Department of Mathematics and Statistics

The effect of boundary slip on transient non-Newtonian blood flows under pulsatile pressure

Nathnarong Khajohnsaksumeth

This thesis is presented for the Degree of
Doctor of Philosophy
of
Curtin University

August 2014

Declaration

To the best of my knowledge and belief, this thesis contains no material previously published by any other person except where due acknowledgment has been made.

This thesis contains no material which has been accepted for the award of any other degree or diploma in any university.

.....
Nathnarong Khajohnsaksumeth
August 2014

Abstract

The effect of fluid-solid boundary slip on fluid flows has been studied in various micro-systems for many years. In this work, we investigate the influence of boundary slip for two pulsatile blood flow problems. In the first problem, we investigate the effect of boundary slip on the transient pulsatile flow of fluids through vessels with body acceleration. The Fahraeus-Lindqvist effect, expressing the fluid behavior near the wall by the Newtonian fluid whereas in the core by a non-Newtonian fluid, is also taken into account. To describe the non-Newtonian behavior, we use the modified second-grade fluid model in which the viscosity and the normal stresses are represented in terms of the shear rate. The complete set of equations are then established and formulated in dimensionless form. For a special case of the material parameters, we derive an analytical solution for the problem; while for the general case, we solve the problem numerically. Our subsequent analytical and numerical results show that the slip parameter has very significant influence on the velocity profile and also the convergence rate of the numerical solutions.

In the second problem, in order to precisely understand the blood flow behavior, the realistic three dimensional geometry domain is taken into account, and we investigate the effect of boundary slip on blood flow in the human right coronary artery (RCA) which provides blood to the heart muscle. The mathematical model is constructed by using the Navier-Stoke equations and the continuity equation under the pulsatile flow condition. The blood is assumed as a non-Newtonian fluid using the Carreau model. The numerical approaches are developed based on the finite element technique utilizing the COMSOL Multiphysics package. Numerical results are presented to show the flow phenomena and the influence of the slip parameter on the flow behaviour.

List of publications during PhD candidature

- N. Khajohnsaksumeth, B. Wiwatanapataphee, and Y.H. Wu. "Flow of a Modified Second-grade Fluid with Boundary Slip Condition.", *Proceedings of International Conference in Mathematics and Applications(ICMA - MU)*, 2011.
- N. Khajohnsaksumeth, B. Wiwatanapataphee, and Y.H. Wu. "The effect of boundary slip on the transient pulsatile flow of a modified second-grade fluid.", *Abstract and Applied Analysis*, ID 858597, 2013.
- N. Khajohnsaksumeth, B. Wiwatanapataphee, and Y.H. Wu. "The effect of slip boundary on the unsteady blood flow in 3D tubes.", *International Conference on Engineering and Applied Science (ICEAS)*, ICEAS-1764, 2013.
- N. Khajohnsaksumeth, B. Wiwatanapataphee, and Y.H. Wu. "The computation of the blood flow model in three-dimensional straight tube domain with boundary slip", *to submit*.

Acknowledgements

I wish to acknowledge the financial support of the Royal Thai Government Scholarship for my PhD study.

I would like to express my thanks to my supervisor, Prof. Yonghong Wu, for his encouragement and supervision throughout the past three years with remarkable patience and enthusiasm.

I would like to thank my co-supervisor, Prof. Benchawan Wiwatanapataphee of Mahidol University, for her continuing encouragement and advice during my PhD study.

I would like to give thanks to all my friends and classmates for their support and friendship particularly, Wilaiporn Paisan, Rinrada Thamchai, Yaowanuch Raksong, Dr.Nattakorn Phewchean, Pawaton Kaemawithanurat, Dr.Qian Sun.

I thank all of the staff in the Department of Mathematics and Statistics at Curtin University for contributing to a friendly working environment. The administrative staff, Joyce Yang, Shuie Liu, Lisa Holling, Jeannie Darmageo, Cheryl Cheng and Carey Ryken Rapp, deserve special thanks for providing kind and professional help on numerous occasions.

Finally, on a more personal note, I sincerely thank everyone in my family, especially my parents, for their love, understanding and support during my entire period of my PhD candidature in Australia.

Contents

CHAPTER 1

Introduction

1.1 Background

Computational techniques have become an effective tool for investigating blood flow behaviour in the cardiovascular system [1], determining hemodynamics quantification of healthy and diseased blood vessels [2–4], designing medical devices and vascular surgeries [5,6], and predicting the intervention outcomes [7–9]. Owing to the rapid development of computational capacity in recent years, many sophisticated mathematical models and numerical algorithms have been developed for simulation of blood flow in arteries. Different types of boundary conditions have also been proposed to accurately determine the interaction between the fluid and the artery wall.

The cardiovascular system is the most important network system in human. This network system of blood vessels delivers appropriate amount of blood, based on physiologic conditions and organ demand, from the heart to all human organs, and vice versa as shown in Figure 1.1. Thus, the arteries providing blood, must react to the changing in the end organs to keep the stability of the overall circulatory system. In order to understand the blood flow behavior in arteries, many research projects [10–14] have been carried out to study blood flow both experimentally and theoretically.

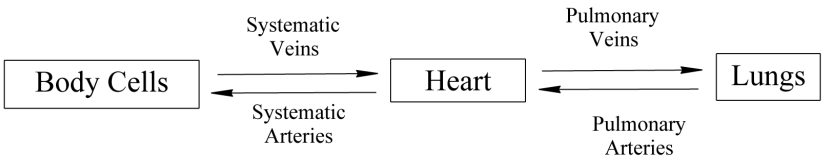

Figure 1.1: diagram showing summarized chart of the cardiovascular system.

1.2 Objectives of the Thesis

The study of blood flows through small vessels by using mathematical models can extract important information to enhance our understanding of the blood flow behavior in arteries and the diseases related to the flow behavior.

The purpose of this work is to study two mathematical models for blood flows driven by a pressure field where the slip boundary is taken into account. The blood flow motion is described by the Navier-Stokes equations and the continuity equation. The main objectives of this research are to obtain analytical solutions and numerical solutions for the models, and examine the influence of the slip boundary on flow behaviour under the pressure driving force.

The specific objectives of this work are as follows:
(1) establish the underlying boundary value problem governing the one-dimensional modified second-grade fluid flow driven by pulsatile pressure fields taking into account the boundary slip,
(2) obtain the analytical solution for the special case of the one-dimensional modified second-grade fluid flow with the slip boundary,
(3) study the blood flow behavior for the one-dimensional modified second-grade fluid model when the slip boundary condition is taken into account,
(4) establish the boundary value problem governing the three-dimensional blood flow driven by pulsatile pressure fields taking into account the boundary slip,
(5) investigate the blood flow behavior in three-dimensional computation domains including the straight tube with constant radius and the tube with variable radius along the tube-length.

1.3 Outline of the Thesis

In this thesis, various analytical and numerical solutions for the blood flow models with boundary slip through blood vessels driven by the pulsatile pressure fields are developed. The thesis is organized into five chapters dividedly as follows:

Chapter 1 gives an overview of the research background and the objectives of the research.

Chapter 2 presents a literature review of the former work and results related to this work including the review of fundamental equations, boundary conditions and prior research works in the field.

Chapter 3 presents the mathematical model and results for the one-dimensional transient flow based on the second-grade fluid model with boundary slip driven by the pulsatile pressure field. Analytical solutions are derived for $m = 0$, while for $m \neq 0$ the problem is solved numerically. Furthermore, the effects of boundary slip are also presented.

Chapter 4 concerns with the three-dimensional transient pulsatile non-Newtonian blood flow model with boundary slip. A complete set of governing equations for the underlying boundary value problem is established followed by the numerical approach based on the finite element method. A series of numerical experiments are then carried out to investigate the influence of boundary slip on the flow behaviour.

Chapter 5 summarizes the main results of this thesis and discusses further research.

CHAPTER 2

Literature Review

2.1 Overview

Over the last couple of decades, a great deal of research has been carried out to study blood flows through vessels, particularly, the effect of stenosis on the motion of blood, the exchange of mechanical stresses, the localization of high shear stresses, and high vorticity zones as they are connected to human cardiovascular disease such as atherosclerosis. In many cases, reduced order structural models can be applied, where the wall effect is assumed to be a thin membrane under particular assumption.

In [15–17], a linear elastic shell model is applied for the vessel wall, where only in the normal direction, the displacement is assumed to be non-zero and the solution is obtained on a cylindrical geometry. Furthermore, in [16–18], the underlying equations for blood flow-wall deformation are solved by an explicit and kinematically coupling algorithm which is used by M.Bukac et al. [19] for the Koiter viscoelastic shell model on a cylindrical geometry with longitudinal displacement. Fernandes [20] analyzed an explicit and kinematically coupled scheme whereas implicit coupling algorithms are applied by many researchers [15, 21, 22] where the equations for the blood flow also include dynamics of the vessel motion.

Many research results have been obtained on the flow behaviour. However, many issues have still not yet been modelled and understood. In this work, we will investigate the influence of boundary slip on the flow behaviour. This work will include construction of mathematical models based on the principles of fluid dynamics, the development of solutions analytically and numerically, and the investigation of boundary slip. Hence in this chapter, we will review topics relevant to the construction of mathematical models, and previous work and results obtained for blood flows in the human cardiovascular system. The cardiovascular

system is introduced in section 2.2. Then the general governing equations for fluid flow are represented in section 2.3, followed by a review of previous research in blood flows.

2.2 The Cardiovascular System

The cardiovascular system of human is a closed network organ system known as the microcirculatory systems [23–27]. The system distributes blood to deliver oxygen, carbon dioxide, hormones, nutrients, etc. to and from cells in the body so that the body can maintain its stabilization, temperature, pH and homeostasis. The three essential components of this system are the heart, the blood, and the blood vessels including the pulmonary circulation system for blood oxygenation and the systemic circulation for blood deoxygenation to body cells.

2.2.1 Human Heart

The most important organ in the human body is the heart since it can cause a severe disease and lead to death ultimately when it works improperly. The human heart locates behind the breastbone which is inside the ribcage between the lungs. It works as a blood pump to drive blood through the blood circulatory system by heart contracting and relaxing. There are four chambers contained in the human heart,namely, left atrium, right atrium, left ventricle, and right ventricle where the two atrium chambers are superior chambers for receiving blood to the human heart while the two ventricle chambers are inferior chambers for releasing blood out of the heart. After the blood transfers the nutrient and oxygen to the body cell being as deoxygenated blood, it flows to the right atrium of the heart via superior vena cava. With the heart contracting and relaxing, the deoxygenated blood in the right atrium is pumped out to the right ventricle of the heart via the tricuspid valve and then transferred to the lung through the pulmonary valve for pulmonary circulation. After the gas exchange processes in the lungs to release carbon dioxide and absorb oxygen, the oxygenated blood flows to the left atrium of the heart through pulmonary veins. With the heart pumping, the oxygenated blood in the left atrium flows to the left ventricle via the Mitral valve. Finally, the oxygenated blood in the left ventricle is pumped via the aortic valve to aorta for releasing the nutrients and oxygen to the body cells through arteries and coronary circulation. Generally, the average size and shape of the adult heart is close to the size and the shape of the close fist as shown in Figure 2.1.

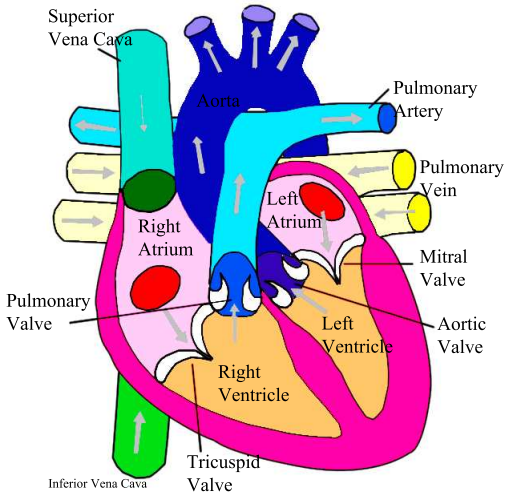

Figure 2.1: sketch showing the front view of the human heart structure.

2.2.2 Blood

Blood is a fluid that contains red blood cells called erythrocytes or RBCs, white blood cells called leukocytes, and platelets called thrombocytes which are floating in a yellow liquid, namely, plasma. With these substances, the blood can transport essential substances such as hormones, oxygen, nutrient etc. to the body cells via the systematic circulation and carry the waste product such as carbon dioxide from the body cells to the pulmonary circulation. Additionally, not only being an exchanging medium, the blood also helps to maintain the body temperature, recovers injury and cures illness. The human body contains blood approximately 7 or 8 percent of the total body weight.

2.2.3 Blood Vessels

Blood vessels are tubes which blood flows to and from the heart for transporting and exchanging substances to the body cells in the circulatory system part. Blood vessels are categorized into three types, namely, arteries, capillaries, and veins.

Arteries are very strength blood vessels that always contain the blood from the heart. There are three types of arteries. The first type is pulmonary artery which receives blood pumped from the right ventricle to the lungs for blood oxygenation. The second type is known as the aorta which is a major artery to deliver the fresh oxygenated blood from the left ventricle to the body cells distribution. Another type is called coronary arteries which receive blood from the aota to the heart-muscle itself since the heart also needs blood for functioning.

Capillaries are small blood vessels which have a single cell thick wall. These

arteries deliver blood for exchanging the essential substance to every body cell through its wall.

The veins are blood vessels that transport blood with low-oxygen level after the substance exchanging from the capillaries to flow back to the heart. To prevent blood from returning to the capillaries, the veins contain valves for unidirectional flow. Moreover, there are tiniest veins known as coronary veins to receive blood with low-oxygen level from the heart muscle and the heart wall outside the human heart and deriver to the right atrium.

2.3 Governing Equations for Fluid Flows

Generally, fluid flows involve the following variables: velocity vector, pressure, stress tensor, deformation rate and fluid density [28–31]. With the assumption of the continuum property, the flow can be described by the fundamental equations of continuum mechanics including the stress equations of motion, the continuity equation, the geometric equations and the constitutive equations. With the previous mentioned equations, we then can derive the so-called Navier-Stokes equations which, together with the continuity equation, form four governing field equations to determine the three velocity components and the fluid pressure in three-dimensional incompressible fluid flows. In this section, we firstly introduce the fundamental equations for continuum mechanics together with the underlying principles and assumptions. Then we review the Navier-Stokes equations with some discussion on their applications and limitations.

2.3.1 The Stress Equations of The Motion Object

Stress vector plays an important role as a fundamental component in continuum mechanics since it is used to measure the internal force intensity created within the object corresponding to the external force. To achieve the stress equation, defining the normal stress and shear stress is needed. First, we define Ω be an arbitrary object where the gravity and the surface force act on as shown in Figure 2.2 and let Γ be a cross-section plane for Ω passing through an arbitrary interior point Q. Then the object Ω is separated into two parts Ω_1 and Ω_2. Without loss of generality, we now consider the force acting on Ω_1. Because of the gravity and the surface force, there is an internal resultant force $\triangle F$ acting on an infinitesimal region $\triangle A$ about point Q. Therefore, the stress vector acting at a point Q on the plane Γ can be defined by the average force acting on the unit area $\triangle A$ when

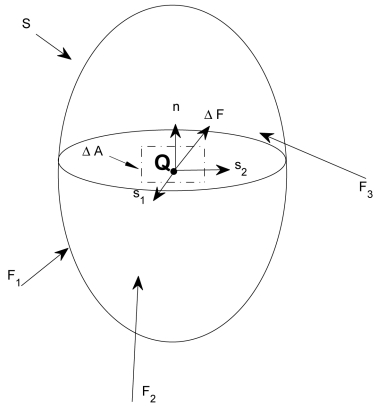

Figure 2.2: sketch showing the internal force $\triangle F$ exerting on the area $\triangle A$ around the point Q for an arbitrary body object

$\triangle A$ goes to zero, namely

$$\sigma = \lim_{\triangle A \to 0} \frac{\triangle F}{\triangle A} \tag{2.1}$$

From Equation (2.1),the stress vector can be interpreted as the strength of the vector acting on the interior point of the object body.

Since the force $\triangle F$ is an arbitrary force and needs not to be normal to the surface $\triangle A$, without loss of generality, the force $\triangle F$ can be decomposed into three orthogonal components $\triangle F_n$, $\triangle F_{s1}$, and $\triangle F_{s2}$ where $\triangle F_n$ denotes the vector projection of $\triangle F$ on the unit normal vector of the surface area $\triangle A$ at point Q, and $\triangle F_{s1}$ and $\triangle F_{s2}$ denote vector projections of $\triangle F$ on the unit span vectors S_1, S_2 of the tangent plane of the surface area $\triangle A$ at point Q, respectively, such that S_1 is perpendicular to S_2.
Then Equation (2.1) can be expressed as

$$\sigma = \lim_{\triangle A \to 0} \left(\frac{\triangle F_n}{\triangle A}, \frac{\triangle F_{s1}}{\triangle A}, \frac{\triangle F_{s2}}{\triangle A} \right) \tag{2.2}$$

According to Equation (2.2), the so-called normal stress which is the stress vector in the normal direction to the surface area $\triangle A$ at point Q can be defined as

$$\sigma_n = \lim_{\triangle A \to 0} \frac{\triangle F_n}{\triangle A}, \tag{2.3}$$

while the components

$$\sigma_{s1} = \lim_{\triangle A \to 0} \frac{\triangle F_{s1}}{\triangle A} \tag{2.4}$$

and

$$\sigma_{s2} = \lim_{\triangle A \to 0} \frac{\triangle F_{s2}}{\triangle A} \tag{2.5}$$

are the stress vectors on the tangent plane of the surface area $\triangle A$ at point Q called shear stresses.

Thus, any stress vector of the force acting on an arbitrary point in an object can be written in term of one normal stress and two shear stresses. Following their definition, it has been seen that the normal stress can cause either tension or compression in the object, whereas the shape change in the object occurs due to the shear stresses.

To be able to specify the stress component σ conveniently, double subscript notation is required. We denote the first subscript notation as a normal direction to the plane on which the stress exerts, and the second subscript notation as a direction of the stress vector. That is, σ_{ij} represents the stress in j-direction acting on a plane normal to the i-axis. Additionally, the sign of the stress component is determined being positive if and only if the stress exerts toward the positive coordinate direction on a positive plane or the stress exerts toward the negative coordinate direction on a negative plane. Otherwise, the sign of the stress component is considered as negative.

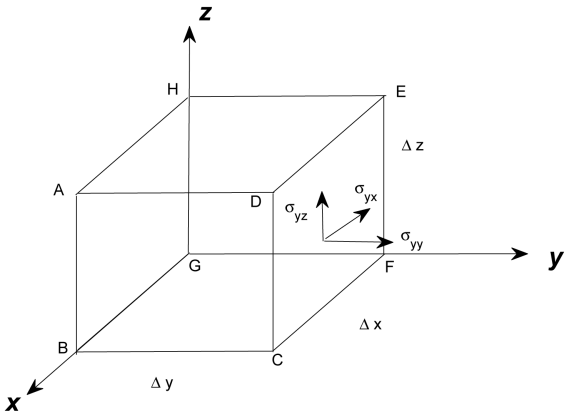

Figure 2.3: sketch showing two shear stresses and one normal stress on the CDEF-face of the rectangular element

Following Newton's second law, we can derive a set of equations fulfilled by the stress components, namely stress equations of the motion. Without loss of generality, let Ω_1 be the free body diagram of a differential element in three-dimension coordinate system (x, y, z) with mass density ρ as shown in Figure 2.5 and

$$\sigma_{CDEF}(x, y, z) = (\sigma_{yx}(x, y, z), \sigma_{yy}(x, y, z), \sigma_{yz}(x, y, z)) \tag{2.6}$$

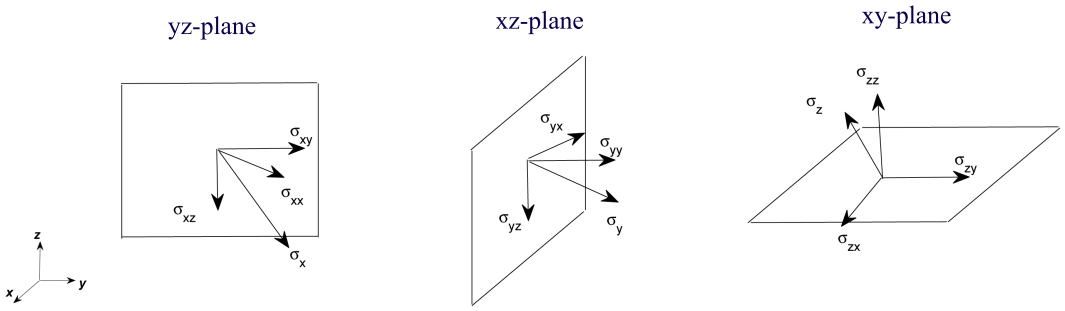

Figure 2.4: sketch showing the decomposition of the stress into two shear stress and one normal stress on the yz-plane, xz-plane, and xy-plane.

be a known stress vector acting on the $ABGH$-face. According to the assumption of stress continuity , the stress vector on $CDEF$-face is

$$\sigma_{CDEF}(x, y+\triangle y, z) = (\sigma_{yx}(x, y+\triangle y, z), \sigma_{yy}(x, y+\triangle y, z), \sigma_{yz}(x, y+\triangle y, z)) \quad (2.7)$$

We then apply the Taylor series expansion which yields

$$\begin{aligned}
\sigma_{yx}(x, y+\triangle y, z) &= \sigma_{yx}(x, y, z) + \frac{\partial \sigma_{yx}}{\partial y} dy + \mathcal{O}(dy)^2, && (2.8)\\
\sigma_{yy}(x, y+\triangle y, z) &= \sigma_{yy}(x, y, z) + \frac{\partial \sigma_{yy}}{\partial y} dy + \mathcal{O}(dy)^2, && (2.9)\\
\sigma_{yz}(x, y+\triangle y, z) &= \sigma_{yz}(x, y, z) + \frac{\partial \sigma_{yz}}{\partial y} dy + \mathcal{O}(dy)^2. && (2.10)
\end{aligned}$$

Analogously, the stress vector on the $ABCD$-face can be obtained as

$$\begin{aligned}
\sigma_{xx}(x+\triangle x, y, z) &= \sigma_{xx}(x, y, z) + \frac{\partial \sigma_{xx}}{\partial x} dx + \mathcal{O}(dx)^2, && (2.11)\\
\sigma_{xy}(x+\triangle x, y, z) &= \sigma_{xy}(x, y, z) + \frac{\partial \sigma_{xy}}{\partial x} dx + \mathcal{O}(dx)^2, && (2.12)\\
\sigma_{xz}(x+\triangle x, y, z) &= \sigma_{xz}(x, y, z) + \frac{\partial \sigma_{xz}}{\partial x} dx + \mathcal{O}(dx)^2, && (2.13)
\end{aligned}$$

and the stress vector on the $ADEH$-face can be obtained as

$$\begin{aligned}
\sigma_{zx}(x, y, z+\triangle z) &= \sigma_{zx}(x, y, z) + \frac{\partial \sigma_{zx}}{\partial z} dz + \mathcal{O}(dz)^2, && (2.14)\\
\sigma_{zy}(x, y, z+\triangle z) &= \sigma_{zy}(x, y, z) + \frac{\partial \sigma_{zy}}{\partial z} dz + \mathcal{O}(dz)^2, && (2.15)\\
\sigma_{zz}(x, y, z+\triangle z) &= \sigma_{zz}(x, y, z) + \frac{\partial \sigma_{zz}}{\partial z} dz + \mathcal{O}(dz)^2. && (2.16)
\end{aligned}$$

By the definition of stress vector, the forces exerting on the surface in the x-

direction can be found as follows:

$$\mathbf{F}_1 = -\sigma_{xx} dydz \tag{2.17}$$

$$\mathbf{F}_2 = \left(\sigma_{xx} + \frac{\partial \sigma_{xx}}{\partial x} dx\right) dydz \tag{2.18}$$

$$\mathbf{F}_3 = -\sigma_{yx} dydz \tag{2.19}$$

$$\mathbf{F}_4 = \left(\sigma_{yx} + \frac{\partial \sigma_{yx}}{\partial y} dy\right) dxdz \tag{2.20}$$

$$\mathbf{F}_5 = -\sigma_{zx} dydz \tag{2.21}$$

$$\mathbf{F}_6 = \left(\sigma_{zx} + \frac{\partial \sigma_{zx}}{\partial z} dz\right) dxdy \tag{2.22}$$

$$\tag{2.23}$$

Therefore, the total surface force in the x-direction can be calculated as

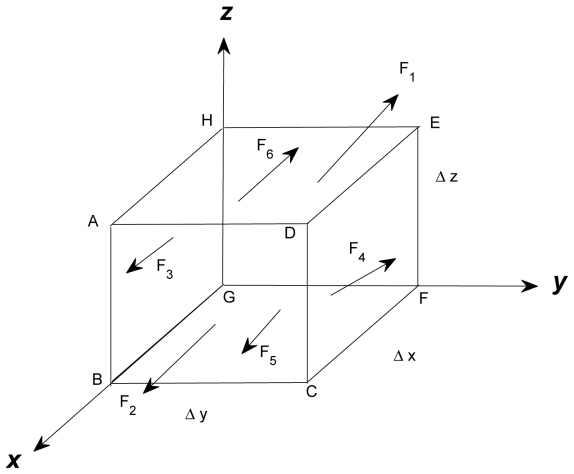

Figure 2.5: sketch showing all forces in the x-direction acting on an arbitrary element.

$$\begin{aligned}
\mathbf{F}_{x,surface} &= \mathbf{F}_1 + \mathbf{F}_2 + \mathbf{F}_3 + \mathbf{F}_4 + \mathbf{F}_5 + \mathbf{F}_6 \\
&= -\sigma_{xx} dydz + \left(\sigma_{xx} + \frac{\partial \sigma_{xx}}{\partial x} dx\right) dydz - \sigma_{yx} dydz \\
&\quad + \left(\sigma_{yx} + \frac{\partial \sigma_{yx}}{\partial y} dy\right) dxdz - \sigma_{zx} dydz + \left(\sigma_{zx} + \frac{\partial \sigma_{zx}}{\partial z} dz\right) dxdy \\
&= \left(\frac{\partial \sigma_{xx}}{\partial x} + \frac{\partial \sigma_{yx}}{\partial y} + \frac{\partial \sigma_{zx}}{\partial z}\right) dxdydz
\end{aligned} \tag{2.24}$$

Furthermore, by the definition of the body force which applies on the volumetric mass straightly, we then suppose that the body force (force per unit mass) as (X, Y, Z) with an acceleration (a_x, a_y, a_z), hence the body force in the x-direction

can be computed by

$$\mathbf{F}_{x,body} = \rho X dxdydz. \tag{2.25}$$

Applying Newton's second law, i.e. $\Sigma\mathbf{F} = ma$, the total net force in the x-direction can be represented by

$$\mathbf{F}_{x,surface} + \mathbf{F}_{x,body} = ma_x \tag{2.26}$$

that is,

$$\left(\frac{\partial\sigma_{xx}}{\partial x} + \frac{\partial\sigma_{yx}}{\partial y} + \frac{\partial\sigma_{zx}}{\partial z}\right) dxdydz + \rho X dxdydz = \rho dxdydz a_x \tag{2.27}$$

which yields

$$\left(\frac{\partial\sigma_{xx}}{\partial x} + \frac{\partial\sigma_{yx}}{\partial y} + \frac{\partial\sigma_{zx}}{\partial z}\right) + \rho X = \rho a_x \tag{2.28}$$

Analogously, the total net force in the y-direction can be derived as

$$\left(\frac{\partial\sigma_{xy}}{\partial x} + \frac{\partial\sigma_{yy}}{\partial y} + \frac{\partial\sigma_{zy}}{\partial z}\right) + \rho Y = \rho a_y \tag{2.29}$$

and the total net force in the z-direction can be presented as

$$\left(\frac{\partial\sigma_{xz}}{\partial x} + \frac{\partial\sigma_{yz}}{\partial y} + \frac{\partial\sigma_{zz}}{\partial z}\right) + \rho Z = \rho a_z \tag{2.30}$$

Furthermore, we assume that there is no rotation in our model. Consequently, the force moment is set to be zero, namely $\Sigma M = 0$, and we have

$$\sigma_{ij} = \sigma_{ji} \tag{2.31}$$

where i, j-indices denote as subscript notation of x, y, and z. Besides, it has been shown that the stress tensor is a second order symmetric tensor.

2.3.2 Equation of Continuity

To obtain the model for the finite control volume V fixed in space, let ρ be the fluid density and v be the flow velocity vector at a point on the closed surface S where n is an outward unit normal vector of the closed elemental surface S. We also suppose that V is an elemental volume. Applying the fundamental physical principle of mass conservation, namely the mass cannot be created or destroyed if there is no nuclear reaction, the net mass flow out of the control volume through

surface S must be equal to the rate of decrease in the mass inside the control volume with respect to time.

Since the mass flow of a moving fluid through any fixed surface is calculated by the product of the density and the area of surface and the vector projection of the velocity vector on the normal vector of the control surface, for a small control surface dS, it can be expressed as

$$\rho v_n dS = \rho v \cdot n dS. \tag{2.32}$$

We observe that if the direction of the velocity v points in the direction out of the control volume, i.e. the mass flow is leaving the control volume or it is an outflow, the product in equation (2.32) is positive. Reversely, if the direction of the velocity v points into the control volume, i.e. the mass flow is entering the control volume or it is an inflow, the product in equation (2.32) is negative.

Therefore, the net mass flow out of control volume through surface S is represented by

$$\iint_S \rho v \cdot n dS. \tag{2.33}$$

On the other hand, the total mass held within the control volume V can be computed by

$$\iiint_V \rho dV, \tag{2.34}$$

it yields that the rate of increase in the mass inside V is

$$\frac{\partial}{\partial t} \iiint_V \rho dV. \tag{2.35}$$

Thus, the rate of decrease in the mass inside V is

$$-\frac{\partial}{\partial t} \iiint_V \rho dV. \tag{2.36}$$

Therefore, the equation of the mass conservation can be demonstrated as

$$\iint_S \rho v \cdot n dS = -\frac{\partial}{\partial t} \iiint_V \rho dV. \tag{2.37}$$

Applying the divergence theorem on the surface integral term of the equation (2.37) and then rearranging it, we have

$$\iiint_V \left[\frac{\partial \rho}{\partial t} + \nabla \cdot (\rho v) \right] dV = 0, \tag{2.38}$$

where $\nabla = (\frac{\partial}{\partial x}, \frac{\partial}{\partial y}, \frac{\partial}{\partial z})$

Since the control volume V is arbitrary, the integral in equation (2.39) is zero if and only if the integrand is equal to zero at any point within the control volume V, thus

$$\frac{\partial \rho}{\partial t} + \nabla \cdot (\rho v) = 0, \tag{2.39}$$

where is the so-called continuity equation.

For the incompressible fluid flow, the fluid density ρ is a constant and equation (2.39) reduces to

$$\nabla \cdot v = 0. \tag{2.40}$$

2.3.3 Equations of Deformation

To obtain the rate of the fluid deformation, the geometric equations described by the velocity vector is considered. For the three-dimensional space, the deformation rate is a tensor given by

$$d = \begin{bmatrix} d_{xx} & d_{xy} & d_{xz} \\ d_{yx} & d_{yy} & d_{yz} \\ d_{zx} & d_{zy} & d_{zz} \end{bmatrix}, \tag{2.41}$$

where d_{xx}, d_{yy}, and d_{zz} are the normal deformation rate corresponding to x, y, and z directions for measuring the rate of size changing in x, y, and z directions respectively, and other components of d are the shear deformation rate for measuring the rate of shape change on different coordinate planes.

Because of the continuity of the velocity field in the fluid flow, the deformation rate tensor can be defined corresponding to the velocity vector as

$$d = \frac{1}{2}\left(\nabla v + \nabla v^T\right) \tag{2.42}$$

where v^T is the transpose of the velocity vector.

With the index notation, equation (2.43) can be rewritten as

$$d = \frac{1}{2}\left(\frac{\partial v_i}{\partial x_j} + \frac{\partial v_j}{\partial x_i}\right) \tag{2.43}$$

where $i, j = 1, 2$, and 3.

2.3.4 Constitutive Equations

There are many constitutive equations proposed for different problems. Generally, the constitutive equations are the relationships between the deformation rate and the stress in fluids. Based on the constitutive equations, fluid models are classified as Newtonian fluid models where the shear stress is a linear function of the deformation rate, and non-Newtonian fluid models.

In this thesis, we consider an one-dimensional non-Newtonian fluid flow models using the constitutive equations of a modified (generalised)-second grade fluid in Chapter 3, and the three-dimensional non-Newtonian fluid flow model using the constitutive equations of Carreau's shear-thinning model in chapter 4. The constitutive equations can be written in the general form of

$$\sigma = -p\mathbf{I} + h(\mathbf{D}) \tag{2.44}$$

where p is the blood pressure, $\mathbf{I}$ is a 3x3 identity matrix, and $h(\mathbf{D})$ is the 3x3 matrix function of the rate of deformation tensor $\mathbf{D}$.

By using index notation, equation (2.44) can be written as

$$\sigma_{ij} = -p\delta_{ij} + h_{ij}(\mathbf{D}), \tag{2.45}$$

where δ_{ij} is the delta function, and $i, j = 1, 2, 3$ for three-dimensional problems.

2.3.5 Navier-Stokes Equations

By the continuum assumption, at any point in the fluid flow domain, all field equations must be satisfied. Consequently, we substitute the constitutive equations (2.44) into the equation of motion (2.28) - (2.30). With the index notation, the equations of motion become

$$\rho a_i = \rho X_i - \frac{\partial p}{\partial x_i} + \frac{\partial h_i(\mathbf{D})}{\partial x_i}, \tag{2.46}$$

where h_i is the i-th row rate function of the deformation tensor $\mathbf{D}$ for $i = 1, 2, 3$.

Furthermore, $a = (a_1, a_2, a_3)$ is the changing rate of the velocity vector with respect to time, we then have

$$a_i = \frac{Dv_i}{Dt}, \tag{2.47}$$

where $v(x_1, x_2, x_3, t) = (v_1(x_1, x_2, x_3, t), v_2(x_1, x_2, x_3, t), v_3(x_1, x_2, x_3, t))$ and $\frac{D\cdot}{Dt}$ is the derivative with respect to time. According to the definition of the particle

location (x_1, x_2, x_3) in the fluid flow, we also have $x_i = x_i(t)$ and $v_i = \frac{dx_i(t)}{dt}$ for $i = 1, 2, 3$. Then equation (2.47) can be written as

$$\begin{aligned}
a_i &= \frac{Dv_i}{Dt} \\
&= \frac{\partial v_i(x_1(t), x_2(t), x_3(t), t)}{\partial t} \\
&= \frac{\partial v_i(x_1(t), x_2(t), x_3(t), t)}{\partial t}\frac{\partial t}{\partial t} + \frac{\partial v_i(x_1(t), x_2(t), x_3(t), t)}{\partial x_1}\frac{\partial x_1(t)}{\partial t} + \\
&\quad \frac{\partial v_i(x_1(t), x_2(t), x_3(t), t)}{\partial x_2}\frac{\partial x_2(t)}{\partial t} + \frac{\partial v_i(x_1(t), x_2(t), x_3(t), t)}{\partial x_3}\frac{\partial x_3(t)}{\partial t} + \\
&= \frac{\partial v_i(x_1(t), x_2(t), x_3(t), t)}{\partial t} + v_1(x_1(t), x_2(t), x_3(t), t)\frac{\partial v_i(x_1(t), x_2(t), x_3(t), t)}{\partial x_1} + \\
&\quad v_2(x_1(t), x_2(t), x_3(t), t)\frac{\partial v_i(x_1(t), x_2(t), x_3(t), t)}{\partial x_2} + \\
&\quad v_3(x_1(t), x_2(t), x_3(t), t)\frac{\partial v_i(x_1(t), x_2(t), x_3(t), t)}{\partial x_3} \\
&= \frac{\partial v_i}{\partial t} + v_1\frac{\partial v_i}{\partial x_1} + v_2\frac{\partial v_i}{\partial x_2} + v_3\frac{\partial v_i}{\partial x_3}. \qquad (2.48)
\end{aligned}$$

Substituting a_i back into equation (2.46) yields

$$\rho(\frac{\partial v_i}{\partial t} + v_1\frac{\partial v_i}{\partial x_1} + v_2\frac{\partial v_i}{\partial x_2} + v_3\frac{\partial v_i}{\partial x_3}) = \rho X_i - \frac{\partial p}{\partial x_i} + \frac{\partial h_i(\mathbf{D})}{\partial x_i} \qquad (2.49)$$

which is known as the Navier-Stokes equations. This system of equations can be fully written as follows

$$\begin{aligned}
\rho(\frac{\partial v_1}{\partial t} + v_1\frac{\partial v_1}{\partial x_1} + v_2\frac{\partial v_1}{\partial x_2} + v_3\frac{\partial v_1}{\partial x_3}) &= \rho X_1 - \frac{\partial p}{\partial x_1} + \frac{\partial h_1(\mathbf{D})}{\partial x_1}, \qquad (2.50) \\
\rho(\frac{\partial v_2}{\partial t} + v_1\frac{\partial v_2}{\partial x_1} + v_2\frac{\partial v_2}{\partial x_2} + v_3\frac{\partial v_2}{\partial x_3}) &= \rho X_2 - \frac{\partial p}{\partial x_2} + \frac{\partial h_2(\mathbf{D})}{\partial x_2}, \qquad (2.51) \\
\rho(\frac{\partial v_3}{\partial t} + v_1\frac{\partial v_3}{\partial x_1} + v_2\frac{\partial v_3}{\partial x_2} + v_3\frac{\partial v_3}{\partial x_3}) &= \rho X_3 - \frac{\partial p}{\partial x_3} + \frac{\partial h_3(\mathbf{D})}{\partial x_3}. \qquad (2.52)
\end{aligned}$$

Obviously, giving the constitutive equations, the Navier-Stokes equations (2.49) with the continuity equation (2.40) construct a system of four differential equations for four unknown variables p, and v_i for $i = 1, 2, 3$ and thus are solvable in principle. However, to be differentiable one flow situation from another, the boundary behavior fulfilled by the pressure field p and the velocity field v must be defined.

Note that the Navier-Stokes equations in the cylindrical coordinate system

can be expressed as

$$\rho\left(\frac{\partial v_r}{\partial t}+v_r\frac{\partial v_r}{\partial r}+\frac{v_\phi}{r}\frac{\partial v_r}{\partial \phi}+v_z\frac{\partial v_r}{\partial z}-\frac{v_\phi^2}{r}\right) = -\frac{\partial p}{\partial r}+\rho X_r+\frac{\partial h_1(\mathbf{D})}{\partial r} \tag{2.53}$$

$$\rho\left(\frac{\partial v_\phi}{\partial t}+v_r\frac{\partial v_\phi}{\partial r}+\frac{v_\phi}{r}\frac{\partial v_\phi}{\partial \phi}+v_z\frac{\partial v_\phi}{\partial z}-\frac{v_\phi v_r}{r}\right) = -\frac{1}{r}\frac{\partial p}{\partial \phi}+\rho X_\phi+\frac{\partial h_2(\mathbf{D})}{\partial \phi} \tag{2.54}$$

$$\rho\left(\frac{\partial v_z}{\partial t}+v_r\frac{\partial v_z}{\partial r}+\frac{v_\phi}{r}\frac{\partial v_z}{\partial \phi}+v_z\frac{\partial v_z}{\partial z}\right) = -\frac{\partial p}{\partial r}+\rho X_z+\frac{\partial h_3(\mathbf{D})}{\partial z} \tag{2.55}$$

2.3.6 No-Slip and Slip Boundary Conditions

The system of four partial differential equations including the Navier-Stokes equations and continuity equation contains four unknown variables, i.e. three component of the velocity vector and the pressure field. In order to achieve the solution for the velocity vector and the pressure field, boundary conditions corresponding to the problem must be addressed. In this section, we will discuss no-slip and slip condition associated with the fluid-solid interfaces.

In our work, we suppose that the boundary $\partial\Omega$ is an impermeable wall. That is

$$\mathbf{v}\cdot\mathbf{n}=0 \qquad \text{on} \quad \partial\Omega, \tag{2.56}$$

where $\mathbf{v}$ is a velocity vector, $\mathbf{n}$ is an outward outer unit normal vector at the boundary.

According to Navier's slip boundary condition [32] , one has

$$\lambda_t\left[\mathbf{v}-(\mathbf{v}\cdot\mathbf{n})\mathbf{n}\right]+(1-\lambda_t)\left[\mathbf{T}\cdot\mathbf{n}-(\mathbf{n}\cdot\mathbf{T}\cdot\mathbf{n})\mathbf{n}\right]=0 \qquad \text{on} \qquad \partial\Omega \tag{2.57}$$

where λ_t is a parameter, $\mathbf{n}$ is a outward unit normal vector at the boundary, $\mathbf{T}$ is the stress tensor and $\mathbf{v}$ is a velocity vector.

Clearly, if $\lambda_t = 1$, equation (2.57) becomes the so-called no slip boundary condition suggested in 1845 by Sir George Gabriel Stokes.

The no-slip boundary condition assumes that the layer of fluid molecules adjoining the solid boundary accepts the same velocity as the solid boundary. Thus the layer of fluid molecules near the fixed wall would have zero tangential velocity [33] as shown in Figure 2.6. Nevertheless, the no-slip boundary condition is a hypothesis rather than a condition deduced from any principle. Many researchers [34–39] reported the existence of slip of a fluid on solid surface. Thus, it is

important to develop a unified slip boundary condition taking into account the blood flow in artery by specifying a appropriate velocity slip boundary condition on the wall.

Yang [40] studied slip effects on the micropipe liquid flow in theoretical analysis, and constructed the criterion for flow velocity slip layer near wall with the velocity slip computation.

The cohesion and adhesion between the molecules create the liquid viscosity essentially. With the liquid viscosity, the liquid is adhesive on the solid boundary. Since there is a liquid intermolecular force and the fluid molecules moves highly in random direction, the force between the liquid and solid cannot be measured by calculating molecules force between liquid and solid surface.

The technique to compute the exerting force between the solid and liquid molecular groups depending on the three Hamaker material hypotheses was established by Zhang [41]. They found that not only the liquid flow and heat transfer of the liquid are affected by the boundary slip greatly but also the channel wall characters and shear stress. Zhang and his co-workers supposed that the liquid molecules have uniform distribution inside the pipe and the impact of random movement of fluid molecules is ignored. A numerical integration method was introduced to compute the force between fluid molecules and solid wall. When the wall has a large enough force to prevent the shear stress from the fluid flow, the micelles near the wall are able to preserve stationary state, hence the velocity slip will be impacted by the fluid and the solid molecular potential parameters as well as the flow shear stress. Velocity slip on the wall micelles experience from the wall frictional force. When the fraction increases, the micelles velocity in flow increases. Thus, the friction coefficient is applied to compute the fraction of the wall and after that the velocity of the liquid group is considered. From the experiment in a micron pipe, it informes that a small velocity slip may appear when the flow pressure gradient is relatively large, and will lead to the errors of calculation in the pipe flow.

Liquid slip boundary implies that the velocity of the liquid molecules at the wall is not equal to zero, while no-slip presents physically in a situation where the liquid in the first molecular layer is statics and all the other molecules are shear past the first molecular layer. The liquid molecules flow through the first molecular layer is subject to strong friction on the wall. The lower the friction with the wall is, the less forces is needed for a given flow velocity. Therefore, slip is very important in microfluidics since it significantly reduces the required pressure in pressure-driven flows. In most experiments dealing with slip, the slip

length can be achieved from measurement [39].

A slip length parameter or a slip coefficient l_s on a rigid surface can be achieved by simplifying equation (2.57) as follows

$$\mathbf{v} = l_s \mathbf{n} \cdot [(\nabla \mathbf{v}) + (\nabla \mathbf{v})^T], \tag{2.58}$$

where l_s is assumed to be a material parameter.

The slip length is the local equivalent distance under the solid surface as shown in Figure 2.7. In this case, the no-slip boundary condition is fulfilled as the flow field is linearly extended outside of the physical domain. In Figure 2.8, it demonstrates a stage where the liquid does not obtain any friction with the wall. Over the last couple of years, various researches have been investigated to understand various flow behaviour of Newtonian and non-Newtonian fluid flow with slip boundary condition.

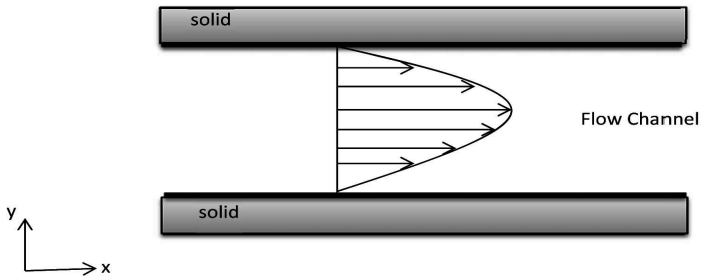

Figure 2.6: sketch showing the channel flow behaviour with no-slip boundary condition.

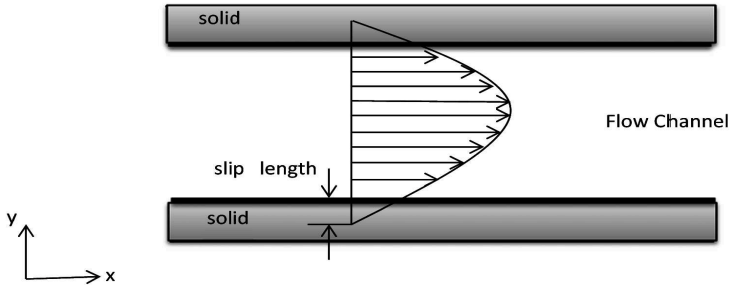

Figure 2.7: sketch showing the channel flow behaviour for slip boundary with finite slip length.

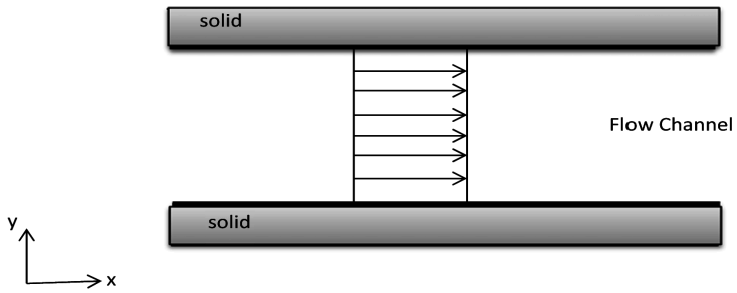

Figure 2.8: sketch showing the channel flow behaviour for slip boundary with infinity slip length.

2.4 Previous Works on Blood Flow in Arteries

In this section, previous research on blood flow in arteries is reviewed. Based on the dimension of the problems, the models of blood flows are reviewed in three categories corresponding respectively to one-dimensional models (section 2.4.1), two-dimensional models (section 2.4.2), and three-dimensional models (section 2.4.3).

2.4.1 One-Dimensional Blood Flow Models

To study the blood flow behavior and propagation of pressure-wave in the system of human arteries, a one-dimensional pulsating blood flow model was introduced by A. Quarteroni et al. [42–44]. Because of the complexity of the three-dimensional fluid-structure models, the one-dimensional models can be taken as another way or combined with them in a geometrical multiscale approach [45]. These models are derived by averaging the Navier-Stoke equations on each section of an arterial vessel and using simplified model for vessel compliance which provides lower orders of magnitude compared to higher-dimensional models based on the coupling of the Navier-Stokes equations for the flow field in the arterial lumen and a mechanical model for the vessel-wall displacement. Although The results of the one-dimensional models are just an averaged information, a good demonstration of the pressure-wave propagation in arteries is presented [46, 47].

To derive the governing equations, the system of partial differential equations is established by considering a vessel of length l with a centreline $s(x)$ with a cross-sectional area $A(s,t)$ normal to s. Moreover, $Q(x,t) = Au$ is defined as the volume flux at a given section where $u(s,t)$ is an average velocity. With the mass conservation in control volume such that the rate of mass change within the control volume is equal to the negative value of the net mass flux out of the

control volume. Let $V(t) = \int_0^l A dx$ be the volume. Furthermore,it is supposed that the seepage through the side wall is equal to zero then the mass conservation can be presented as

$$\rho \frac{dV(t)}{dt} + \rho Q(l,t) - \rho Q(0,t) = 0, \tag{2.59}$$

where ρ is a mass density. By substituting $V(t) = \int_0^l A(x,t)dx$ and $Q(l,t) - Q(0,t) = \int_0^l \frac{\partial Q}{\partial x} dx$ into equation (2.59), it yields

$$\rho \frac{d}{dt} \int_0^l A(x,t)dx + \rho \int_0^l \frac{\partial Q}{\partial x} dx = 0. \tag{2.60}$$

Suppose l is independent of time, the time derivative can be taken inside the integral then equation(2.60) becomes

$$\rho \int_0^l \left\{ \frac{\partial A}{\partial t} + \frac{\partial Q}{\partial x} \right\} dx = 0. \tag{2.61}$$

Since l is arbitrary and equation (2.61) must be fulfilled for any value of l, the differential one-dimensional mass conservation equation can be achieved as

$$\frac{\partial A}{\partial t} + \frac{\partial Q}{\partial x} = \frac{\partial A}{\partial t} + \frac{\partial uA}{\partial x} = 0. \tag{2.62}$$

Then the momentum equation for one-dimensional flow was considered with the assumption that the flux through the side wall in the x-direction is equal to zero. Since the momentum equation implies that the rate of momentum change in the control volume with the net flux of momentum of out of the control volume is equal to the total force acting on the control volume. Thus, the momentum equation for one-dimensional flows follows

$$\frac{d}{dt} \int_0^l \rho Q dx + (\alpha \rho Q u)_l - (\alpha \rho Q u)_0 = F, \tag{2.63}$$

where F is a total force exerting on the control volume in the x-direction and $\alpha(x,t)$ is a momentum flux correction factor which accounts for the nonlinearity of the sectional integration.

To achieve the complete momentum equation, the total force F dealing with a pressure and viscous force is defined, that is

$$F = (pA)_0 - (pA)_l + \int_0^l p \frac{\partial A}{\partial x} dx + \int_0^l f dx, \tag{2.64}$$

where p is pressure and f is the friction force per unit length.
By substituting F into equation(2.64), it yields that

$$\frac{d}{dt}\int_0^l \rho Q dx + (\alpha\rho Qu)_l - (\alpha\rho Qu)_0 = (pA)_0 - (pA)_l + \int_0^l p\frac{\partial A}{\partial x}dx + \int_0^l f dx. \quad (2.65)$$

Since $(\alpha\rho Qu)_l - (\alpha\rho Qu)_0 = \int_0^l \frac{\partial(\alpha\rho Qu)}{\partial x}dx$, $(pA)_0 - (pA)_l = -\int_0^l \frac{\partial(pA)}{\partial x}dx$, and suppose that l is independent of time and ρ is constant, it results

$$\rho\int_0^l \left\{\frac{\partial Q}{\partial t} + \frac{\partial(\alpha Qu)}{\partial x}\right\}dx = \int_0^l \left\{-\frac{\partial(pA)}{\partial x} + p\frac{\partial A}{\partial x} + f\right\}dx. \quad (2.66)$$

Since it must be satisfied for any value of l, one has

$$\frac{\partial Q}{\partial t} + \frac{\partial(\alpha Qu)}{\partial x} = -\frac{A}{\rho}\frac{\partial p}{\partial x} + \frac{f}{\rho}. \quad (2.67)$$

To analyse the one-dimensional arterial system in an alternative approach, Wang & Parker [48,49] applied a semi-analytical time-space domain technique to establish the linearised wave motion in arteries. The authors proposed a highly idealised cardiac function in a fairly realistic model of the anatomy of the largest arteries and construct their model on the data of Westerhof & Noordergraaf [50]. Then Skalak [51], Stettler et al. [52, 53] and Stergiopulos et al. [54] studied the wave behaviour by applying the method of characteristic.

The one-dimensional flow model provides a good investigation of the propagation of pressure waves in arteries [55,56], it can be successfully applied to study the effect on pulse waves of geometrical and mechanical arterial modification for the presence of stenoses or the placement of stents or prostheses [57,58]. Since the model needs a low cost of computation, it is usable to investigate pressure wave propagation on an isolated arterial segment [59–62] and the global circulation system [61, 63–65]. Nevertheless, they cannot obtain flow-field details sufficient to accept a reliable calculation of local quantities such as wall shear stresses. To be able achieve these details, a three-dimensional model is needed. However, the one-dimensional explanation may still require in the case when the frame of multi-scale approach is applied.

2.4.2 Two-Dimensional Blood Flow Models

Blood flow models in two-dimensional space have been investigated for a couple of decades [66]. B.Chahboune and J.M. Crolet [66] introduced a two-dimensional

mathematical model and a numerical simulation based on the finite element method to compute the fluid-structure interaction during the cardiac cycle. The model is applied to couple the blood flow with the motion of the arterial wall of the left ventricle. A time-evolution is imposed for the shape of the cardiac wall. Sunčica Čanić et al. [67] proposed a closed system of effective equations presenting a time-dependent flow of a viscous incompressible Newtonian fluid in a long and narrow elastic tube. They applied the three-dimensional incompressible Navier-Stokes equations with the axially symmetric assumption. The tube wall is modelled by two ways: the linear membrane shell model, and the linearly elastic Koiter shell model. The behaviour of the coupled fluid-structure interaction problem reaches the limit when the ration between the radius and the length of the tube tends to zero is investigated. The reduced equations that are of Biot type with memory is achieved. Moreover, the reduced equations also lead to the memory term explicitly capturing the viscoelastic nature of the coupled problem. The reduced model is validated experimentally by using a mock circulatiory flow loop assembled at the Cardiovascular Research Laboratory at the Texas Heart Institute. The results of the experiment agreed excellently to the numerical solution.

2.4.3 Three-Dimensional Blood Flow Models

Recently, due to the rapid development of sophisticated computational techniques to support the computation for complex problems, more complex blood flow models have been investigated widely by many researchers [68–76]. Queen(1992) formulated a three-dimensional model to study the heart behaviour where the four chambers, the four valves system and the exiting vessels are included. Gerbeau et al. [68] proposed a three-dimensional model for the fluid-structure interaction in the arteries. They also introduced a numerical algorithm for simulating the fluid-structure interaction in large complian vessels where large displacement is issued. Their strategy aims to get realistic simulations on a gemoetries coming from medical imaging. However, the interpretation of results in biological sense is ignored. However, many researchers have proposed and introduced many computational approaches to investigate the blood flow behaviour by examining only the field of velocity, treating the vessel wall of subject-specific problem as rigid [72–76], or considering simplified or reduced geometries of deformable wall problems [70, 71]. The ALE(Arbitraily Lagrangian-Eulerian) technique for fluid-structure interaction problem is one of the well-known method for approaching the blood flow problem including wall deformation [77,78]. It has been greatly im-

proved to solve blood flow problem in deformable domains in recent years [79–81]. Howerver, the ALE method still encounters a formidable problem for large, realistic anatomic and physiologic models of the cardiovascular system. C.Alberto Figueroa et al. [69] introduced the so-called coupled momentum method for fluid-solid interaction problems(CMM-FSI), and three-dimensional deformable models of arteries. This technique couples the equations of the vessel wall deformation at the variational level as a boundary condition for the fluid domain. A strong coupling of the degree-of-freedom of the fluid and the solid domains, a linear membrane model which supported with transverse shear for the wall of the vessel are determined. The effect of the vessel wall boundary is considered in a monolithic way to the fluid model. Furthermore, the other techniques to compute the blood flow models including the wall deformability are based on the immersed boundary method [82, 83] or on transpiration approaches based on linearization principles [84, 85].

2.5 Concluding Remarks

The problem of blood flow in arteries has been investigated from many aspects including mathematics, biology, biochemical, engineering, over the last couple of decades. Most of the models consider fluid flows in micro-scale. It is essential to understand the flow behaviour under different model parameters and externally controllable conditions so that the model can be formulated precisely to describe the behaviour of the blood flow. Due to the advancement of technologies, many mathematical models have been proposed to investigate the flow behavior in micro-scale with various different geometries driven by pulsatile pressure force, and a lot of analytical and numerical solutions have been achieved. Nevertheless, some factors and problems still need to be investigated. This work will focus on establishing models taking into account boundary slip at micro-scale, and investigating the effect of boundary slip on the pulsatile blood flows.

CHAPTER 3

The Effect of Boundary Slip on the Transient Pulsatile Flow of a Modified Second-Grade Fluid

3.1 General Overview

In this chapter, we study a fluid-structure interaction problem, namely the effect of boundary slip on the flow of a non-Newtonian fluid through micro-channels. This problem has many applications and we particularly focus on blood flow in the cardiovascular system.

For the study of blood flow in arteries, two major types of constitutve models have been used. The first type of models is based on the microcontinuum or the structured continuum theories [86–91] in which the balance laws are used to determine the characteristics of blood motion. In the other type of models, blood is considered as a suspension and its flow is modeled by the non-Newtonian fluid mechanics. Due to the red blood cell(RBC) migration as shown experimentally, blood has been modeled as a two stage fluid by many researchers [92–94]. The first stage is a peripheral layer which is modeled as a Newtonian viscous fluid, while the other one is a centre core which is modeled as a non-Newtonian fluid. The effect of body acceleration and pulsatile conditions were taken into account under the same problem by Majhi and Nair [92, 95]. Later, Massoudi and Phuoc [96] used the (generalized) second-grade fluid constitutive model to describe the shear-thinning and normal stress effect ,and the behavior of blood flow near the wall is modeled by the Newtonian fluid model, while the behavior of the blood flow at the core is described by the second-grade fluid model.

In all of the above mentioned models, the so-called no-slip boundary condition is used, namely , the velocity of flow relative to the solid is zero on the fluid-solid

interface [97]. Although the no-slip condition is supported by many experimental results, the existence of slip of a fluid on the solid surface was also observed by many other researchers [98–105]. The Navier slip condition has been used by various researchers to describe boundary slip and is a more general boundary condition, in which the fluid velocity component tangential to the solid surface, relative to the solid surface, is proportional to the shear stress on the fluid-solid interface and the slip length. The surface characteristics constant, slip length, describes the "slipperiness" of the surface. Recently, we and many other researchers have investigated various flow problems of Newtonian fluids with the traditional no-slip and the Navier slip boundary conditions [97, 105–115], and it is found that the boundary slip and the slip parameter have significant influence on the flow of Newtonian fluids through micro-channels and tubes.

Motivated by the above mentioned work, we extend previous work on slip flows of Newtonian fluids [106,107] to the case involving both Newtonian and non-Newtonian fluid flow in the flow region. The contribution of this work includes establishment of the underlying boundary value problem for the problem, the derivation of an exact solution for a special case, and finding of the influence of the slip parameter on the flow profile and flow behavior. The rest of the chapter is organized as follows. In section 3.2, we present the underlying boundary value problem for the problem in dimensionless form. Then in section 3.3, we derive an exact solution for a special case. In section 3.4, we investigate numerically the effect of the slip parameter for the general case. Finally, a conclusion is given in section 3.5.

3.2 Mathematical Formulation

The flow of a fluid with no thermochemical and electromagnetic effects can be described by the conservation equations of mass and linear momentum, namely

$$\frac{\partial \rho}{\partial t} + \operatorname{div}(\rho \mathbf{v}) = 0, \tag{3.1}$$

$$\rho\left(\frac{\partial \mathbf{v}}{\partial t} + \mathbf{v} \cdot \nabla \mathbf{v}\right) = \operatorname{div}\mathbf{T} + \rho \mathbf{b} \tag{3.2}$$

where ρ is the density of the fluid, $\frac{\partial}{\partial t}$ is the partial derivative with respect to time, $\mathbf{v}$ is the velocity vector,$\mathbf{b}$ is the body force vector, $\mathbf{T}$ is the stress tensor.

The stress tensor is related to the velocity gradient by the constitutive equations. For a modified (generalized) second-grade fluid [96, 116, 117], the constitu-

tive equations can be expressed by

$$\mathbf{T} = -p\mathbf{I} + \Pi^{\frac{m}{2}}\left(\mu\mathbf{A_1} + \alpha_1\mathbf{A_2} + \alpha_2\mathbf{A_1^2},\right) \tag{3.3}$$

where m is a material parameter, $\Pi = \frac{1}{2}\text{tr}\mathbf{A_1^2}$ is the second invariant of $\mathbf{A_1}$, p is the fluid pressure, μ is the coefficient of viscosity, α_i are material moduli (the normal stress coefficients) and $\mathbf{A_i}$ are the kinematical tensors given by

$$\mathbf{A_1} = \mathbf{L} + \mathbf{L}^T \tag{3.4}$$

and

$$\mathbf{A_2} = \frac{\partial \mathbf{A_1}}{\partial t} + [\text{grad}(\mathbf{A_1})]\mathbf{v} + \mathbf{A_1}\mathbf{L} + (\mathbf{L})^T\mathbf{A_1} \tag{3.5}$$

in which $L = \text{grad } \mathbf{v}$ and the superscript T refers to matrix transposition.

For the axially symmetrical blood flow through a circular tube of radius b, we can assume that $\mathbf{v} = v(r,t)\mathbf{e_z}$, where z is the axial direction and r is the radial direction. Under the periodic body acceleration and an unsteady pulsatile pressure gradient [92,95], the momentum equation in the z-direction in the cylindrical polar coordinate (r,θ,z) is

$$\rho\frac{\partial v}{\partial t} = -\frac{\partial p}{\partial z} + \rho G + \frac{1}{r}\frac{\partial}{\partial r}(rT_{rz}). \tag{3.6}$$

The shear stress T_{rz} for a generalized second-grade fluid can be expressed by

$$T_{rz} = \begin{cases} \mu_1\left|\frac{\partial v_1}{\partial r}\right|^m\frac{\partial v_1}{\partial r} & 0 \le r \le a, \\ \mu_2\frac{\partial v_2}{\partial r} & a \le r \le b. \end{cases} \tag{3.7}$$

The approximate periodic form of the pressure gradient generated by the heart can be described by

$$-\frac{\partial p}{\partial z} = A_0 + A_1\cos\omega_p t, \tag{3.8}$$

where $A_0, A_1, \omega_p = 2\pi f_p$ and f_p are the constant component of the pressure gradient, the amplitude of the pressure fluctuation (establishing the systolic and diastolic pressures), the circular frequency and the frequency of pulse rate, respectively.

The body acceleration G can be approximated by

$$G = A_g\cos(\omega_b t + \phi), \tag{3.9}$$

where A_g is the amplitude, $f_b = \frac{\omega_b}{2\pi}$ is the frequency and ϕ is the lead angle of G

with respect to the action of the heart.

Substituting (3.7)-(3.9) into (3.6), the system of blood flow equations for a modified second-grade fluid in the z-direction, in the inner and outer core, becomes

$$\rho_1 \frac{\partial v_1}{\partial t} = A_0 + A_1 \cos \omega_p t + \rho A_g \cos(\omega_b t + \phi) + \frac{1}{r}\frac{\partial}{\partial r}(r\mu_1 \Big|\frac{\partial v_1}{\partial r}\Big|^m \frac{\partial v_1}{\partial r}), \quad \text{for} \quad 0 \le r \le a, \tag{3.10}$$

$$\rho_2 \frac{\partial v_2}{\partial t} = A_0 + A_1 \cos \omega_p t + \rho A_g \cos(\omega_b t + \phi) + \frac{1}{r}\frac{\partial}{\partial r}(r\mu_2 \frac{\partial v_2}{\partial r}), \quad \text{for} \quad a \le r \le b. \tag{3.11}$$

In order to completely define the problem, boundary and initial conditions are required. In this work, the Navier slip condition is applied. That is, on the solid-fluid interface $r = b$, the axial fluid velocity, relative to the solid surface, is proportional to the shear stress on the interface. As the fluid layer near the wall is modeled as a Newtonian fluid in our model, the shear stress on the boundary is related to the shear strain rate by $\sigma_{rz} = \mu_2 \frac{\partial v}{\partial z}$. Thus, the Navier slip condition can be written as

$$v_2(b,t) + l\frac{\partial v_2}{\partial t}(b,t) = 0, \tag{3.12}$$

where l is the slip parameter. Moreover, we assume that the slip parameter does not change along the axial direction.

On $r = 0$, the symmetry condition is introduced:

$$\frac{\partial v_1}{\partial r}(0,t) = 0. \tag{3.13}$$

On the interface between two different fluids, for continuous and smooth behavior of the velocity and shear stresses, we require

$$v_1(a,t) = v_2(a,t), \tag{3.14}$$

$$\Big[\mu_1 \Big|\frac{\partial v_1}{\partial r}\Big|^m \frac{\partial v_1}{\partial r}\Big](a,t) = \Big[\mu_2 \frac{\partial v_2}{\partial r}\Big](a,t). \tag{3.15}$$

The initial conditions are set to

$$v_1(r,0) = 0 = v_2(r,0) \tag{3.16}$$

which is essential for the numerical scheme adopted to estimate the time at which the pulsatile steady state is achieved.

To simplify the equations, we introduce the following non-dimensional variables and parameters

$$\bar{r} = \frac{r}{b}; \quad \bar{v} = \frac{v}{v_0}; \quad \bar{t} = \frac{\omega_p}{2\pi}t; \quad u_0 = \frac{A_0 b^2}{\mu_2}; \tag{3.17}$$

$$e = \frac{A_1}{A_0}; \quad \omega_r = \frac{\omega_b}{\omega_p}; \quad r_0 = \frac{a}{b}; \quad \bar{mu} = \mu\big(\frac{u_0}{b}\big)^m; \tag{3.18}$$

$$\rho^* = \frac{\rho_1}{\rho_2}; \quad \mu^* = \frac{\mu_2}{\bar{\mu}}; \quad C_1 = \frac{A_0 b^2}{\bar{\mu} u_0}; \quad C_2 = \rho_1 A_g \frac{b^2}{\bar{\mu} u_0} = \frac{\rho_1 A_g}{A_0} B_1; \tag{3.19}$$

$$\alpha = \frac{\rho_1 \omega_p b^2}{2\pi\bar{\mu}}; \quad \gamma = \frac{\rho_2 \omega_p b^2}{2\pi\bar{\mu}\mu^*} = \frac{\rho_2 \omega_p b^2 \rho_1}{2\pi\bar{\mu}\mu^*\rho_1} = \alpha\frac{\rho^*}{\mu^*}; \tag{3.20}$$

$$\hat{C_1} = \frac{A_0 b^2}{\bar{\mu} u_0 \mu^*} = \frac{C1}{\mu^*}; \quad \hat{C_2} = \frac{\rho_2 A_g b^2 \rho_1}{\bar{\mu} u_0 \mu^* \rho_1} = C_2\frac{\rho^*}{\mu^*}. \tag{3.21}$$

In terms of the non-dimensional variables and parameters, equations (3.10)-(3.16) can be written in the form of

$$\alpha\frac{\partial \bar{v_1}}{\partial \bar{t}} = C_1(1 + e\cos 2\pi\bar{t}) + C_2\cos(2\pi\omega_r\bar{t} + \phi) + \frac{1}{\bar{r}}\frac{\partial}{\partial \bar{r}}\Big[\bar{r}\Big|\frac{\partial \bar{v_1}}{\partial \bar{r}}\Big|^m \frac{\partial \bar{v_1}}{\partial \bar{r}}\Big], \quad \text{for} \quad 0 \le r \le r_0, \tag{3.22}$$

$$\gamma\frac{\partial \bar{v_2}}{\partial \bar{t}} = \bar{C_1}(1 + e\cos 2\pi\bar{t}) + \bar{C_2}\cos(2\pi\omega_r\bar{t} + \phi) + \frac{1}{\bar{r}}\frac{\partial}{\partial \bar{r}}\Big[\bar{r}\frac{\partial \bar{v_2}}{\partial \bar{r}}\Big], \quad \text{for} \quad r_0 \le r \le 1. \tag{3.23}$$

The boundary conditions and initial conditions, in dimensionless form, can be expressed by

$$\frac{\partial \bar{v_1}}{\partial \bar{r}}(0, \bar{t}) = 0; \tag{3.24}$$

$$b\bar{v_2}(1, t) + l\frac{\partial \bar{v_2}}{\partial \bar{r}}(1, \bar{t}) = 0; \tag{3.25}$$

$$\bar{v_1}(r_0, \bar{t}) = \bar{v_2}(r_0, \bar{t}); \tag{3.26}$$

$$\Big[\Big|\frac{\partial \bar{v_1}}{\partial \bar{r}}\Big|^m \frac{\partial \bar{v_1}}{\partial \bar{r}}\Big](r_0, \bar{t}) \;=\; \Big[\mu^* \frac{\partial \bar{v_2}}{\partial \bar{r}}\Big](r_0, \bar{t}). \tag{3.27}$$

$$\bar{v_1}(r, 0) = \quad 0 \quad = \bar{v_2}(r, 0). \tag{3.28}$$

3.3 Analytical Solutions

For $m = 0$, the model reduces to the linear model with different viscosity in the peripheral layer and the centre core. In this case, equations (3.22) and (3.23) have the same form:

$$L(v) = \beta \frac{\partial v}{\partial t} - \frac{1}{r}\frac{\partial v}{\partial r} - \frac{\partial^2 v}{\partial r^2} = B_1(1 + e\cos(2\pi t)) + B_2 \cos(2\pi\omega_r t + \phi) \tag{3.29}$$

By the superposition principle, if v_0, v_1 and v_2 are the solution of $L(v) = f(t)$ for $f(t) = B_1 \exp(0ti), B_1 a \exp(2\pi ti)$ and $B_2 \exp((2\pi\omega_r t + \phi)i)$, then the complete solution of equation (3.29) is $v = \sum_{n=0}^{2} \mathrm{Re}(v_n)$

To determine v_n, we solve

$$\beta \frac{\partial v_n}{\partial t} = D_n \exp(g_n(t)i) + \frac{1}{r}\frac{\partial v_n}{\partial r} + \frac{\partial^2 v_n}{\partial r^2}, \tag{3.30}$$

where $g_0(t) = 0, g_1(t) = 2\pi t, g_2(t) = 2\pi\omega_r t + \phi, D_0 = B_1, D_1 = eB_1$ and $D_2 = B_2$. As equation(3.30) admits solutions of the form $v_n = f_n(r)e^{g_n(t)i}$, we have

$$\frac{\partial v}{\partial t} = f_n(r)[i g_n'(t) \exp(g_n(t)i)], \tag{3.31}$$

$$\frac{\partial v}{\partial r} = f_n'(r) \exp(g_n(t)i), \tag{3.32}$$

$$\frac{\partial^2 v}{\partial r^2} = f_n''(r) \exp(g_n(t)i). \tag{3.33}$$

Substituting (3.31) - (3.33) into (3.30) yields,

$$\beta g_n'(t) f_n(r) \exp(g_n(t)i)i = D_n \exp(g_n(t)i) + \frac{1}{r} f_n'(r) \exp(g_n(t)i) + f_n''(r) \exp(g_n(t)i). \tag{3.34}$$

Dividing by $\exp(g_n(t)i)$ on both sides of eq.(3.34), we obtain

$$\beta g_n'(t) f_n(r)i = D_n + \frac{1}{r} f_n'(r) + f_n''(r). \tag{3.35}$$

For $n = 0$, equation (3.35) becomes

$$f_0''(r) + \frac{1}{r} f_0'(r) - i\beta g_0'(t) f_0(r) = -D_0 \tag{3.36}$$

As $g_0(t) = 0$, by rearranging equation (3.36) and substituting $B_1 = D_0$, we get

$$f_0''(r) + \frac{1}{r} f_0'(r) = -B_1, \tag{3.37}$$

which gives

$$(r f_0'(r))' = -B_1 r. \tag{3.38}$$

Integrating both sides of equation (3.38), we have

$$r f_0'(r) = -\frac{1}{2} B_1 r^2 + c_2. \tag{3.39}$$

Dividing by r on both sides and integrating the equation (3.39) , we have the general solution

$$f_0(r) = (c_1 + c_2 \ln r) - \frac{B_1}{4} r^2. \tag{3.40}$$

Hence, $v_0(r,t) = f_0(r) = -B_1 \frac{r^2}{4} + c_2 \ln r + c_1$
For $n = 1$, we have

$$f_1''(r) + \frac{1}{r} f_1'(r) - 2\pi\beta i f_1(r) = -eB_1. \tag{3.41}$$

Let $\bar{\beta_1}^2 = -2\pi\beta i$, then

$$\frac{1}{\bar{\beta_1}^2} f_1''(r) + \frac{1}{\bar{\beta_1}^2 r} f_1'(r) + f_1(r) = -\frac{eB_1}{\bar{\beta_1}^2}. \tag{3.42}$$

Let $\hat{r} = \bar{\beta_1} r$, then by using the chain rule for differentiation, we have

$$f_1'(r) = \frac{df_1(r)}{dr} = \frac{df_1(\hat{r})}{d\hat{r}} \frac{d\hat{r}}{dr} = f_1'(\hat{r}) \bar{\beta_1}, \tag{3.43}$$

$$f_1''(r) = \frac{df_1'(r)}{dr} = \frac{d\bar{\beta_1} f_1'(\hat{r})}{d\hat{r}} \frac{d\hat{r}}{dr} = f_1''(r) \bar{\beta_1}^2. \tag{3.44}$$

Hence, equation (3.42) becomes

$$\hat{r}^2 f_1''(\hat{r}) + \hat{r} f_1'(\hat{r}) + \hat{r}^2 f_1(\hat{r}) = -\frac{eB_1}{\bar{\beta_1}^2} \hat{r}^2, \tag{3.45}$$

The associated homogeneous equation of (3.45) is a Bessel equation and has solution as follows

$$f_1^h(\hat{r}) = d_1 J_0(\hat{r}) + e_1 Y_0(\hat{r}), \tag{3.46}$$

where $J_0(\hat{r})$ and $Y_0(\hat{r})$ are respectively the zero-order Bessel functions of the first kind and the second kind.

For the particular solution of the equation (3.45), we assume $f_1^p(\hat{r}) = Q$ (constant). By substituting into the equation, we have

$$f_1^p(\hat{r}) = -\frac{eB_1}{\bar{\beta_1}^2} = -\frac{eB_1}{2\pi\beta} i. \tag{3.47}$$

Since $f_1(r) = f_1(\hat{r}) = f_1^h(\hat{r}) + f_1^p(\hat{r})$, the general solution of equation (3.41) is

$$f_1(r) = d_1 J_0(\bar{\beta_1} r) + e_1 Y_0(\bar{\beta_1} r) - \frac{eB_1}{2\pi\beta} i, \tag{3.48}$$

where d_1 and e_1 are integration constants.

Similarly, for $n = 2$, we have

$$f_2''(r) + \frac{1}{r} f_2'(r) - 2\beta\pi\omega_r f_2(r) i = -B_2 \tag{3.49}$$

and the general solution is

$$f_2 = d_2 J_0(\bar{\beta_2} r) + e_2 Y_0(\bar{\beta_2} r) - \frac{B_2}{2\beta\omega_r \pi} i, \tag{3.50}$$

where $\bar{\beta_2}^2 = -2\pi\beta\omega_r i$.

Because of the boundness of v_1 and v_2, c_2 and e_1 as well as e_2 are set to zero. Hence, from eq.(3.22)-(3.23) and the solutions of equation(3.29), we have

$$\begin{aligned} \bar{v_1} =& \mathrm{Re}\big\{ c_1 - \frac{C_1}{4}\bar{r}^2 + [d_1 J_0(\beta_1 \bar{r}) - \frac{eC_1}{2\pi\alpha} i] \exp(2\pi \bar{t} i) + [d_2 J_0(\beta_2 \bar{r}) \\ & - \frac{C_2}{2\pi\omega_r \alpha} i] \exp((2\pi\omega_r \bar{t} + \phi) i) \big\}, \end{aligned} \tag{3.51}$$

$$\begin{aligned} \bar{v_2} =& \mathrm{Re}\big\{ \hat{c_1} + \hat{c_2} \ln \bar{r} - \frac{\bar{C_1}}{4}\bar{r}^2 + [\hat{d_1} J_0(\hat{\beta_1}\bar{r}) + \hat{e_1} Y_0(\hat{\beta_1}\bar{r}) - \frac{e\hat{C_1}}{2\pi\gamma} i] \exp(2\pi \bar{t} i) \\ & + [\hat{d_2} J_0(\hat{\beta_2}\bar{r}) + \hat{e_2} Y_0(\hat{\beta_2}\bar{r}) - \frac{\bar{C_2} i}{2\pi\omega_r \gamma}] \exp((2\pi\omega_r \bar{t} + \phi) i) \big\}, \end{aligned} \tag{3.52}$$

where $\hat{\beta}_1^2 = -2\pi\gamma i$, $\hat{\beta}_2^2 = -2\pi\omega_r\gamma i$,$\beta_1^2 = -2\pi\alpha i$ and $\beta_2^2 = -2\pi\omega_r\alpha i$

As $\frac{dJ_0(x)}{dx} = -J_1(x)$ and $\frac{dY_0(x)}{dx} = -Y_0(x)$, we have

$$\frac{\partial\bar{v_1}}{\partial\bar{r}} = \mathrm{Re}(-\frac{C_1}{2}\bar{r} - d_1\beta_1 J_1(\beta_1\bar{r})\exp(2\pi\bar{t}i) - d_2\beta_2 J_1(\beta_2\bar{r})\exp((2\pi\omega_r\bar{t}+\phi)i)), \tag{3.53}$$

$$\frac{\partial\bar{v_2}}{\partial\bar{r}} = \mathrm{Re}(\hat{c_2}\frac{1}{\bar{r}} - \frac{\bar{C_1}}{2}\bar{r} + [-\hat{d_1}\hat{\beta}_1 J_1(\hat{\beta}_1\bar{r}) - \hat{e_1}\hat{\beta}_1 Y_1(\hat{\beta}_1\bar{r})]\exp(2\pi\bar{t}i)$$

$$+ [-\hat{d_2}\hat{\beta}_2 J_1(\hat{\beta}_2\bar{r}) - \hat{e_2}\hat{\beta}_2 Y_1(\hat{\beta}_2\bar{r})]\exp((2\pi\omega_r\bar{t}+\phi)i)). \tag{3.54}$$

Obviously, v_1 satisfies the boundary condition (3.24) automatically. We now consider the boundary condition (3.25), namely

$$\mathrm{Re}[(b\hat{c_1} + l\hat{c_2} - (l+\frac{b}{2})\frac{\bar{C_1}}{2}) + ((bJ_0(\hat{\beta}_1) - l\hat{\beta}_1 J_1(\hat{\beta}_1))\hat{d_1} + (bY_0(\hat{\beta}_1)$$

$$- l\hat{\beta}_1 Y_1(\hat{\beta}_1))\hat{e_1} - \frac{eb\bar{C_1}i}{2\pi\gamma})\exp(2\pi\bar{t}i) + (\hat{d_2}(bJ_0(\hat{\beta}_2) - l\hat{\beta}_2 J_1(\hat{\beta}_2)) + \hat{e_2}(bY_0(\hat{\beta}_2)$$

$$- l\hat{\beta}_2 Y_1(\hat{\beta}_2)) - \frac{b\bar{C_2}}{2\pi\omega_r\gamma}i)\exp((2\pi\omega_r\bar{t}+\phi)i)] = 0. \tag{3.55}$$

Further, from boundary conditions (3.26) and (3.27), we have

$$\mathrm{Re}[(c_1 - \hat{c_1} - \hat{c_2}\ln r_0 - (C_1 - \hat{C_1})\frac{r_0^2}{4}) + (d_1 J_0(\beta_1 r_0) - \hat{d_1} J_0(\hat{\beta}_1 r_0)$$

$$- \hat{e_1} Y_0(\hat{\beta}_1 r_0) - (\gamma C_1 - \alpha\bar{C_1})\frac{ei}{2\pi\alpha\gamma})\exp(2\pi\bar{t}i) + (d_2 J_0(\beta_2 r_0) - \hat{d_2} J_0(\hat{\beta}_2 r_0)$$

$$- \hat{e_2} Y_0(\hat{\beta}_2 r_0) - (\gamma C_2 - \alpha\bar{C_2})\frac{i}{2\pi\omega_r\gamma\alpha})\exp((2\pi\omega_r\bar{t}+\phi)i)] = 0, \tag{3.56}$$

$$\mathrm{Re}[\big((\mu^*\bar{C_1} - C1)\frac{r_0}{2} - \mu^*\frac{\hat{c_2}}{r_0}\big) + (-d_1\beta_1 J_1(\beta_1 r_0) + \hat{d_1}\mu^*\hat{\beta}_1 J_1(\hat{\beta}_1 r_0)$$

$$+ \hat{e_1}\mu^*\hat{\beta}_1 Y_1(\hat{\beta}_1 r_0))\exp(2\pi\bar{t}i) + (-d_2\beta_2 J_1(\beta_2 r_0) + \hat{d_2}\mu^*\hat{\beta}_2 J_1(\hat{\beta}_2 r_0)$$

$$+ \hat{e_2}\mu^*\hat{\beta}_2 Y_1(\hat{\beta}_2 r_0))\exp((2\pi\omega_r\bar{t} + \phi)i)] = 0 \tag{3.57}$$

As equations (3.55) - (3.57) must be satisfied for any instant of time t, we require that the constant terms and the coefficients of the exponential terms all vanish, namely

$$b\hat{c_1} + l\hat{c_2} - (l + \frac{b}{2})\frac{\bar{C_1}}{2} = 0 \tag{3.58}$$

$$c_1 - \hat{c_1} - \hat{c_2}\ln r_0 - (C_1 - \bar{C_1})\frac{r_0^2}{4} = 0 \tag{3.59}$$

$$(\mu^*\bar{C_1} - C_1)\frac{r_0}{2} - \mu^*\frac{\hat{c_2}}{r_0} = 0 \tag{3.60}$$

$$\hat{d_1}(bJ_0(\hat{\beta}_1) - l\hat{\beta}_1 J_1(\hat{\beta}_1)) + \hat{e_1}(bY_0(\hat{\beta}_1) - l\hat{\beta}_1 Y_1(\hat{\beta}_1)) - \frac{eb\bar{C_1}}{2\pi\gamma}i = 0 \tag{3.61}$$

$$d_1 J_0(\beta_1 r_0) - \hat{d_1}J_0(\hat{\beta}_1 r_0) - \hat{e_1}Y_0(\hat{\beta}_1 r_0) - \frac{eC_1}{2\pi\alpha}i + \frac{e\bar{C_1}}{2\pi\gamma}i = 0 \tag{3.62}$$

$$-d_1\beta_1 J_1(\beta_1 r_0) + \hat{d_1}\mu^*\hat{\beta}_1 J_1(\hat{\beta}_1 r_0) + \hat{e_1}\mu^*\hat{\beta}_1 Y_1(\hat{\beta}_1 r_0) = 0 \tag{3.63}$$

$$\hat{d_2}(bJ_0(\hat{\beta}_2) - l\hat{\beta}_2 J_1(\hat{\beta}_2)) + \hat{e_2}(bY_0(\hat{\beta}_2) - l\hat{\beta}_2 Y_1(\hat{\beta}_2)) - \frac{b\bar{C}_2}{2\pi\omega_r\gamma}i = 0 \tag{3.64}$$

$$d_2 J_0(\beta_2 r_0) - \hat{d_2}J_0(\hat{\beta}_2 r_0) - \hat{e_2}Y_0(\hat{\beta}_2 r_0) - \frac{C_1}{2\pi\omega_r\alpha}i + \frac{\bar{C}_2}{2\pi\omega_r\gamma}i = 0 \tag{3.65}$$

$$-d_2\beta_2 J_1(\beta_2 r_0) + \hat{d_2}\mu^*\hat{\beta}_2 J_1(\hat{\beta}_2 r_0) + \hat{e_2}\mu^*\hat{\beta}_2 Y_1(\hat{\beta}_2 r_0) = 0. \tag{3.66}$$

Solving the above system of equations by Cramer's Rule yields

$$c_1 =(\ln r_0 - \frac{l}{b})((\mu^*\bar{C}_1 - C_1)\frac{r_0^2}{2\mu^*}) + (\frac{l}{b} + \frac{1-r_0^2}{2})\frac{\bar{C}_1}{2} + C_1\frac{r_0^2}{4} \tag{3.67}$$

$$\hat{c_1} =-\frac{l}{b}((\mu^*\bar{C}_1 - C_1)\frac{r_0^2}{2\mu^*}) + (\frac{l}{b} + \frac{1}{2})\frac{\bar{C}_1}{2} \tag{3.68}$$

$$\hat{c_2} =(\mu^*\bar{C}_1 - C_1)\frac{r_0^2}{2\mu^*} \tag{3.69}$$

$$\begin{aligned} d_1 =&\mu^*\big[(J_1(\hat{\beta}_1 r_0)Y_0(\hat{\beta}_1 r_0) - J_0(\hat{\beta}_1 r_0)Y_1(\hat{\beta}_1 r_0))\frac{eb\hat{\beta}_1\bar{C}_1 i}{2\pi\gamma} + (\gamma C_1 \\ &- \alpha\bar{C}_1)[J_1(\hat{\beta}_1 r_0)(bY_0(\hat{\beta}_1) - l\hat{\beta}_1 Y_1(\hat{\beta}_1)) - Y_1(\hat{\beta}_1 r_0)(bJ_0(\hat{\beta}_1) \\ &- l\hat{\beta}_1 J_1(\hat{\beta}_1))]\frac{\hat{\beta}_1 ei}{2\pi\gamma\alpha}\big]/(bJ_0(\hat{\beta}_1) - l\hat{\beta}_1 J_1(\hat{\beta}_1))(\beta_1 J_1(\beta_1 r_0)Y_0(\hat{\beta}_1 r_0) \\ &- \mu^*\hat{\beta}_1 Y_1(\hat{\beta}_1 r_0)J_0(\beta_1 r_0)) + (bY_0(\hat{\beta}_1) \\ &- l\hat{\beta}_1 Y_1(\hat{\beta}_1))(\mu^*\hat{\beta}_1 J_0(\beta_1 r_0)J_1(\hat{\beta}_1 r_0) - \beta_1 J_1(\beta_1 r_0)J_0(\hat{\beta}_1 r_0)) \end{aligned} \tag{3.70}$$

$$\begin{aligned} \hat{d_1} =&[(\beta_1 J_1(\beta_1 r_0)Y_0(\hat{\beta}_1 r_0) - \mu^*\hat{\beta}_1 Y_1(\hat{\beta}_1 r_0)J_0(\beta_1 r_0))\frac{eb\bar{C}_1}{2\pi\gamma}i \\ &+ \frac{(\gamma C_1 - \alpha\bar{C}_1)}{2\pi\gamma\alpha}(bY_0(\hat{\beta}_1) - l\hat{\beta}_1 Y_1(\hat{\beta}_1))e\beta_1 J_1(\beta_1 r_0)i]/(bJ_0(\hat{\beta}_1) \\ &- l\hat{\beta}_1 J_1(\hat{\beta}_1))(\beta_1 J_1(\beta_1 r_0)Y_0(\hat{\beta}_1 r_0) - \mu^*\hat{\beta}_1 Y_1(\hat{\beta}_1 r_0)J_0(\beta_1 r_0)) \\ &+ (bY_0(\hat{\beta}_1) - l\hat{\beta}_1 Y_1(\hat{\beta}_1))(\mu^*\hat{\beta}_1 J_0(\beta_1 r_0)J_1(\hat{\beta}_1 r_0) \\ &- \beta_1 J_1(\beta_1 r_0)J_0(\hat{\beta}_1 r_0)) \end{aligned} \tag{3.71}$$

$$\begin{aligned}\hat{e_1} =&[(\mu^*\hat{\beta}_1 J_0(\beta_1 r_0)J_1(\hat{\beta}_1 r_0) - \beta_1 J_0(\hat{\beta}_1 r_0)J_1(\beta_1 r_0))\frac{eb\bar{C_1}i}{2\pi\gamma} - (bJ_0(\hat{\beta}_1)\\ &- l\hat{\beta}_1 J_1(\hat{\beta}_1))(\gamma C_1 - \alpha\bar{C_1})J_1(\beta_1 r_0)\frac{\beta_1 ei}{2\pi\alpha\gamma}]/(bJ_0(\hat{\beta}_1)\\ &- l\hat{\beta}_1 J_1(\hat{\beta}_1))(\beta_1 J_1(\beta_1 r_0)Y_0(\hat{\beta}_1 r_0) - \mu^*\hat{\beta}_1 Y_1(\hat{\beta}_1 r_0)J_0(\beta_1 r_0))\\ &+ (bY_0(\hat{\beta}_1) - l\hat{\beta}_1 Y_1(\hat{\beta}_1))(\mu^*\hat{\beta}_1 J_0(\beta_1 r_0)J_1(\hat{\beta}_1 r_0)\\ &- \beta_1 J_1(\beta_1 r_0)J_0(\hat{\beta}_1 r_0))\end{aligned} \tag{3.72}$$

$$\begin{aligned}d_2 =&\mu^*\big[(J_1(\hat{\beta}_2 r_0)Y_0(\hat{\beta}_2 r_0) - J_0(\hat{\beta}_2 r_0)Y_1(\hat{\beta}_2 r_0))\frac{b\hat{\beta}_2\bar{C}_1 i}{2\pi\omega_r\gamma} + (\gamma C_2\\ &- \alpha\bar{C_2})[J_1(\hat{\beta}_2 r_0)(bY_0(\hat{\beta}_2) - l\hat{\beta}_2 Y_1(\hat{\beta}_2)) - Y_1(\hat{\beta}_2 r_0)(bJ_0(\hat{\beta}_2)\\ &- l\hat{\beta}_2 J_1(\hat{\beta}_2))]\frac{\hat{\beta}_2 i}{2\pi\omega_r\gamma\alpha}\big]/(bJ_0(\hat{\beta}_2) - l\hat{\beta}_2 J_1(\hat{\beta}_2))(\beta_2 J_1(\beta_2 r_0)Y_0(\hat{\beta}_2 r_0)\\ &- \mu^*\hat{\beta}_2 Y_1(\hat{\beta}_2 r_0)J_0(\beta_2 r_0)) + (bY_0(\hat{\beta}_2)\\ &- l\hat{\beta}_2 Y_1(\hat{\beta}_2))(\mu^*\hat{\beta}_2 J_0(\beta_2 r_0)J_1(\hat{\beta}_2 r_0) - \beta_2 J_1(\beta_2 r_0)J_0(\hat{\beta}_2 r_0))\end{aligned} \tag{3.73}$$

$$\begin{aligned}\hat{d_2} =&[(\beta_2 J_1(\beta_2 r_0)Y_0(\hat{\beta}_2 r_0) - \mu^*\hat{\beta}_2 Y_1(\hat{\beta}_2 r_0)J_0(\beta_2 r_0))\frac{b\bar{C}_1}{2\pi\omega_r\gamma}i\\ &+ \frac{(\gamma C_1 - \alpha\bar{C_1})}{2\pi\gamma\alpha\omega_r}(bY_0(\hat{\beta}_2) - l\hat{\beta}_2 Y_1(\hat{\beta}_2))\beta_2 J_1(\beta_2 r_0)i]/(bJ_0(\hat{\beta}_2)\\ &- l\hat{\beta}_2 J_1(\hat{\beta}_2))(\beta_2 J_1(\beta_2 r_0)Y_0(\hat{\beta}_2 r_0) - \mu^*\hat{\beta}_2 Y_1(\hat{\beta}_2 r_0)J_0(\beta_2 r_0))\end{aligned}$$

$$+ (bY_0(\hat{\beta}_2) - l\hat{\beta}_2 Y_1(\hat{\beta}_2))(\mu^* \hat{\beta}_2 J_0(\beta_2 r_0) J_1(\hat{\beta}_2 r_0)$$

$$- \beta_2 J_1(\beta_2 r_0) J_0(\hat{\beta}_2 r_0)) \tag{3.74}$$

$$\hat{e_2} = [(\mu^* \hat{\beta}_2 J_0(\beta_2 r_0) J_1(\hat{\beta}_2 r_0) - \beta_2 J_0(\hat{\beta}_2 r_0) J_1(\beta_2 r_0)) \frac{b\bar{C_1} i}{2\pi\omega_r \gamma} - (bJ_0(\hat{\beta}_2)$$

$$- l\hat{\beta}_2 J_1(\hat{\beta}_2))(\gamma C_1 - \alpha \bar{C_1}) J_1(\beta_2 r_0) \frac{\beta_2 i}{2\pi\omega_r \alpha\gamma}]/(bJ_0(\hat{\beta}_2)$$

$$- l\hat{\beta}_2 J_1(\hat{\beta}_2))(\beta_2 J_1(\beta_2 r_0) Y_0(\hat{\beta}_2 r_0) - \mu^* \hat{\beta}_2 Y_1(\hat{\beta}_2 r_0) J_0(\beta_2 r_0))$$

$$+ (bY_0(\hat{\beta}_2) - l\hat{\beta}_2 Y_1(\hat{\beta}_2))(\mu^* \hat{\beta}_2 J_0(\beta_2 r_0) J_1(\hat{\beta}_2 r_0)$$

$$- \beta_2 J_1(\beta_2 r_0) J_0(\hat{\beta}_2 r_0)) \tag{3.75}$$

To study the flow behavior and the effect of the slip parameters, we investigate the velocity profiles in the arteries with different values of the slip parameter under various different conditions. In the first example of investigation, the radius of the artery is taken as $r = b = 0.15$ cm., and the other parameters are set to $A_0 = 698.65$ dyne/cm^3, $A_g = 0.5g, f_b = f_p = 1.2, \phi = 0, C_1 = 6.6, C_2 = 4.64, A_1 = 1.2A_0$ and $\rho_1/\rho_2 = 1$. Figures 3.1 and 3.2 show the velocity profile as a function of time and location, and the velocity profile as a function of time at three different radial locations for two different slip parameters $l = 0$ (no-slip) and $l = 2$. The results show that boundary slip has very dramatical effect on the fluid flow in the artery. It affects not only the magnitude of the flow velocity significantly, but also the flow pattern and velocity profile on the cross-section of the artery. For the no-slip flow ($l_b = 0$), the pulsatile flow nature gradually disappears toward the arterial wall; while with boundary slip, the flow near the arterial wall also displays a pulsatile nature.

We then investigate whether the above observed flow phenomena associated with boundary slip is affected or not by the radius of the artery, and for this purpose, we consider the fluid flow through an artery with a larger radius $r = 0.5$ cm. The constant pressure gradient is set to $A_0 = 32$ dyne/cm^3 in order to achieve a mean velocity magnitude approximately equal to that in the smaller artery; while all other parameters are set to the same values as those used for

the smaller radius. Figures 3.3 and 3.4 show the velocity profile in the artery for two different slip parameter values including $l_b = 0$ (no-slip) and $l_b = 2$. The 3-dimensional graph shows the variation of the flow velocity with time and radial position; while the 2-dimensional graphs demonstrate the variation of the flow velocity with time at three different radial locations including $r = 0$ (centre), $r = 0.6$ (inner-outer layers interface) and $r = 1$ (arterial wall). From Figures 3.1 - 3.4, it is clear that the boundary slip affects the flow phenomena and behavior observed for the smaller artery and also appears in the artery with a larger radius; and further a more significant pulsatile nature of fluid flow is observed for the larger artery.

To further investigate the effect of the slip parameter on the velocity profile near the artery wall, we show in Figure 3.5 the velocity of fluid on the artery wall for five different values of the slip parameter including $l_b = 0, 2, 4, 6$ and 8. The results clearly demonstrate that the slip parameter has very significant effect on the near-wall velocity, and that the magnitude of the average wall velocity is proportional to the slip parameter.

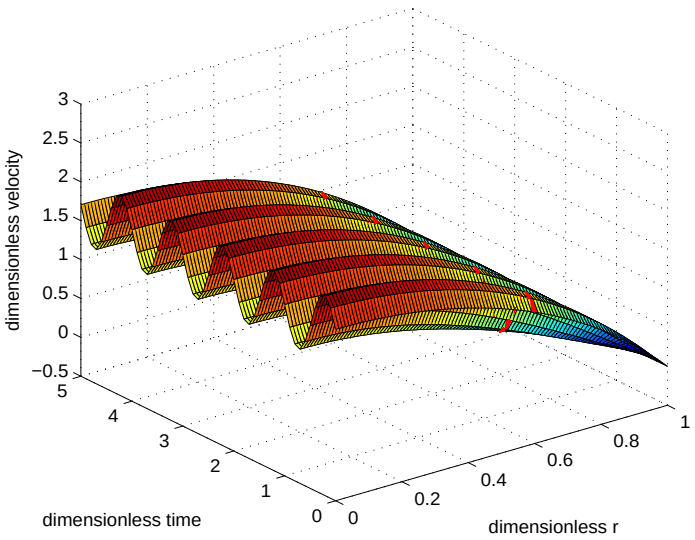

(a)

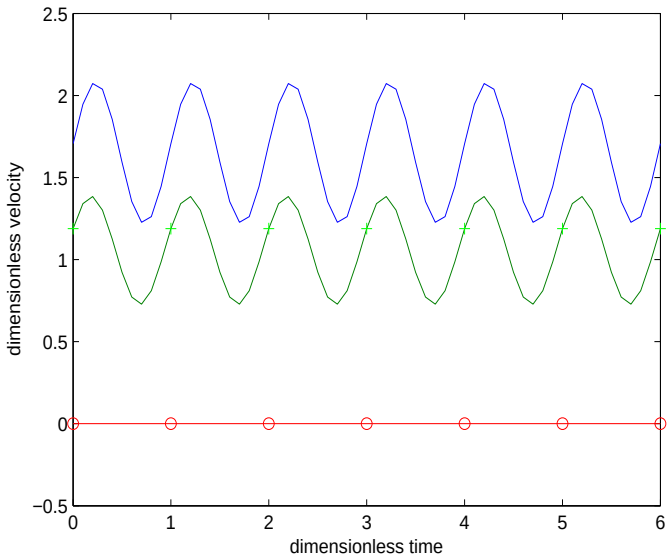

(b)

——— $r = 0$; ——+—— $r = 0.6$; ——o—— $r = 1$

Figure 3.1: The velocity profile in the small artery with radius 0.15 cm under slip parameter values $l_b = 0$. In the figure, the 3D graph shows the variation of velocity as a function of time and location; while the 2D graphs show the variation of velocity with time at three radial locations including the artery centre ($r = 0$), the interface of inner-outer layer ($r = 0.6$), and the arterial wall ($r = 1$).

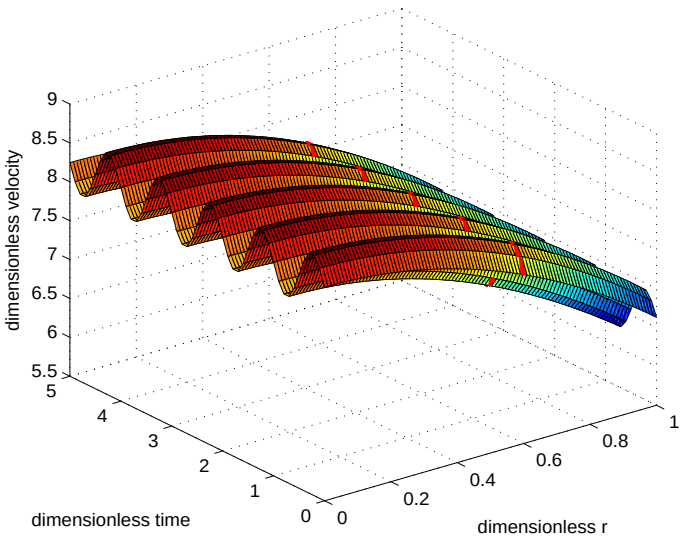

(a)

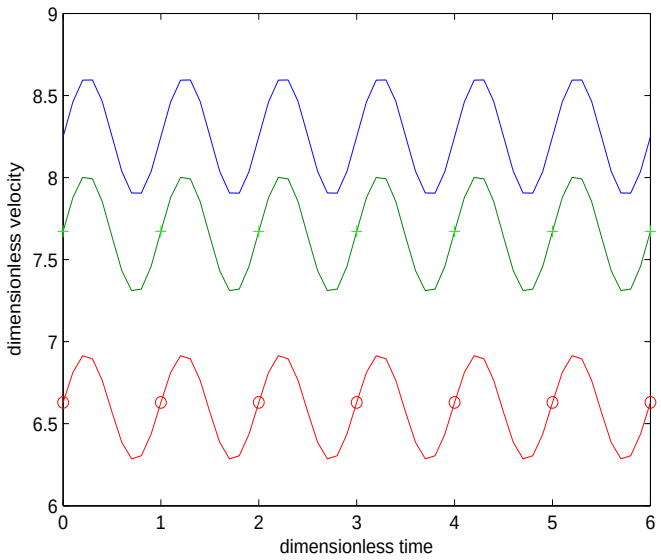

(b)

——— $r = 0$; ——+—— $r = 0.6$; ——o—— $r = 1$

Figure 3.2: The velocity profile in the small artery with radius 0.15 cm under slip parameter values $l_b = 2$. In the figure, the 3D graph shows the variation of velocity as a function of time and location; while the 2D graphs show the variation of velocity with time at three radial locations including the artery centre ($r = 0$), the interface of inner-outer layer ($r = 0.6$), and the arterial wall ($r = 1$).

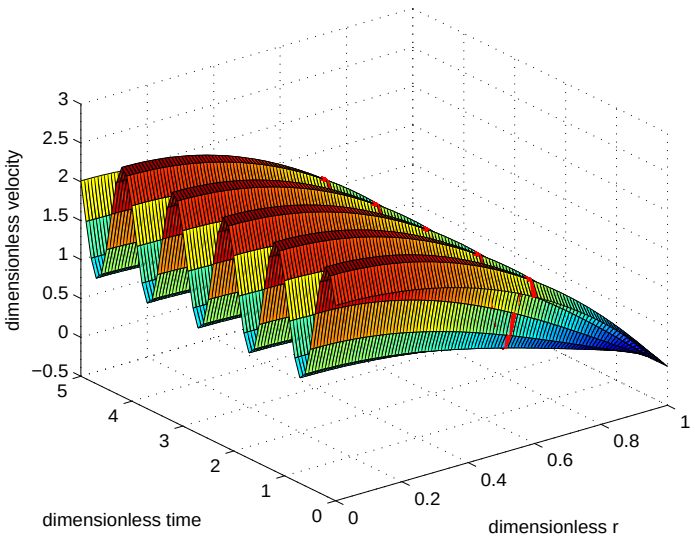

(a)

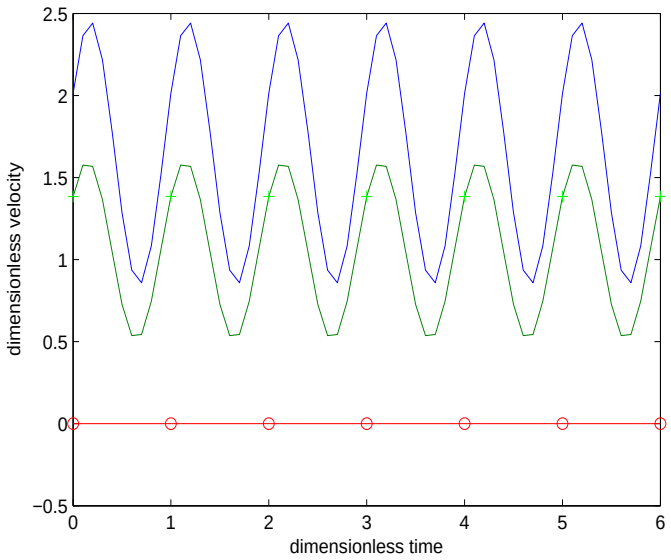

(b)

——— $r = 0$; ——+—— $r = 0.6$; ——o—— $r = 1$

Figure 3.3: The velocity profile in the large artery with radius 0.50 cm under slip parameter values $l_b = 0$. In the figure, the 3D graph shows the variation of velocity as a function of time and location; while the 2D graphs show the variation of velocity with time at three radial locations including the artery centre ($r = 0$), the interface of inner-outer layer ($r = 0.6$), and the arterial wall ($r = 1$).

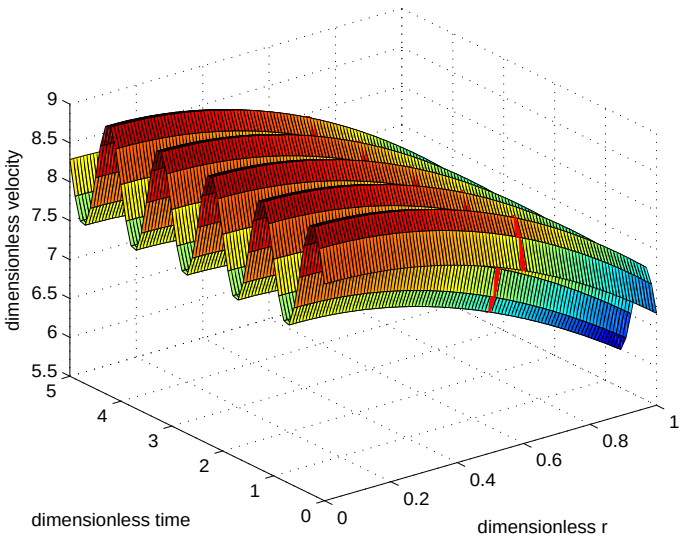

(a)

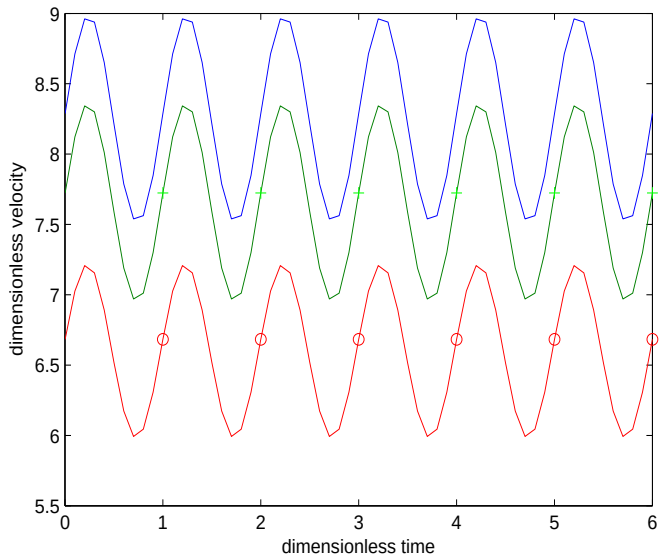

(b)

——— $r = 0$; ——+—— $r = 0.6$; ——o—— $r = 1$

Figure 3.4: The velocity profile in the large artery with radius 0.50 cm under slip parameter values $l_b = 2$. In the figure, the 3D graph shows the variation of velocity as a function of time and location; while the 2D graphs show the variation of velocity with time at three radial locations including the artery centre ($r = 0$), the interface of inner-outer layer ($r = 0.6$), and the arterial wall ($r = 1$).

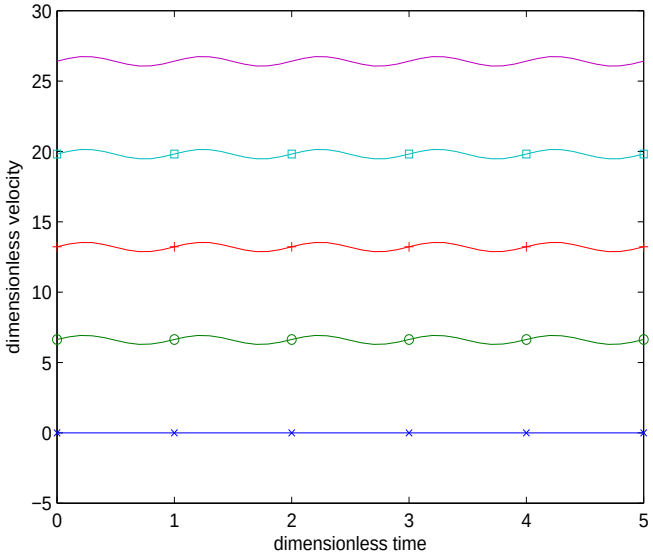

(a)

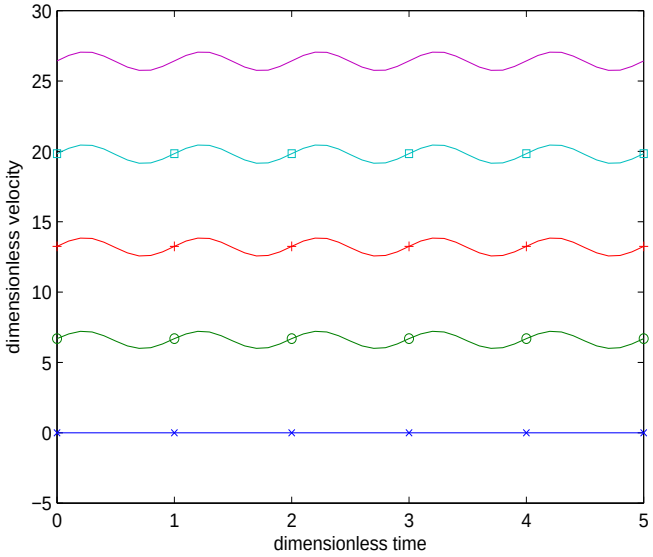

(b)

—×— $l_b = 0$; —○— $l_b = 2$; —+— $l_b = 4$;
—□— $l_b = 6$; ——— $l_b = 8$

Figure 3.5: Diagram showing the velocity profile on the arterial wall with five different slip parameters l_b for two different artery radius (a) $r = 0.15$ cm; (b) $r = 0.5$ cm.

3.4 Numerical Investigation

The following numerical scheme, based on the equidistance finite different method, is established to solve the underlying boundary value problem for the general case $m \neq 0$, consisting of equations (3.22) and (3.23) and boundary conditions (3.24) - (3.28).

$$\frac{\partial v}{\partial t} = \frac{v_1^{j+1} - v_i^j}{t_{i+1} - t_i} \tag{3.76}$$

$$\frac{\partial v}{\partial r} = \begin{cases} \frac{v_{1+1}^j - v_{i-1}^j}{r_{i+1} - r_{i-1}}, & \text{for interior points} \\ \frac{v_{1+1}^j - v_i^j}{r_{i+1} - r_i}, & \text{for boundary points} \end{cases} \tag{3.77}$$

$$\frac{\partial^2 v}{\partial r^2} = \frac{v_{i+1}^j - 2v_i^j + v_{i-1}^j}{r_{i+1} - r_i} \tag{3.78}$$

To validate the numerical technique, we apply the numerical scheme to generate a series of numerical solutions for the case $m = 0$, and then compare the numerical results with the exact solution derived in section 3.3.

Figures 3.6 and 3.7 present the velocity profile in the small and large arteries for two different slip parameters $l_b = 0$ (no-slip) and $l_b = 2$ obtained by the numerical technique. The numerical errors between the exact solution and the numerical solution, $E_r = V - U$, are presented in Figures 3.8 and 3.9 in which V is the exact solution and U is the numerical solution. The results clearly indicate that the numerical solution converges to the exact solution. It also shows that a larger slip length has a lower convergence rate.

We then investigate the flow phenomena for the general case $m \neq 0$, and here we consider $m = -\frac{1}{4}$ in the investigation. Figures 3.10 and 3.11 give the 3D graph showing the convergence of the transient velocity field to a steady state pulsatile velocity field, and also demonstrating the substantial influence of boundary slip on the steady state velocity profile in both magnitude and flow pattern. Figure 7, showing the variation of velocity with time at three arterial locations for different slip parameters and artery radius, also clearly demonstrates the significant effect of boundary slip on the flow through the artery. Figure 8 shows the variation of fluid velocity along the artery wall under different slip parameters and artery radius. The results show that as the slip parameter increases, the time required

for achieving convergence results increases and the magnitude of the average steady state velocity also increases.

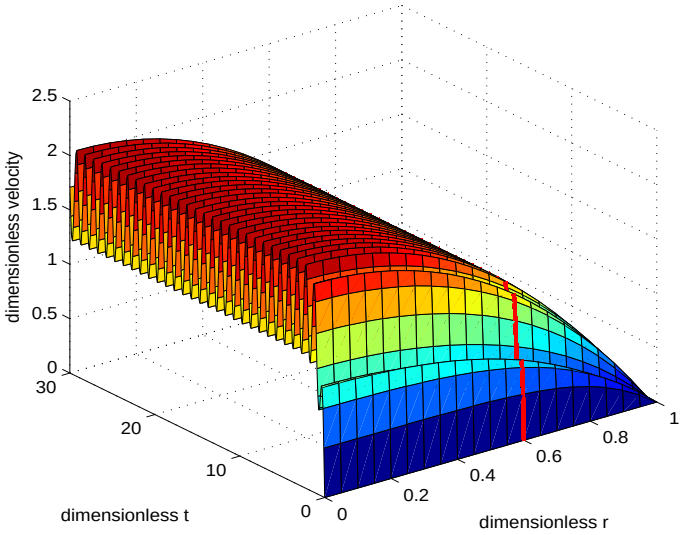

(a)

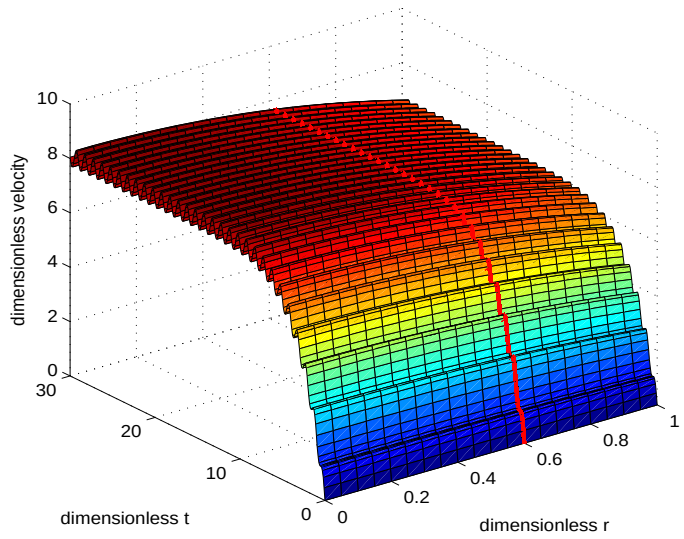

(b)

Figure 3.6: Velocity profiles in arteries with radius $r = 0.15$ cm for different slip parameter values (a) $l_b = 0$, (b) $l_b = 2$.

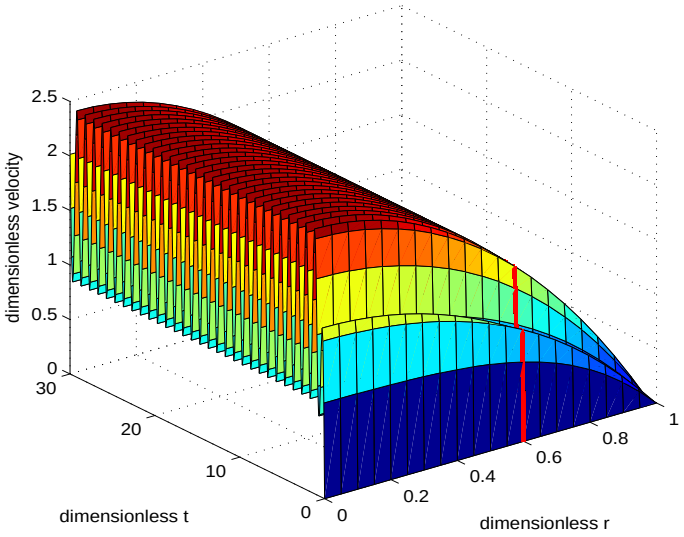

(a)

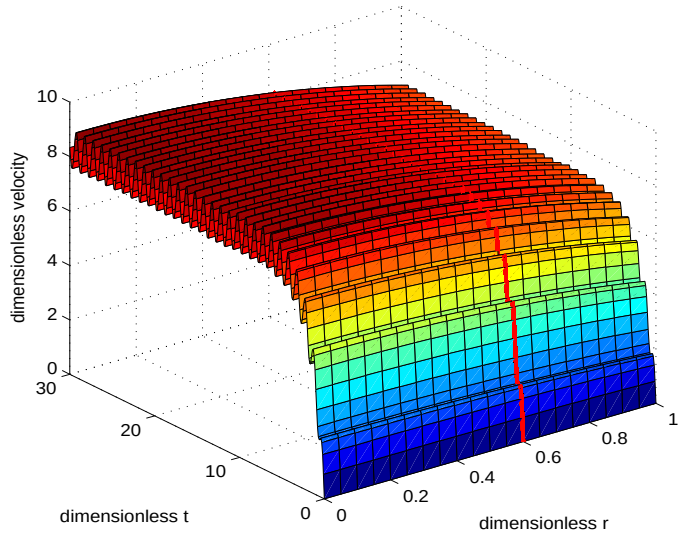

(b)

Figure 3.7: Velocity profiles in arteries with radius $r = 0.5$ cm for different slip parameter values (a) $l_b = 0$, (b) $l_b = 2$.

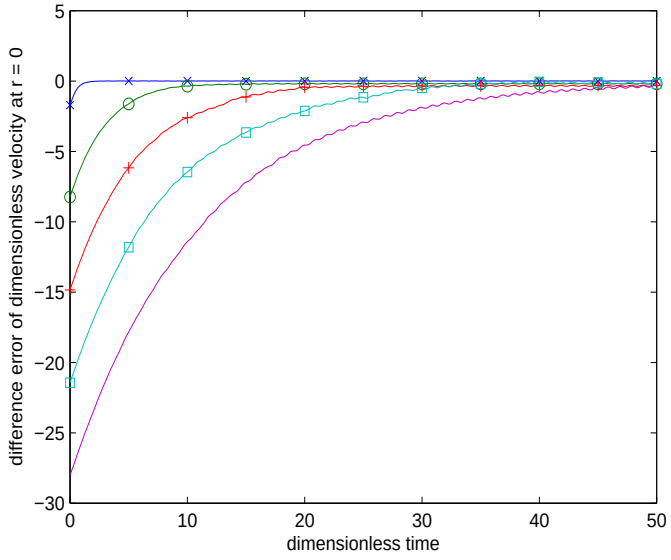

(a)

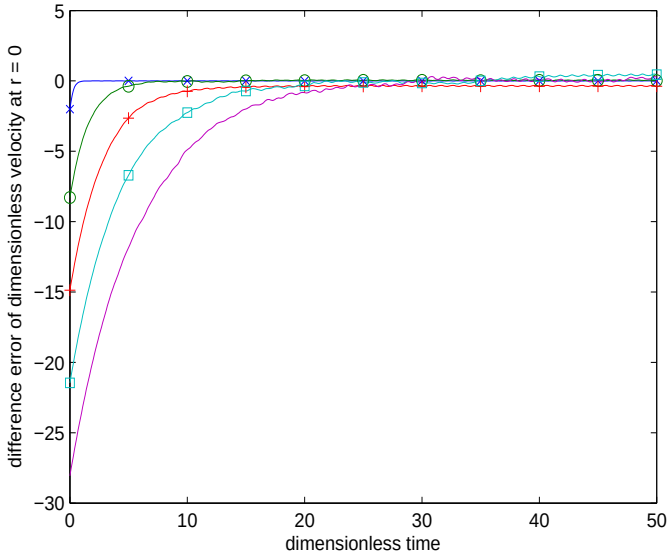

(b)

—×— $l_b = 0$; —○— $l_b = 2$; —+— $l_b = 4$;
—□— $l_b = 6$; ——— $l_b = 8$

Figure 3.8: Diagrams showing the convergence of numerical solutions for different slip parameters and artery radius: (a) $r = 0.15$ cm; (b) $r = 0.50$ cm.

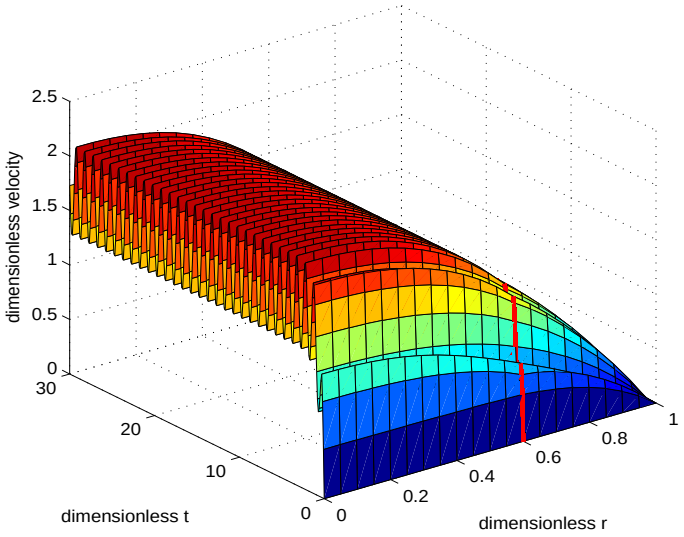

(a)

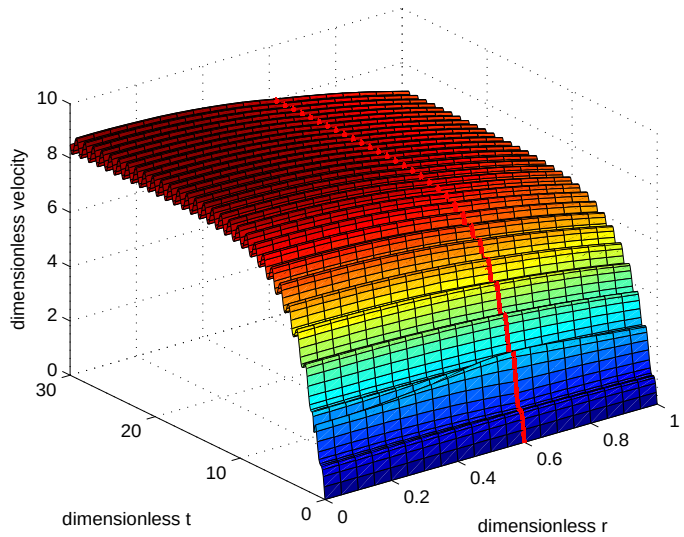

(b)

Figure 3.9: Velocity profiles in arteries with radius $r = 0.15$ cm for different slip parameter values (a) $l_b = 0$, (b) $l_b = 2$.

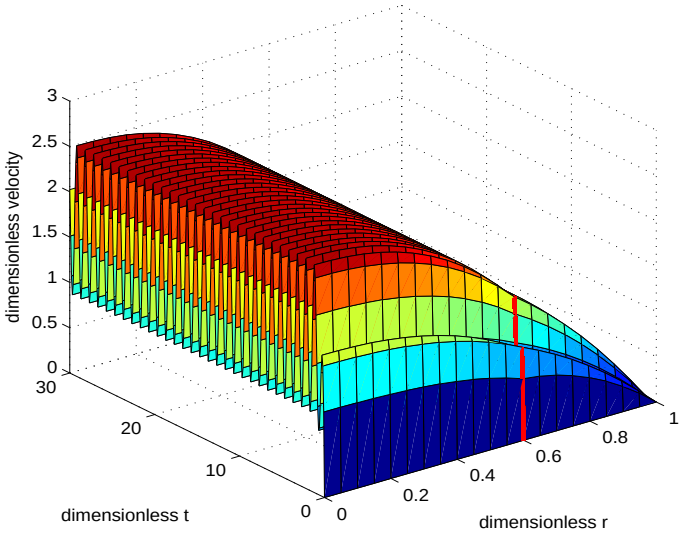

(a)

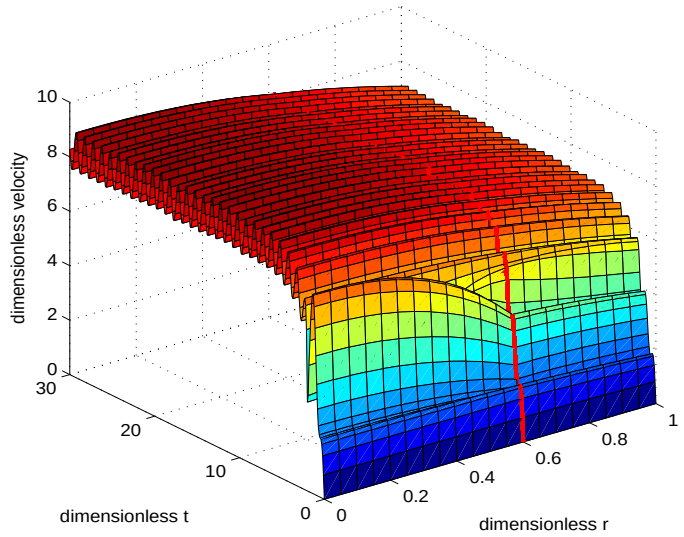

(b)

Figure 3.10: Velocity profiles in arteries with radius $r = 0.5$ cm for different slip parameter values (a) $l_b = 0$, (b) $l_b = 2$.

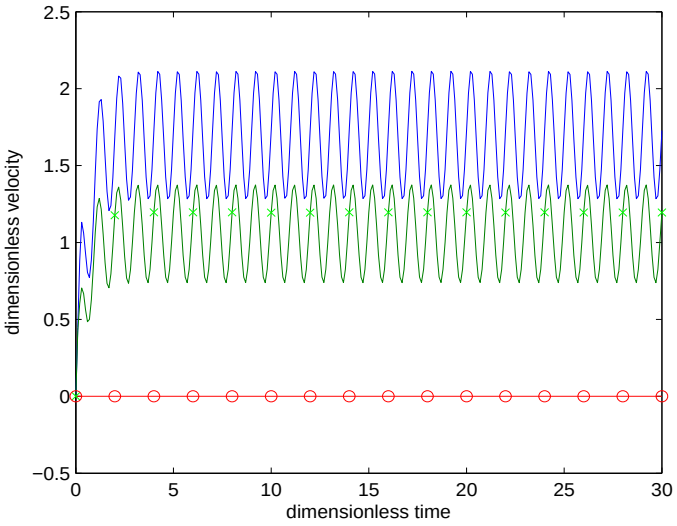

(a)

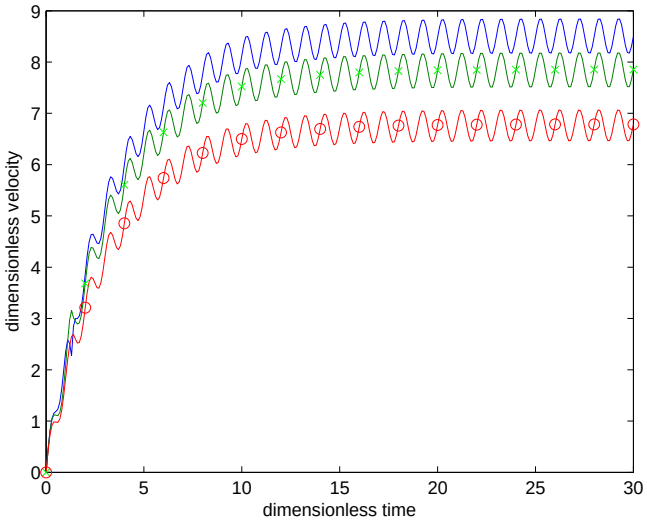

(b)

——— $r = 0$ (centre);
——+—— $r = 0.6$ (inner-outer layer interface);
——o—— $r = 1$ (wall)

Figure 3.11: Velocity profiles at three arterial locations (r_1, r_2, r_3) : for $m = -\frac{1}{4}$ and artery radius $r = 0.15$ cm for different slip parameter values (a) $l_b = 0$;(b) $l_b = 2$.

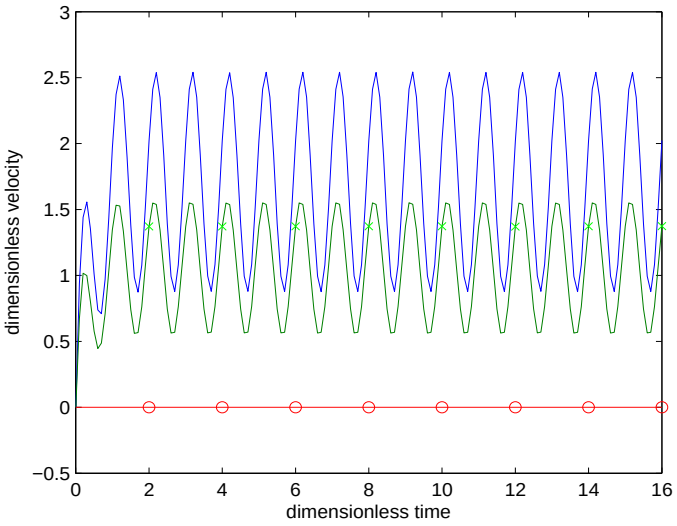

(a)

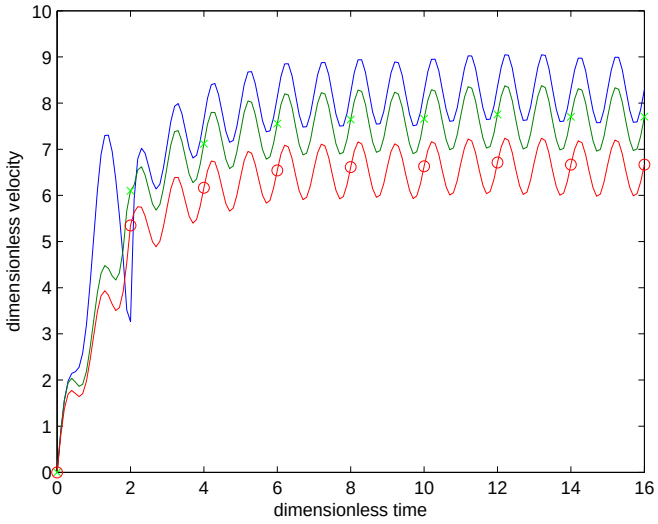

(b)

——— $r = 0$ (centre);
——+—— $r = 0.6$ (inner-outer layer interface);
——o—— $r = 1$ (wall)

Figure 3.12: Velocity profiles at three arterial locations (r_1, r_2, r_3) : for $m = -\frac{1}{4}$ and artery radius $r = 0.5$ cm for different slip parameter values (a) $l_b = 0$; (b) $l_b = 2$.

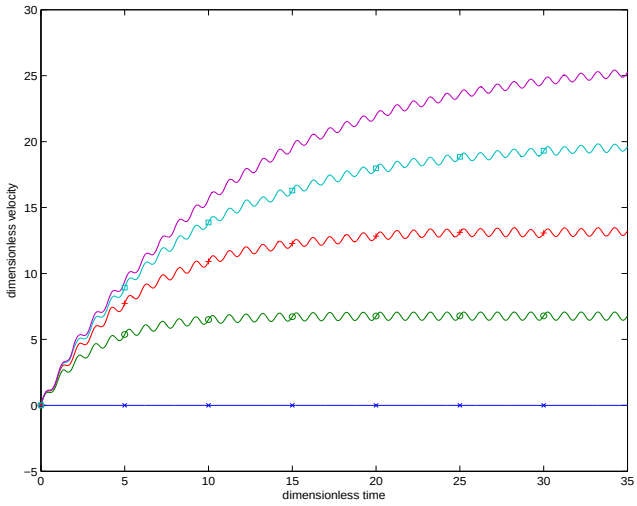

(a)

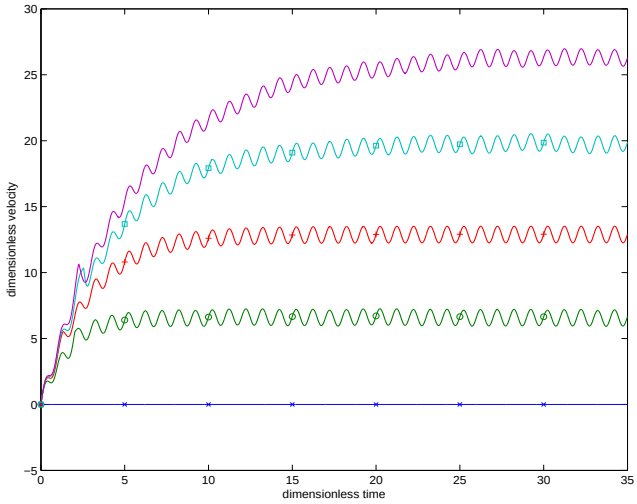

(b)

——×—— $l_b = 0$; ——○—— $l_b = 2$; ——+—— $l_b = 4$;
——□—— $l_b = 6$; ——— $l_b = 8$

Figure 3.13: Diagram showing the convergence of numerical results of the fluid velocity on the wall to the steady state pulsatile velocity field under various slip parameters l_b for two different artery radii : (a) $r = 0.15$ cm and (b) $r = 0.50$ cm.

3.5 Concluding Remarks

In this work, a mathematical model for the transient pulsatile flow of fluids through vessels, taking into account boundary slip and the Fahraeus-Lindquist effect, is established. For a special case of the underlying boundary value problem, an exact solution for the velocity field has been derived in explicit form, which provides one with an exact analytical method for investigating the flow phenomena under the special case, and also a mean for validating the subsequently developed numerical scheme for generating numerical results for the general case. Our analytical and numerical studies show that for the flow of fluids with the Fahraeus-Lindquist effect, boundary slip has very significant influence on the magnitude of the mean flow velocity and on the flow pattern and velocity profile on the cross-section. With boundary slip, the boundary layer near the wall also displays significant pulsatile flow nature. The results also show that as the boundary slip length increases, the convergence rate of numerical results to the exact solutions decreases and the time required to achieve the steady state pulsatile flow increases.

CHAPTER 4

The Effect of Boundary Slip on the Transient Pulsatile Flow in Three-Dimensional Computation Domains

4.1 General Overview

In order to have a better understanding of cardiovascular diseases particularly atherosclerosis, many researchers, especially in medical science, investigated the behaviour of blood flow in arteries in recent year. For a normal situation, blood flow in the circulatory system of the human is driven by the heart pumping. With the contracting and relaxing of the heart pumping, a pressure gradient throughout the arterial network is generated. The effect of body acceleration on the pulsatile blood flow through a rigid tube was studied by Chaturani and Palanisamy [118] assuming that the blood was a Newtonian fluid. Elsoud et al. [119] investigated the interaction between the peristaltic flow to pulsatile couple stress fluid. They examined a viscous incompressible couple stress fluid including a sinusoidal travelling wave on the infinite parallel walls. El-Shehawey et al. [120] studied the pulsatile blood flow under the periodic body acceleration in a porous medium. Then Das and Saha [121] investigated the arterial MHD pulsatile flow of blood under periodic body acceleration. Roa et al. [122] investigated the unsteady two-phase viscous ideal fluid flow through a parallel plate channel under a pulsatile pressure gradient subjected to a body acceleration.

Generally, the viscous fluids near walls is ideally assumed as no-slip. The disadvantage for using no-slip condition is evidently shown in polymer melts which often present the microscopic wall slip. The slip condition plays a significant role

when shear skin, spurt, and hysteresis effect is taken into account. Establishment of appropriate boundary conditions is essential to predict the fluid flows in many applications. The fluids in circular with boundary slip has a relevant technological applications, for instance, the fluid in polishing valves of artificial heart and internal cavities [123]. El-Shehaway et al. [124] studied the effect of the slip on the peristaltic flow of a non-Newtonian Maxwellian fluid. Eldesoky [125] investigated the influence of slip condition on peristaltic transport of a compressible Maxwell fluid through porous medium in a tube. Recently, the effect of slip boundary condition has been greatly investigated by many researchers [126–132].

In this work, the effect of boundary slip on unsteady pulsatile blood flow through two different tubes is investigated. The numerical approach is established based on the finite element method utilizing the Comsol Multiphysics. The rest of the chapter is organized as follows. Section 4.2 presents the governing field equations, followed by the boundary conditions in section 4.3. Section 4.4 gives the finite element formulation for the underlying boundary value problem. The domain of computation and numerical investigations are given in section 4.5 - 4.7, followed by concluding remarks in section 4.8

4.2 Governing Field Equations

In this study, the blood is assumed as an incompressible non-Newtonian fluid. The motion of blood flow can be described by the continuity equation (4.1) and the Navier-Stokes equations (4.2) as follows:

$$\nabla \cdot \mathbf{u} = 0, \tag{4.1}$$

$$\rho\big[\frac{\partial \mathbf{u}}{\partial t} + (\mathbf{u} \cdot \nabla)\mathbf{u}\big] = \nabla \cdot \sigma, \tag{4.2}$$

where $\mathbf{u} = (u_1, u_2, u_3)^T$ denotes the blood velocity vector, $\rho = 1.06 \quad g/cm^3$ denotes the blood density and σ is the total stress tensor which is related to the deformaion $\mathbf{D}$ by

$$\sigma = -p\mathbf{I} + 2\mu(\dot{\gamma})\mathbf{D} \tag{4.3}$$

where p is the blood pressure, $\mathbf{I}$ denotes a 3x3 identity matrix, μ is the blood viscosity, $\dot{\gamma}$ is the shear rate, and the rate of deformation tensor $\mathbf{D}$ is related to the velocity $\mathbf{u}$ by

$$\mathbf{D} = \frac{1}{2}(\nabla \mathbf{u} + \nabla \mathbf{u}^T). \tag{4.4}$$

For Carreau's shear-thinning model for non-Newtonian fluids, the viscosity is

Table 4.1: Parameter values for the model computation.

Parameter	Symbol	Value	Unit
Zero shear viscosity	μ_0	0.56	g cm^{-1} s^{-1}
Infinite shear viscosity	μ_∞	0.0345	g cm^{-1} s^{-1}
Time constant	λ	3.313	s
Consistency index	n	0.3568	-

assumed as a function of shear rate ($\dot{\gamma}$) as follows:

$$\mu(\dot{\gamma}) = \mu_\infty + (\mu_0 - \mu_\infty)[l + (\lambda\dot{\gamma})^2]^{\frac{(n-1)}{2}}, \tag{4.5}$$

where μ_0 is a zero shear viscosity, μ_∞ is a infinite shear viscosity, λ is a time constant, n is a consistency index, and the shear rate $\dot{\gamma}$ is given by

$$\dot{\gamma} = \sqrt{2tr[\frac{1}{2}(\nabla\mathbf{u} + \nabla\mathbf{u}^T)]^2}, \tag{4.6}$$

Moreover, the blood parameters are set as in Table 4.1: In indexing, the governing equations (4.1) - (4.4) can be written as

$$\frac{\partial u_j}{\partial x_j} = 0, \tag{4.7}$$

$$\rho\big(\frac{\partial u_i}{\partial t} + u_j\frac{\partial u_i}{\partial x_j}\big) = -\frac{\partial p}{\partial x_i} + \mu\big[\frac{\partial}{\partial x_j}\big(\frac{\partial u_i}{\partial x_j} + \frac{\partial u_j}{\partial x_i}\big)\big], \tag{4.8}$$

where the repeated literal index represents summation over the index range, and the single index is free index taking value over the index range.

4.3 Boundary Conditions

To compute the velocity field and pressure in the domain, the pulsatile pressure and the pulsatile flow rate need to be set. We model the pulsatile pressure and flow rate in terms of periodic functions $p(t) = p(t + kT)$ and $Q(t) = Q(t + kT)$ for $k = 1, 2, 3, ..$ with the cardiac period $T = 0.8s$, respectively. Furthermore, it is assumed that there is no difference in time variation in each cardiac cycle. According to the assumptions, the pulsatile pressure $p(t)$ and the flow rate $Q(t)$

Table 4.2: Coefficients of the pulsatile pressure function and the flow rate function obtained from interpolation of patients data.

mean parameters	k	α_k^p [torr]	β_k^p [torr]	α_k^Q [liter/min]	β_k^Q [liter/min]
$\overline{p} = 95.3333$ [torr]	1	5.9369	3.6334	0.0393	0.0241
	2	-11.1997	2.1255	-0.0360	0.0342
$\overline{Q} = 0.0896$ [litre/min]	3	-2.2778	-3.7528	-0.0131	0.0026
	4	2.7333	-0.6375	-0.0035	-0.0041

can be represented by cosine and sine functions as follows:

$$p(t) = \overline{p} + \sum_{k=1}^{4} \alpha_k^p \cos(k\omega t) + \beta_k^p \sin(k\omega t), \tag{4.9}$$

$$Q(t) = \overline{Q} + \sum_{k=1}^{4} \alpha_k^Q \cos(k\omega t) + \beta_k^Q \sin(k\omega t), \tag{4.10}$$

where $\overline{p}$ represents the mean pressure, $\overline{Q}$ is the mean flow rate, and $\omega = \frac{2\Pi}{T}$ is the angular frequency with period T.

By interpolating the set of pressure data taken from patients, the coefficient $\overline{p}$, $\overline{Q}$, α_k^p, β_k^p, α_k^Q, β_k^Q in Equations (4.9) and (4.10) can be evaluated as in Table 4.2

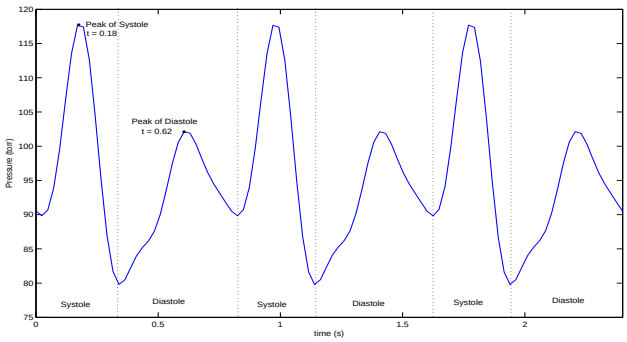

Figure 4.1: Pulsatile pressure function showing two peaks located at 0.18s and 0.62s of each cardiac cycle.

The normal inflow velocity at the inlet tube is set to pulsatile velocity corresponding to the flow rate and it can be expressed in term of the flow rate function as follows:

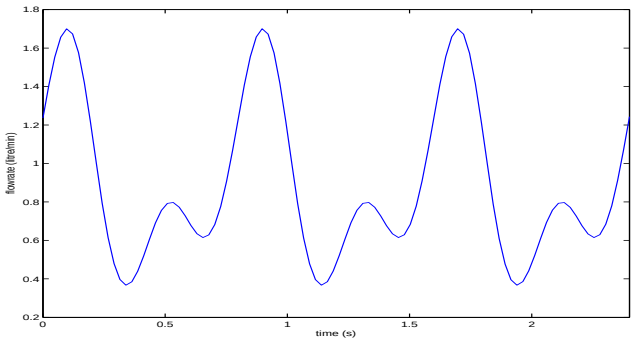

Figure 4.2: Pulsatile flow rate corresponding to the pulsatile pressure.

$$\mathbf{u}_{in}(t) = \frac{Q(t)}{A} \tag{4.11}$$

where $A = 28.28571\text{mm}^2$ is the cross-sectional area of the inlet boundary. On the outlet, pulsatile pressure condition is imposed with no viscous stress, namely

$$p = p_0(t), \quad \mu(\nabla \mathbf{u} + (\nabla \mathbf{u})^T) \cdot \mathbf{n} = 0, \tag{4.12}$$

where $\mathbf{n}$ is the unit normal vector at the boundary.

In this study, two different situations for the flow on artery wall are concerned, including the no-slip boundary condition

$$\mathbf{u_{wall}} = 0. \tag{4.13}$$

and the slip velocity condition

$$\mathbf{u_{wall}} = \frac{L_s}{\mu}\tau_{n,t}, \tag{4.14}$$

where $\tau_{n,t}$ is a tangential stress tensor on the wall, L_s is a slip length parameter. Note that when $L_s = 0$, we have $\mathbf{u_{wall}} = 0$ which corresponds to the no-slip boundary condition.

On summary, the model for the blood flow can be described by the following boundary value problem.
BVP: Find $\mathbf{u}$ and p such that equations (4.7), (4.8), and all boundary conditions are satisfied.

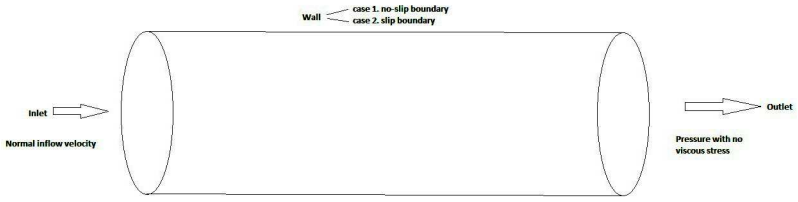

Figure 4.3: Circular tube with the imposed boundary conditions

4.4 Finite Element Formulation

In order to investigate the effect of boundary slip on the blood flow behaviour in three-dimensional models, the finite element approach is applied for numerical computation.

4.4.1 Weak Formulation under No-Slip Boundary Condition

To apply the finite element technique, the governing equations including its boundary conditions are transformed into the weak formulation. The system of equations (4.7) and (4.8) is multiplied by the weight function, then the variational statement corresponding to the boundary value problem is achieved.

Find u_i for $i = 1, 2, 3$ and $p \in H^1(\Omega)$ such that for all v_i for $i = 1, 2, 3$ and $v_p \in H_0^1(\Omega)$, all boundary conditions are satisfied and

$$\int_\Omega v_p \frac{\partial u_j}{\partial x_j} d\Omega = 0, \tag{4.15}$$

$$\rho \int_\Omega v_i \frac{\partial u_i}{\partial t} d\Omega + \rho \int_\Omega v_i (u_j \frac{\partial u_i}{\partial x_j}) d\Omega = -\int_\Omega v_i \frac{\partial p}{\partial x_i} d\Omega + \int_\Omega v_i \mu \frac{\partial}{\partial x_j} (\frac{\partial u_i}{\partial x_j} + \frac{\partial u_j}{\partial x_i}) d\Omega. \tag{4.16}$$

where
$H^1(\Omega) = \Big\{ v \in L^2(\Omega) | \frac{\partial v}{\partial x_i} \in L^2(\Omega)$ is the sobolev space $W^{1,2}(\Omega)\}$,
$H_0^1(\Omega) = \{v \in H^1(\Omega) | v = 0$ on the Dirichlet type boundary with $\| \cdot \|_{1,2,\Omega}\}$ and $L^2(\Omega)$ is the space of integrable function.

Using integration by part,

$$\int_\Omega \frac{\partial u}{\partial x_i} v d\Omega = \int_\Gamma u v \hat{n}_i d\Gamma - \int_\Omega u \frac{\partial v}{\partial x_i} d\Omega, \tag{4.17}$$

we get

$$\int_\Omega v_i \mu \frac{\partial}{\partial x_j}\left(\frac{\partial u_i}{\partial x_j}+\frac{\partial u_j}{\partial x_i}\right)d\Omega = \int_\Gamma v_i \mu\left(\frac{\partial u_i}{\partial x_j}+\frac{\partial u_j}{\partial x_i}\right)\hat{n}_i d\Gamma - \int_\Omega \mu \frac{\partial v_i}{\partial x_j}\left(\frac{\partial u_i}{\partial x_j}+\frac{\partial u_j}{\partial x_i}\right)d\Omega. \tag{4.18}$$

where $\hat{\mathbf{n}}$ is the outward unit surface normal to Γ, $\hat{n}_i$ is the i-th component of $\hat{\mathbf{n}}, i = 1, 2, 3$.

Therefore, equation (4.15) and (4.16) become

$$\int_\Omega v_p \frac{\partial u_j}{\partial x_j} = 0, \tag{4.19}$$

$$\begin{aligned}\rho\int_\Omega v_i\frac{\partial u_i}{\partial t}+\rho\int_\Omega v_i u_j\frac{\partial u_i}{\partial x_j}d\Omega = &-\Big[\int_\Gamma v_i p\hat{n}_i d\Gamma - \int_\Omega \frac{\partial v_i}{\partial x_i}p d\Omega\Big]\\ &+\Big[\int_\Gamma \mu v_i\Big(\frac{\partial u_i}{\partial x_j}+\frac{\partial u_j}{\partial x_i}\Big)\hat{n}_i d\Gamma\\ &-\int_\Omega \mu\frac{\partial v_i}{\partial x_i}\Big(\frac{\partial u_i}{\partial x_j}+\frac{\partial u_j}{\partial x_i}\Big)d\Omega\Big]\end{aligned} \tag{4.20}$$

where Γ is the boundary of the domain.

With the geometric tube domain, Γ can be decomposed into three parts, namely $\Gamma = \Gamma_{\text{wall}} \bigcup \Gamma_{\text{inlet}} \bigcup \Gamma_{\text{outlet}}$ where Γ_{wall} is the surface on the wall, Γ_{inlet} is the surface at the inlet, and Γ_{outlet} is the surface at the outlet.

Hence, the boundary integration in equation (4.20) can be decomposed into three integration terms, namely

$$\begin{aligned}\rho\int_\Omega v_i\frac{\partial u_i}{\partial t}+\rho\int_\Omega v_i u_j\frac{\partial u_i}{\partial x_j}d\Omega = &-\Big[\int_{\Gamma_{\text{wall}}} v_i p\hat{n}_i d\Gamma_{\text{wall}} + \int_{\Gamma_{\text{inlet}}} v_i p\hat{n}_i d\Gamma_{\text{inlet}}\\ &+\int_{\Gamma_{\text{outlet}}} v_i p\hat{n}_i d\Gamma_{\text{outlet}} - \int_\Omega \frac{\partial v_i}{\partial x_i}p d\Omega\Big]\\ &+\Big[\int_{\Gamma_{\text{wall}}} \mu v_i\Big(\frac{\partial u_i}{\partial x_j}+\frac{\partial u_j}{\partial x_i}\Big)\hat{n}_i d\Gamma_{\text{wall}}\\ &+\int_{\Gamma_{\text{inlet}}} \mu v_i\Big(\frac{\partial u_i}{\partial x_j}+\frac{\partial u_j}{\partial x_i}\Big)\hat{n}_i d\Gamma_{\text{inlet}}\\ &+\int_{\Gamma_{\text{outlet}}} \mu v_i\Big(\frac{\partial u_i}{\partial x_j}+\frac{\partial u_j}{\partial x_i}\Big)\hat{n}_i d\Gamma_{\text{outlet}}\\ &-\int_\Omega \mu\frac{\partial v_i}{\partial x_i}\Big(\frac{\partial u_i}{\partial x_j}+\frac{\partial u_j}{\partial x_i}\Big)d\Omega\Big]\end{aligned} \tag{4.21}$$

Since $v_i \in H_0^1$, the following terms are equal to be zero:

$$\begin{aligned}
\int_{\Gamma_{\text{wall}}} v_i p \hat{n}_i d\Gamma_{\text{wall}} &= 0, \\
\int_{\Gamma_{\text{inlet}}} v_i p \hat{n}_i d\Gamma_{\text{inlet}} &= 0, \\
\int_{\Gamma_{\text{wall}}} \mu v_i \big(\frac{\partial u_i}{\partial x_j} + \frac{\partial u_j}{\partial x_i}\big) \hat{n}_i d\Gamma_{\text{wall}} &= 0, \\
\int_{\Gamma_{\text{inlet}}} \mu v_i \big(\frac{\partial u_i}{\partial x_j} + \frac{\partial u_j}{\partial x_i}\big) \hat{n}_i d\Gamma_{\text{inlet}} &= 0, \\
\int_{\Gamma_{\text{outlet}}} \mu v_i \big(\frac{\partial u_i}{\partial x_j} + \frac{\partial u_j}{\partial x_i}\big) \hat{n}_i d\Gamma_{\text{outlet}} &= 0.
\end{aligned} \tag{4.22}$$

Thus, equation (4.21) can be reduced to,

$$\begin{aligned}
&\rho \int_\Omega v_i \frac{\partial u_i}{\partial t} + \rho \int_\Omega v_i u_j \frac{\partial u_i}{\partial x_j} d\Omega + \big[\int_{\Gamma_{\text{outlet}}} v_i p \hat{n}_i d\Gamma_{\text{outlet}} - \int_\Omega \frac{\partial v_i}{\partial x_i} p d\Omega \big] \\
&+ \int_\Omega \mu \frac{\partial v_i}{\partial x_i} \big(\frac{\partial u_i}{\partial x_j} + \frac{\partial u_j}{\partial x_i}\big) d\Omega = 0.
\end{aligned} \tag{4.23}$$

To apply the Galerkin Finite Element approximation, we assume that the K-dimensional subspace $H_K \in H^1(\Omega)$ has the basis functions $\{\phi_i\}_{i=1}^K$ for u_i and v_i, and the L-dimensional subspace $H_L \in H^1(\Omega)$ has the basis functions $\{\Phi_i\}_{i=1}^L$ for p and v_p. That is,

$$u_i(x,t) \approx (u_i)_K = \sum_{\alpha=1}^{K} \phi_\alpha(x) u_{i\alpha}(t), \tag{4.24}$$

$$v_i(x,t) \approx (v_i)_K = \sum_{\beta=1}^{K} \phi_\beta(x) v_{i\beta}(t), \tag{4.25}$$

$$p(x,t) \approx (p)_L = \sum_{\gamma=1}^{L} \Phi_\gamma(x) p_\gamma(t), \tag{4.26}$$

$$v_p(x,t) \approx (v_p)_L = \sum_{\epsilon=1}^{L} \Phi_\epsilon(x) v_p \epsilon(t). \tag{4.27}$$

Substituting the u_i, v_i, p and v_p in equations (4.24) - (4.27) into equations

(4.19) and (4.23) and noting that the values of v_i and v_p are arbitrary, we get

$$[(\Phi_\epsilon(x), \frac{\partial \phi_\alpha}{\partial x_i} u_{j\alpha})] = 0, \tag{4.28}$$

$$\begin{aligned}[\rho(\phi_\beta, \phi_\alpha)\dot{u}_{i\alpha}] + [\rho(\phi_\beta, u_j \frac{\partial \phi_\alpha}{\partial x_j})u_{i\alpha}] - [(\frac{\partial \phi_\beta}{\partial x_i}, \Phi_\gamma)p_\gamma] \\ +[(\frac{\partial \phi_\beta}{\partial x_j}, \mu\frac{\partial \phi_\alpha}{\partial x_j})u_{i\alpha}] + [(\frac{\partial \phi_\beta}{\partial x_j}, \mu\frac{\partial \phi_\alpha}{\partial x_i})u_{i\alpha}] + [(\phi_\beta, \Phi_\gamma)p_\gamma] = 0,\end{aligned} \tag{4.29}$$

where $(\cdot, \cdot)$ is the inner product given by $(u, v) = \int_\Omega u \cdot v d\Omega$, and $\dot{u}$ denotes $\frac{du}{dt}$.

The system of expanded equations (4.28) and (4.29) can be expressed as follows:

$$[(\Phi_\epsilon, \frac{\partial \phi_\alpha}{\partial x_1})u_{1\alpha} + (\Phi_\epsilon, \frac{\partial \phi_\alpha}{\partial x_2})u_{2\alpha} + (\Phi_\epsilon, \frac{\partial \phi_\alpha}{\partial x3})u_{3\alpha}] = 0, \tag{4.30}$$

$$\begin{aligned}[\rho(\phi_\beta, \phi_\alpha)\dot{u}_{i\alpha}] + [\rho(\phi_\beta, u_1\frac{\partial \phi_\alpha}{\partial x_1} + u_2\frac{\partial \phi_\alpha}{\partial x_2} + u_3\frac{\partial \phi_\alpha}{\partial x_3})u_{i\alpha}] \\ +[(\frac{\partial \phi_\beta}{\partial x_1}, \mu\frac{\partial \phi_\alpha}{\partial x_1})u_{i\alpha} + (\frac{\partial \phi_\beta}{\partial x_2}, \mu\frac{\partial \phi_\alpha}{\partial x_2})u_{i\alpha} + (\frac{\partial \phi_\beta}{\partial x_3}, \mu\frac{\partial \phi_\alpha}{\partial x_3}u_{i\alpha})] \\ +[(\frac{\partial \phi_\beta}{\partial x_1}, \mu\frac{\partial \phi_\alpha}{\partial x_i})u_{1\alpha} + (\frac{\partial \phi_\beta}{\partial x_2}, \mu\frac{\partial \phi_\alpha}{\partial x_i})u_{2\alpha} + (\frac{\partial \phi_\beta}{\partial x_3}, \mu\frac{\partial \phi_\alpha}{\partial x_i})u_{3\alpha}] \\ -[(\frac{\partial \phi_\beta}{\partial x_i}, \Phi_\gamma)p_\gamma] + [(\phi_\beta, \Phi_\gamma)p_\gamma] = 0,\end{aligned} \tag{4.31}$$

which can be written in matrix form

$$\mathbf{C^T U} = \mathbf{0}, \tag{4.32}$$

$$\mathbf{M\dot{U}} + (\mathbf{A(U)} + \mathbf{B})\mathbf{U} + \mathbf{DP} = \mathbf{0}. \tag{4.33}$$

where

$$\mathbf{U} = \begin{bmatrix} u_{1\alpha} \\ u_{2\alpha} \\ u_{3\alpha} \end{bmatrix}_{3K\times 1} \quad \text{with} \quad u_{i\alpha} = (u_{i1}, u_{i2}, .., u_{iK})^T,$$

$$\dot{\mathbf{U}} = \begin{bmatrix} \dot{u}_{1\alpha} \\ \dot{u}_{2\alpha} \\ \dot{u}_{3\alpha} \end{bmatrix}_{3K\times 1} \quad \text{with} \quad \dot{u}_{i\alpha} = (\dot{u}_{i1}, \dot{u}_{i2}, .., \dot{u}_{iK})^T,$$

$$\mathbf{P} = \Big[p_\gamma\Big]_{L\times 1} \quad \text{with} \quad p_\gamma = (p_1, p_2, .., p_L)^T.$$

The coefficient matrices and load vectors are

$$\mathbf{M} = \begin{bmatrix} m_{\beta\alpha} & 0 & 0 \\ 0 & m_{\beta\alpha} & 0 \\ 0 & 0 & m_{\beta\alpha} \end{bmatrix}_{3K\times 3K}$$

$$\mathbf{A}(\mathbf{U}) = \begin{bmatrix} a(u)_{\beta\alpha} & 0 & 0 \\ 0 & a(u)_{\beta\alpha} & 0 \\ 0 & 0 & a(u)_{\beta\alpha} \end{bmatrix}_{3K\times 3K}$$

$$\mathbf{B} = \begin{bmatrix} 2b_{11}+b_{22}+b_{33} & b_{12} & b_{13} \\ b_{21} & b_{11}+2b_{22}+b_{33} & b_{23} \\ b_{31} & b_{32} & b_{11}+b_{22}+2b_{33} \end{bmatrix}_{3K\times 3K}$$

$$\mathbf{C} = \begin{bmatrix} c^1_{\epsilon\alpha} \\ c^2_{\epsilon\alpha} \\ c^3_{\epsilon\alpha} \end{bmatrix}_{3K\times L}$$

$$\mathbf{D} = \begin{bmatrix} d^1_{\beta\gamma} \\ d^2_{\beta\gamma} \\ d^3_{\beta\gamma} \end{bmatrix}_{3K\times L}$$

where

$$\begin{aligned} m_{\beta\alpha} &= (\phi_\beta, \rho\phi_\alpha), \\ a(u)_{\beta\alpha} &= (\phi_\beta, \rho(u_1\frac{\partial\phi_\alpha}{\partial x_1} + u_2\frac{\partial\phi_\alpha}{\partial x_2} + u_3\frac{\partial\phi_\alpha}{\partial x_3})), \\ b_{mn} &= (b_{mn})_{\beta\alpha} = (\frac{\partial\phi_\beta}{\partial x_m}, \rho\frac{\partial\phi_\alpha}{\partial x_n}), \\ c^i_{\epsilon\alpha} &= (\Phi_\epsilon, \frac{\partial\phi_\alpha}{\partial x_i}), \\ d^i_{\beta\gamma} &= (\phi_\beta, \Phi_\gamma) - (\Phi_\gamma, \frac{\partial\phi_\beta}{\partial x_i}). \end{aligned}$$

4.4.2 Weak Formulation under Slip Boundary Condition

We now consider the second situation for the wall property, i.e. the slip boundary condition is applied to the artery wall. According to the slip boundary condition, $\mathbf{u_{wall}} = \frac{L_s}{\mu}\tau_{n,t}$, the following terms in equation (4.21) can be set to zero:

$$\begin{aligned}\int_{\Gamma_{\text{inlet}}} v_i p\hat{n}_i d\Gamma_{\text{inlet}} = 0,\\ \int_{\Gamma_{\text{inlet}}} \mu v_i\big(\frac{\partial u_i}{\partial x_j} + \frac{\partial u_j}{\partial x_i}\big)\hat{n}_i d\Gamma_{\text{inlet}} = 0,\\ \int_{\Gamma_{\text{outlet}}} \mu v_i\big(\frac{\partial u_i}{\partial x_j} + \frac{\partial u_j}{\partial x_i}\big)\hat{n}_i d\Gamma_{\text{outlet}} = 0,\end{aligned}$$

Thus, we have

$$\begin{aligned}&\rho\int_\Omega v_i\frac{\partial u_i}{\partial t} + \rho\int_\Omega v_i u_j\frac{\partial u_i}{\partial x_j}d\Omega + \big[\int_{\Gamma_{\text{wall}}} v_i p\hat{n}_i d\Gamma_{\text{wall}} + \int_{\Gamma_{\text{outlet}}} v_i p\hat{n}_i d\Gamma_{\text{outlet}}\\ &-\int_\Omega \frac{\partial v_i}{\partial x_i}pd\Omega\big] - \big[\int_{\Gamma_{\text{wall}}} \mu v_i\big(\frac{\partial u_i}{\partial x_j} + \frac{\partial u_j}{\partial x_i}\big)\hat{n}_i d\Gamma_{\text{wall}} - \int_\Omega \mu\frac{\partial v_i}{\partial x_i}\big(\frac{\partial u_i}{\partial x_j} + \frac{\partial u_j}{\partial x_i}\big)d\Omega\big] = 0.\end{aligned} \tag{4.34}$$

Since any vector $\mathbf{V} = (v_t, v_n) = (v_i t_i, v_i n_i)$, we have

$$(-p + \mu\big(\frac{\partial u_i}{\partial x_j} + \frac{\partial u_j}{\partial x_i}\big))n_j = \sigma_{ij}n_j = \chi_i \quad , \tag{4.35}$$

and consequently,

$$(-p + \mu\big(\frac{\partial u_i}{\partial x_j} + \frac{\partial u_j}{\partial x_i}\big))n_j = (\chi_{it}, \chi_{in}) = (\chi_i t_i, \chi_i n_i).$$

Hence,

$$\begin{aligned}-\int_{\Gamma_{\text{wall}}} v_i p\hat{n}_i d\Gamma_{\text{wall}} + \int_{\Gamma_{\text{wall}}} \mu v_i\big(\frac{\partial u_i}{\partial x_j} + \frac{\partial u_j}{\partial x_i}\big)\hat{n}_i d\Gamma_{\text{wall}} &= \int_{\Gamma_{\text{wall}}} (\chi_t v_t + \chi_n v_n)d\Gamma_{\text{wall}},\\ &= \int_{\Gamma_{\text{wall}}} \chi_t v_t d\Gamma_{\text{wall}},\\ &= \int_{\Gamma_{\text{wall}}} \frac{\mu}{L_s} v_t u_t d\Gamma_{\text{wall}}.\end{aligned} \tag{4.36}$$

Therefore, the system of equations (4.34) can be rewritten as,

$$\rho \int_\Omega v_i \frac{\partial u_i}{\partial t} + \rho \int_\Omega v_i u_j \frac{\partial u_i}{\partial x_j} d\Omega + \Big[\int_{\Gamma_{\text{outlet}}} v_i p \hat{n}_i d\Gamma_{\text{outlet}} - \int_\Omega \frac{\partial v_i}{\partial x_i} p d\Omega \Big] - \Big[\int_{\Gamma_{\text{wall}}} \frac{\mu}{L_s} v_t u_t d\Gamma_{\text{wall}} - \int_\Omega \mu \frac{\partial v_i}{\partial x_i} \big(\frac{\partial u_i}{\partial x_j} + \frac{\partial u_j}{\partial x_i} \big) d\Omega \Big] = 0. \quad (4.37)$$

To apply the Galerkin Finite Element approximation, we assume that the K-dimensional subspace $H_K \in H^1(\Omega)$ has the basis functions $\{\phi_i\}_{i=1}^K$ for u_i and v_i, and the L-dimensional subspace $H_L \in H^1(\Omega)$ has the basis functions $\{\Phi_i\}_{i=1}^L$ for p and v_p. That is,

$$u_i(x,t) \approx (u_i)_K = \sum_{\alpha=1}^K \phi_\alpha(x) u_{i\alpha}(t), \quad (4.38)$$

$$v_i(x,t) \approx (v_i)_K = \sum_{\beta=1}^K \phi_\beta(x) v_{i\beta}(t), \quad (4.39)$$

$$p(x,t) \approx (p)_L = \sum_{\gamma=1}^L \Phi_\gamma(x) p_\gamma(t), \quad (4.40)$$

$$v_p(x,t) \approx (v_p)_L = \sum_{\epsilon=1}^L \Phi_\epsilon(x) v_p \epsilon(t). \quad (4.41)$$

Substituting the u_i, v_i, p and v_p in equations (4.38) - (4.41) into equations (4.19) and (4.37) and then assuming the values of v_i and v_p to be arbitrary, we get

$$[(v_p \epsilon, \frac{\partial \phi_\alpha}{\partial x_i} u_{j\alpha})] = 0, \quad (4.42)$$

$$[\rho(\phi_\beta, \phi_\alpha)\dot{u}_{i\alpha}] + [\rho(\phi_\beta, u_j \frac{\partial \phi_\alpha}{\partial x_j}) u_{i\alpha}] - [(\frac{\partial \phi_\beta}{\partial x_i}, \Phi_\gamma) p_\gamma] + [(\frac{\partial \phi_\beta}{\partial x_j}, \mu \frac{\partial \phi_\alpha}{\partial x_j}) u_{i\alpha}] + [(\frac{\partial \phi_\beta}{\partial x_j}, \mu \frac{\partial \phi_\alpha}{\partial x_i}) u_{i\alpha}] + [(\phi_\beta, \Phi_\gamma) p_\gamma] - \frac{\mu}{L_s} [(\phi_\beta, \mu \phi_\alpha) u_{i\alpha}] = 0, \quad (4.43)$$

where $(\cdot, \cdot)$ is the inner product given by $(u, v) = \int_\Omega u \cdot v d\Omega$, and $\dot{u}$ denotes $\frac{du}{dt}$.

The system of expanded equations (4.42) and (4.43) can be expressed as fol-

lows:

$$[(\Phi_\epsilon, \frac{\partial \phi_\alpha}{\partial x_1})u_{1\alpha} + (\Phi_\epsilon, \frac{\partial \phi_\alpha}{\partial x_2})u_{2\alpha} + (\Phi_\epsilon, \frac{\partial \phi_\alpha}{\partial x3})u_{3\alpha}] = 0, \tag{4.44}$$

$$\begin{aligned}
&[\rho(\phi_\beta, \phi_\alpha)\dot{u}_{i\alpha}] + [\rho(\phi_\beta, u_1\frac{\partial \phi_\alpha}{\partial x_1} + u_2\frac{\partial \phi_\alpha}{\partial x_2} + u_3\frac{\partial \phi_\alpha}{\partial x_3})u_{i\alpha}] \\
&+[(\frac{\partial \phi_\beta}{\partial x_1}, \mu\frac{\partial \phi_\alpha}{\partial x_1})u_{i\alpha} + (\frac{\partial \phi_\beta}{\partial x_2}, \mu\frac{\partial \phi_\alpha}{\partial x_2})u_{i\alpha} + (\frac{\partial \phi_\beta}{\partial x_3}, \mu\frac{\partial \phi_\alpha}{\partial x_3}u_{i\alpha})] \\
&+[(\frac{\partial \phi_\beta}{\partial x_1}, \mu\frac{\partial \phi_\alpha}{\partial x_i})u_{1\alpha} + (\frac{\partial \phi_\beta}{\partial x_2}, \mu\frac{\partial \phi_\alpha}{\partial x_i})u_{2\alpha} + (\frac{\partial \phi_\beta}{\partial x_3}, \mu\frac{\partial \phi_\alpha}{\partial x_i})u_{3\alpha}] \\
&-[(\frac{\partial \phi_\beta}{\partial x_i}, \Phi_\gamma)p_\gamma] + [(\phi_\beta, \Phi_\gamma)p_\gamma] - \frac{\mu}{L_s}[(\phi_\beta, \mu\phi_\alpha)u_{i\alpha}] = 0,
\end{aligned} \tag{4.45}$$

which can be written in matrix form as

$$\mathbf{C^T U} = \mathbf{0}, \tag{4.46}$$

$$\mathbf{M\dot{U}} + (\mathbf{A(U)} + \mathbf{B})\mathbf{U} + \mathbf{DP} = \mathbf{0}, \tag{4.47}$$

where

$$\mathbf{U} = \begin{bmatrix} u_{1\alpha} \\ u_{2\alpha} \\ u_{3\alpha} \end{bmatrix}_{3K\times 1} \quad \text{with} \quad u_{i\alpha} = (u_{i1}, u_{i2}, .., u_{iK})^T \ ,$$

$$\mathbf{\dot{U}} = \begin{bmatrix} \dot{u}_{1\alpha} \\ \dot{u}_{2\alpha} \\ \dot{u}_{3\alpha} \end{bmatrix}_{3K\times 1} \quad \text{with} \quad \dot{u}_{i\alpha} = (\dot{u}_{i1}, \dot{u}_{i2}, .., \dot{u}_{iK})^T \ ,$$

$$\mathbf{P} = \begin{bmatrix} p_\gamma \end{bmatrix}_{L\times 1} \quad \text{with} \quad p_\gamma = (p_1, p_2, .., p_L)^T.$$

The coefficient matrices and load vectors can be read by

$$\mathbf{M} = \begin{bmatrix} m_{\beta\alpha} & 0 & 0 \\ 0 & m_{\beta\alpha} & 0 \\ 0 & 0 & m_{\beta\alpha} \end{bmatrix}_{3K\times 3K}$$

$$\mathbf{A}(\mathbf{U}) = \begin{bmatrix} a(u)_{\beta\alpha} & 0 & 0 \\ 0 & a(u)_{\beta\alpha} & 0 \\ 0 & 0 & a(u)_{\beta\alpha} \end{bmatrix}_{3K\times 3K}$$

$$\mathbf{B} = \begin{bmatrix} 2b_{11}+b_{22}+b_{33} & b_{12} & b_{13} \\ b_{21} & b_{11}+2b_{22}+b_{33} & b_{23} \\ b_{31} & b_{32} & b_{11}+b_{22}+2b_{33} \end{bmatrix}_{3K\times 3K}$$

$$\mathbf{C} = \begin{bmatrix} c^1_{\epsilon\alpha} \\ c^2_{\epsilon\alpha} \\ c^3_{\epsilon\alpha} \end{bmatrix}_{3K\times L}$$

$$\mathbf{D} = \begin{bmatrix} d^1_{\beta\gamma} \\ d^2_{\beta\gamma} \\ d^3_{\beta\gamma} \end{bmatrix}_{3K\times L}$$

where

$$\begin{aligned} m_{\beta\alpha} &= (\phi_\beta, \rho\phi_\alpha), \\ a(u)_{\beta\alpha} &= (\phi_\beta, \rho(u_1\frac{\partial\phi_\alpha}{\partial x_1} + u_2\frac{\partial\phi_\alpha}{\partial x_2} + u_3\frac{\partial\phi_\alpha}{\partial x_3})), \\ b_{mn} &= (b_{mn})_{\beta\alpha} = (\frac{\partial\phi_\beta}{\partial x_m}, \rho\frac{\partial\phi_\alpha}{\partial x_n}) - \frac{\mu}{L_s}(\phi_\beta, \mu\phi_\alpha), \\ c^i_{\epsilon\alpha} &= (\Phi_\epsilon, \frac{\partial\phi_\alpha}{\partial x_i}), \\ d^i_{\beta\gamma} &= (\phi_\beta, \Phi_\gamma) - (\Phi_\gamma, \frac{\partial\phi_\beta}{\partial x_i}). \end{aligned}$$

4.4.3 Isoparametric Mapping

The integrals in previous subsections are in terms of the (x, y, z) coordinate. To evaluate the integration of all the coefficient matrix and vectors over the non-uniform and distorted computation domain Ω directly is difficult because of the difference in the integration limits from element to element. Therefore, we apply the coordinate mapping method for handling the integration calculation. We then assume that there is an invertible transformation T_e between a standard element $\bar{\Omega}_e$ with a simple shape and an arbitrary element Ω_e. That is,

$$T_e(\xi, \zeta, \eta) = (x, y, z), \tag{4.48}$$

where T_e is an invertible mapping from the standard element $\bar{\Omega}_e$ in the system of (ξ, ζ, η) to an arbitrary element Ω_e in the system of (x, y, z). Hence, the inverse mapping of T_e can be defined as

$$T_e^{-1}(x, y, z) = (\xi, \zeta, \eta), \tag{4.49}$$

which maps from an arbitrary element Ω_e to the standard element $\bar{\Omega}_e$. Thus, every elements in the computation domain is the same in shape and calculation after transforming to a standard element $\bar{\Omega}_e$.

In our work, we have used the linear bar element, the two-dimensional quadrilateral element, the two-dimensional triangular element, the three-dimensional tetrahedral element, and the three-dimensional triangular prismatic element. The mapping between these standard elements in the parameter space (ξ, ζ, η) and the arbitrary elements in the (x, y, z) space are shown in Figure A.1-A.5 of Appendix A. Details of the coordinate transformation and element interpolation functions are given in Appendix A.

4.5 Domains of Computation and Cut-Line Location

To investigate the effect of boundary slip on the flow behaviour of blood in arteries, we construct two straight tube computation domains with a constant radius along the artery and a variable radius along the artery as shown in figure 4.4 (a)-(b), respectively. The length of both tubes is 11 cm, and the radius of the constant radius tube is 1.5 cm which is equal to the inlet radius of the variable radius tube whereas the outlet radius of the variable radius tube is 0.75 cm. Furthermore, to

observe the velocity, pressure, and shear rate behaviour, the cut-line is defined. Figure 4.5 (a)-(b) show the cut line located at the middle of the constant tube for the velocity measurement and the cut line near the wall along the tube length for pressure and shear rate measurement in the constant tube, respectively. Figure 4.6 (a)-(d) show the cut lines located near the inlet of the variable radius tube, at the middle of the variable radius tube, and near the outlet of the variable radius tube and the cut line near the wall along the tube length correspondingly.

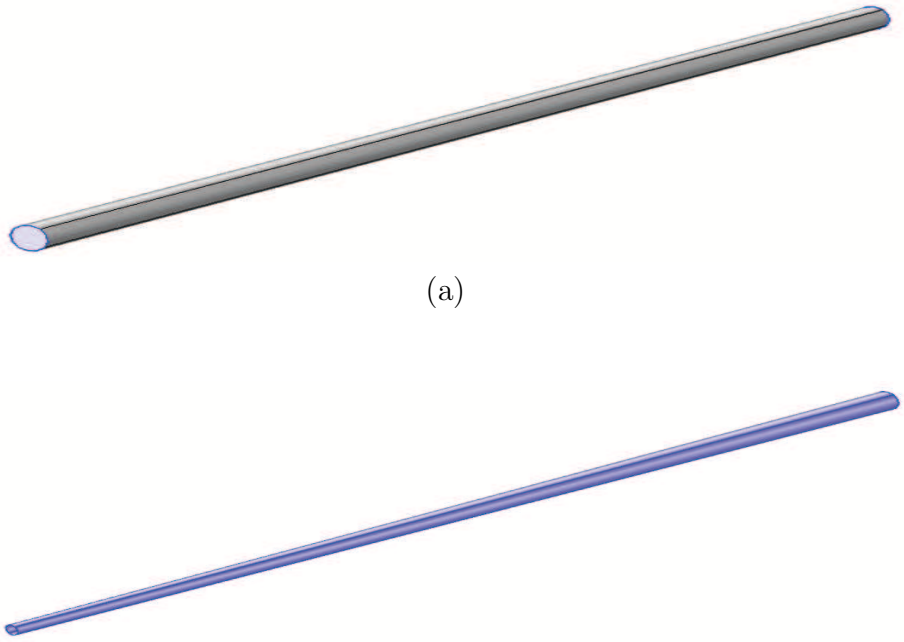

(a)

(b)

Figure 4.4: Diagram showing the computation domain of (a) the constant radius tube; (b) the variable radius tube

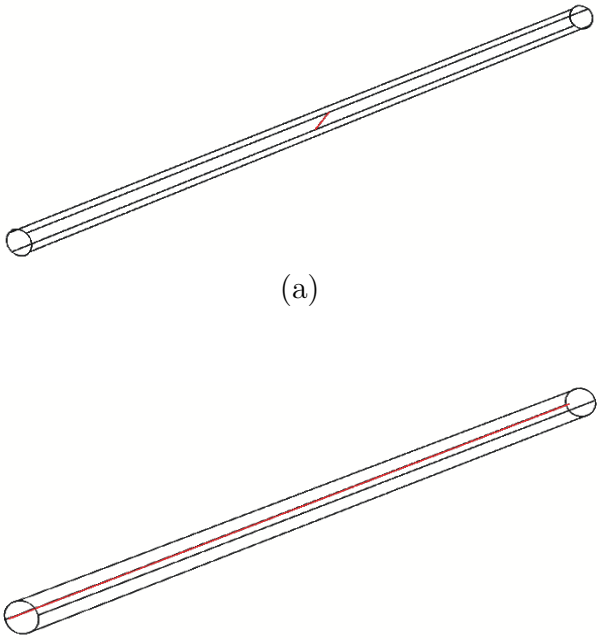

(a)

(b)

Figure 4.5: Diagram showing the cut line in the constant radius tube at (a) middle of the constant radius tube; (b) near the wall along the length of the constant radius tube.

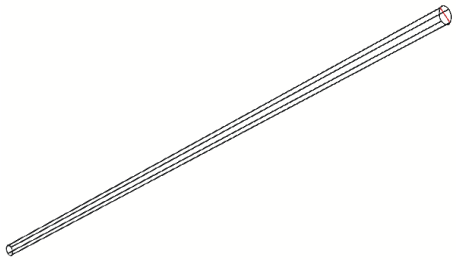

(a)

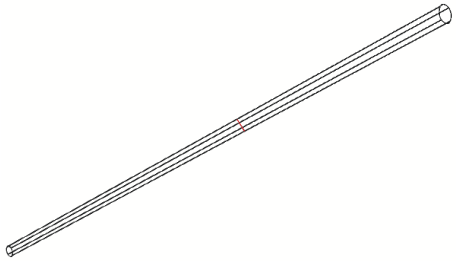

(b)

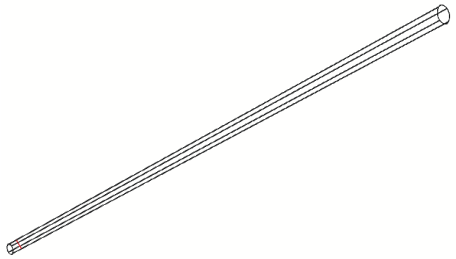

(c)

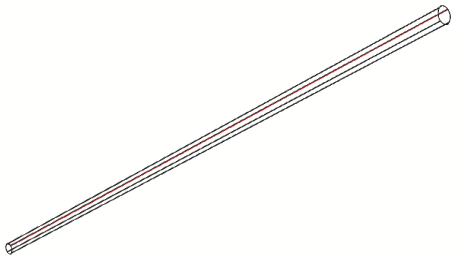

(d)

Figure 4.6: Diagram showing the cut line in the constant radius tube at (a) the inlet of the variable radius tube ; (b) the middle of the variable radius tube;(c) the outlet of the variable radius tube ; (d) near the wall along the length of the variable radius tube.

4.6 Mesh Sensitivity Analysis

In this section, the sensitivity of the numerical results to finite element meshes in the two computation domains are tested and analyzed for achieving reasonable numerical results . Four meshes with different number of elements are used and the corresponding numerical results obtained are then presented and discussed.

4.6.1 Mesh Quality

We firstly set four mesh qualities, namely, coarser, coarse, normal, and fine, in both of computation domains to analyze the effect of the finite element mesh on the numerical results for the no-slip wall. Figure 4.7 (a) shows the generated mesh on the artery computation domain with constant radius and Figure 4.8 (a) shows the generated mesh on the artery with variable radius along the wall, while Figure 4.7 (b) and 4.8 (b) show the close-up of the generated mesh element shape in the artery domain with constant radius and with variable radius along the tube, respectively. We see that the surface mesh elements compose of triangle elements and quadrilateral elements. According to these two elements shapes generation, it leads to the generation of the tetrahedral elements shape and the triangular prismatic elements shape in the domains of computation. Table 4.3 shows the number of mesh elements for coarser, coarse, normal, and fine mesh qualities in the computation domains.

(a)

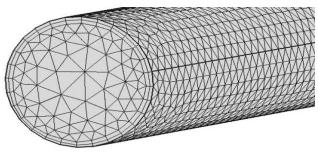

(b)

Figure 4.7: Diagram showing the mesh element of the constant radius tube.

(a)

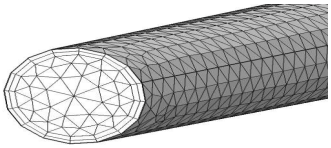

(b)

Figure 4.8: Diagram showing the mesh element of the variable radius tube.

Table 4.3: Number of mesh elements in four meshes, i.e coarser, coarse, normal, and fine mesh qualities.

Mesh Quality	Artery with Constant Radius	Artery with Variable Radius
	Number of Elements	Number of Elements
Coarser	56,878	41,733
Coarse	173,177	113,975
Normal	320,880	217,029
Fine	885,454	585,636

4.6.2 Mesh Sensitivity Results

Figure 4.9 shows the velocity profiles obtained by using four different meshing qualities in the artery domain with a constant radius, $r = 0.15$ cm, at two different instants of time (a) $t = 2.58$ s which is the time corresponding to the highest pressure for the systole period in the third cardiac cycle, and (b) $t = 3.02$ s which is the time corresponding to the highest pressure for the diastole period in the third cardiac cycle. The results have been detected by the cross-section diameter cut-line at the middle of the computation domain as demonstrated in Figure 4.5(a). We observe that when $t = 3.02$ s, all the numerical results from the four different meshing elements are almost identical. However, when $t = 2.58$ s, the results from the four meshing are significantly different, especially at the center of the artery, $r = 0$ or arclength $= 1.5$ cm. The fine meshing approximation gives the highest magnitude of the velocity with the most smooth velocity profile

curve. The normal meshing gives the second highest magnitude of velocity and the second smooth velocity profile whereas the coarser meshing produces the lowest magnitude of the piecewise continuous velocity approximation.

Figure 4.10 shows the velocity profiles from the four different meshing qualities at the inlet of the variable radius artery domain at two different instants of time (a) $t = 2.58$ s, and (b) $t = 3.08$ s. The results have been measured by the cross-section diameter cut-line at the inlet of the domain of computation as demonstrated in Figure 4.6(a). Since the cut-line is close to the inlet where the normal inflow velocity condition is applied, the four velocity profile curves in both graphs, $t = 2.58$ s and $t = 3.02$ s, are very close. Nevertheless, the velocity profiles are slightly different near the artery wall where the fine meshing element gives the most refine result and the second refine approximation is achieved by the normal meshing elements and the coarse meshing elements while the coarser meshing quality yields the coarsest approximation.

Figure 4.11 shows the graphs of velocity profiles obtained from the four different meshing qualities at the middle of the variable radius artery domain when (a) $t = 2.58$ s, and (b) $t = 3.02$ s, and Figure 4.12 shows velocity profile of the four different meshing qualities at the outlet of the radius variation artery domain when (a) $t = 2.58$ s, and (b) $t = 3.02$ s. The curves in Figure 4.11 and 4.12 are detected with a cross-section diameter cut-line at the middle of the variable radius artery domain as demonstrated in Figure 4.6(b) and a cross-section diameter cut-line at the outlet of the variable radius artery domain as demonstrated in Figure 4.6(c), respectively. According to the velocity profiles in Figure 4.11 and 4.12, it is obvious that the fine mesh yields the most smooth numerical results among the other meshing qualities and the normal meshing produces the second smooth numerical solution, while the coarsest piecewise velocity profile is produced by the coarser meshing elements. As we expect, the more elements we use, the smoother and more accurate the results will be. However, using the fine meshing for finite element computation leads to some disadvantage too. That is, the fine meshing scheme requires a large memory to store the large matrix and solve a large number of unknown variables leading to a huge amount of computation time, while the normal meshing quality yields a smaller matrix size and smaller amount of unknown variables leading to a greatly shorter time of computation with a slightly different numerical results. Through the sensitive investigation, the normal meshing scheme is chosen for our numerical investigation.

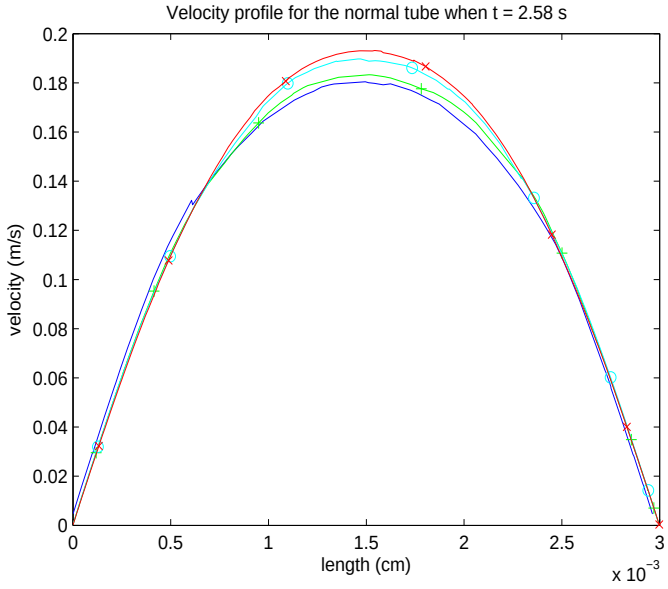

(a)

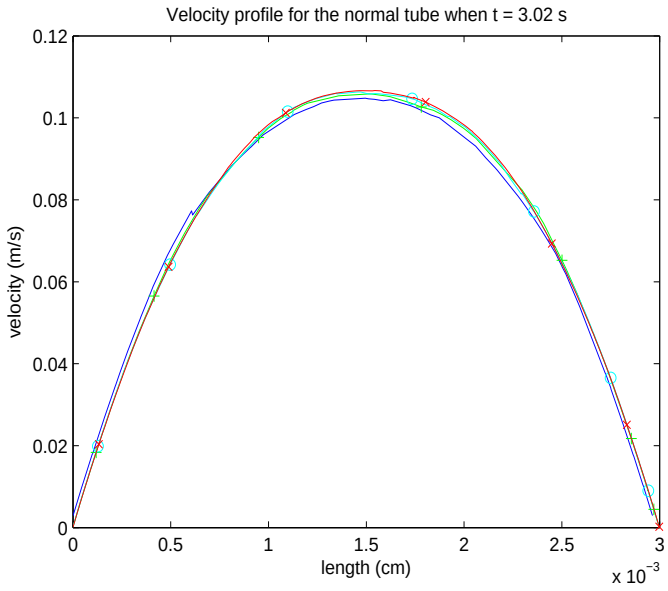

(b)

——— Coarser ; ——+—— Coarse
——o—— Normal ; ——x—— Fine

Figure 4.9: Velocity profile of the tube with radius 0.15 cm under slip parameter values $L_s = 0$ with various mesh qualities at two different times: (a) $t = 2.58s$ and (b) $t = 3.02s$.

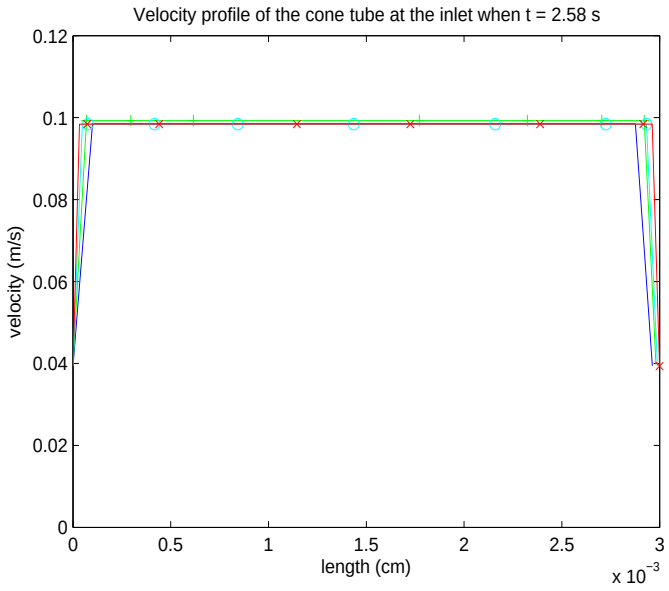

(a)

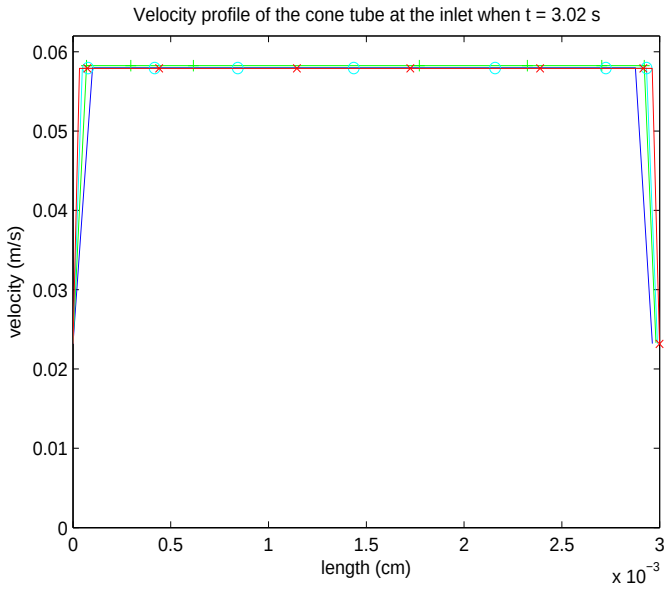

(b)

——— $L_s = 0$; ——+—— $L_s = Sl$;
——o—— $L_s = 2Sl$; ——x—— $L_s = 3Sl$

Figure 4.10: Velocity profile at the inlet of the cone-tube with radius 0.15 cm under slip parameter values $L_s = 0$ with various mesh qualities at two different times: (a) $t = 2.58s$ and (b) $t = 3.02s$.

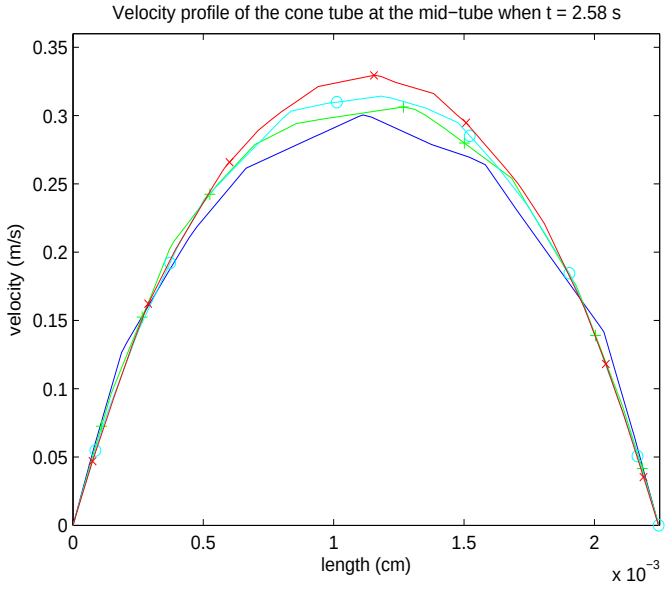

(a)

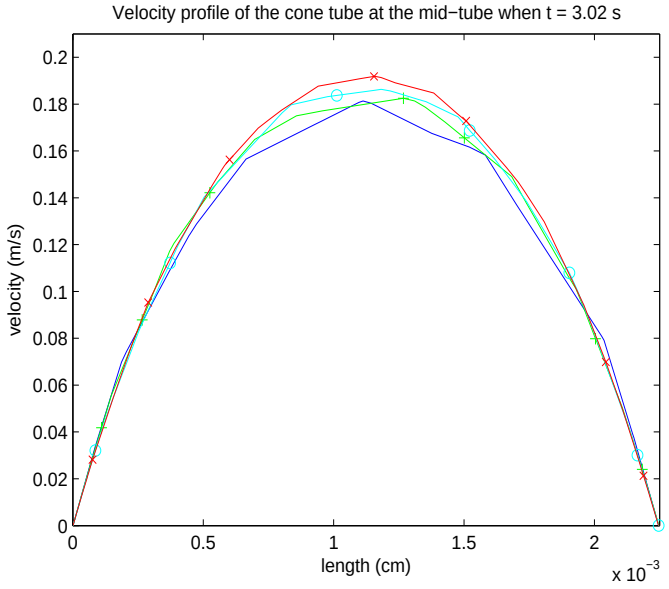

(b)

——— $L_s = 0$; ——+—— $L_s = Sl$;
——o—— $L_s = 2Sl$; ——x—— $L_s = 3Sl$

Figure 4.11: Velocity profile at the middle of the cone-tube with radius 0.1125 cm under slip parameter values $L_s = 0$ with various mesh qualities at two different times: (a) $t = 2.58s$ and (b) $t = 3.02s$.

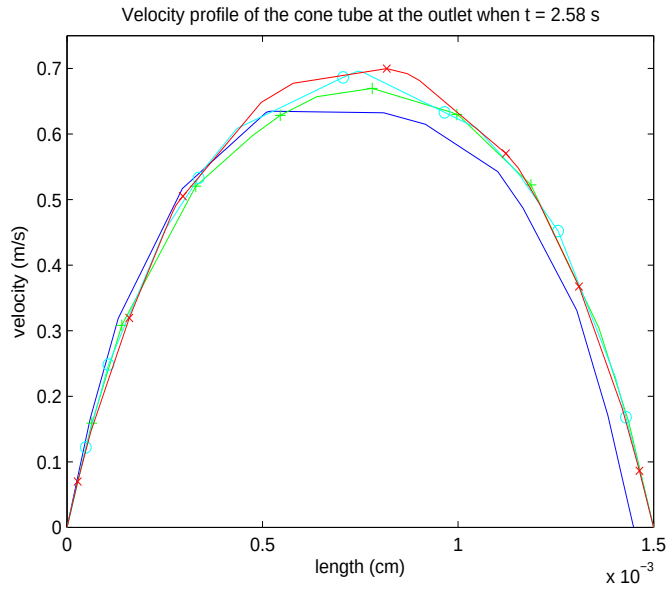

(a)

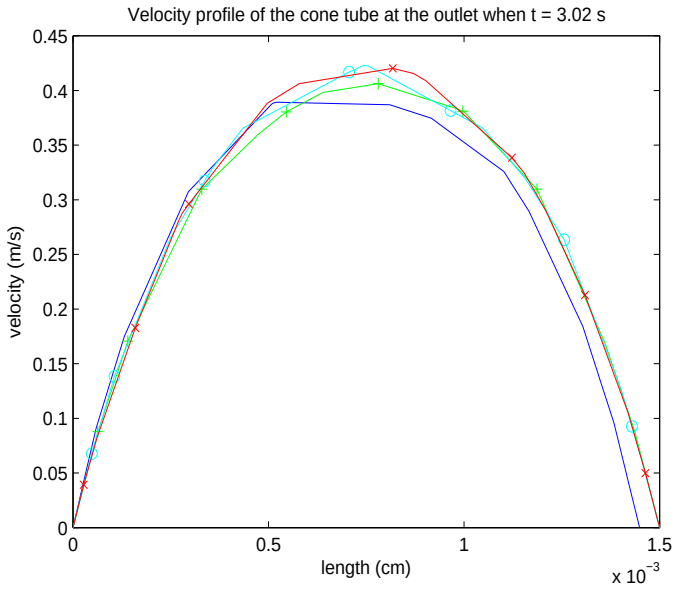

(b)

——— Coarse ; ——+—— Coarser
——o—— Normal ; ——x—— Fine

Figure 4.12: Velocity profile at the outlet of the cone-tube with radius 0.075 cm under slip parameter values $L_s = 0$ with various mesh qualities at two different times: (a) $t = 2.58s$ and (b) $t = 3.02$

4.7 Numerical Results

To study the effect of boundary slip on blood flow in the artery domains, we define the slip parameter L_s as the multiple of Sl given by

$$Sl = \begin{cases} \frac{U_{average}}{\dot{\gamma}_{avarage}} & \text{for the constant radius tube,} \\ \frac{r_{\text{inlet}}}{r}\frac{U_{average}}{\dot{\gamma}_{avarage}} & \text{for the variable radius tube,} \end{cases} \tag{4.50}$$

where r is the local radius, $U_{average} = \frac{U_{max}+U_{min}}{2}$, $U_{max} = 0.11789$ m/s, $U_{min} = 0.011789$ m/s, $\dot{\gamma}_{avarage} = 400$ 1/s, r_{inlet} denotes the radius at the inlet tube.

Thus, the slip parameter L_s is related to the average velocity $U_{average}$ and the average of shear rate $\dot{\gamma}_{avarage}$ in both cases.

4.7.1 The Constant Radius Artery

In this subsection, the effect of boundary slip on the constant radius artery domain is considered and discussed. Figure 4.13 shows the three-dimensional surface of velocity profile in the constant radius artery with respect to time detected by the cross-section diameter cut-line at the middle of the domain length with (a) no-slip boundary condition ($L_s = 0$) and (b) boundary slip condition ($L_s = 3SL$). Figure 4.14 shows the two-dimensional velocity profile for a constant radius artery with four different values of slip parameter, i.e $L_s = 0, SL, 2SL, 3SL$, at two different instants of time (a) $t = 2.58$ s and (b) $t = 3.02$ s. Clearly, the curve of $L_s = 0$ and $L_s = 3SL$ in Figure 4.14 is the cross-section from the three-dimensional velocity profile in Figure 4.13 when $t = 2.58$ s and $t = 3.02$ s, respectively. In Figure 4.14, we see that the velocity for no-slip boundary, $L_s = 0$, is zero on the artery wall while the velocity at the center, $r = 0$ at arclength = 1.5 cm, is about 0.19 m/s when $t = 2.58$ s, and 0.115 m/s when $t = 3.02$ s which is the highest velocity magnitude among the other slip parameter. When the slip parameter L_s increases, the velocity near the artery wall increases but the velocity magnitude at the center decreases. Figure 4.15 shows the velocity behaviour near the artery wall with a constant radius artery under four different slip parameters.

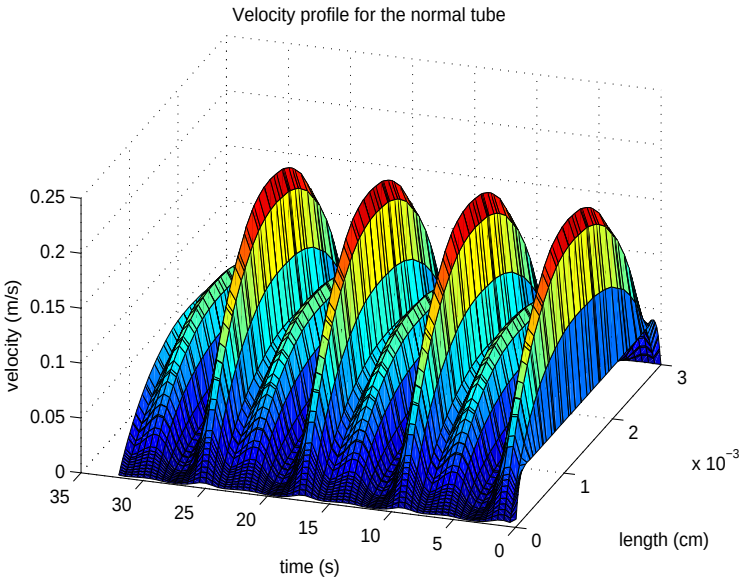

(a)

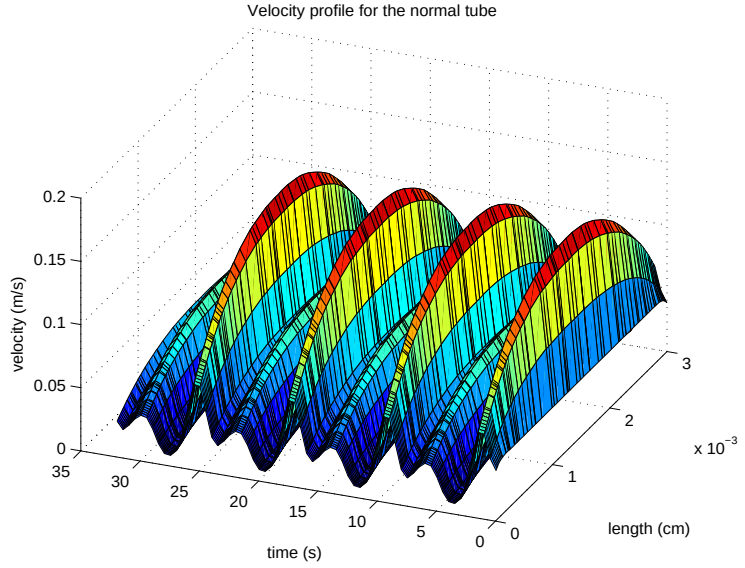

(b)

Figure 4.13: Variation of velocity as a function of time and space in the tube with radius 0.15 cm under two different slip parameter values (a) $L_s = 0$, (b) $L_s = 3Sl$.

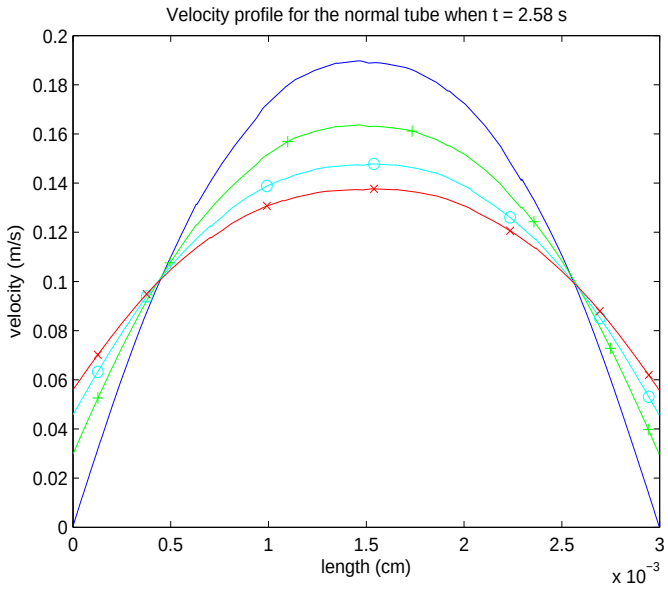

(a)

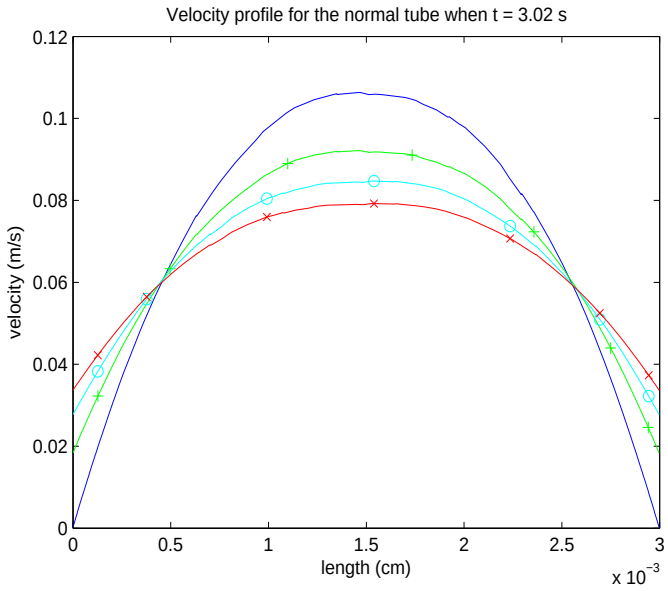

(b)

——— $L_s = 0$; ——+—— $L_s = Sl$;
——o—— $L_s = 2Sl$; ——x—— $L_s = 3Sl$

Figure 4.14: Velocity profile in the tube with radius 0.15 cm under different slip parameter values at two different instants of time (a) $t = 2.58$ s and (b) $t = 3.02$ s.

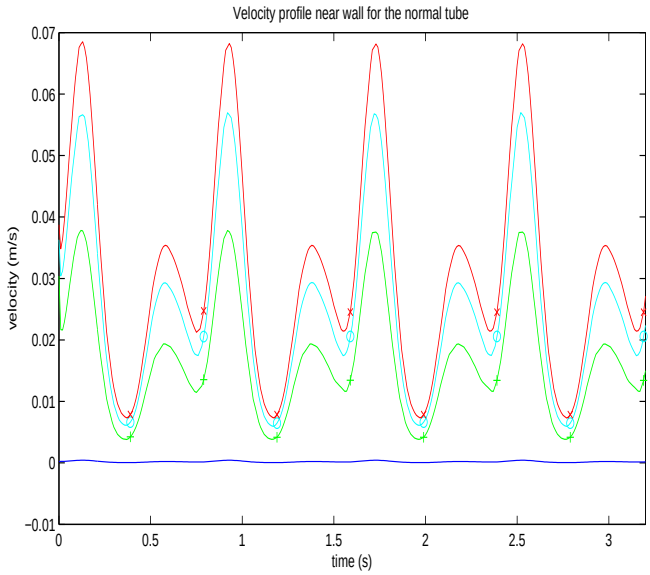

(a) ——— $L_s = 0$; ——+—— $L_s = Sl$;

——o—— $L_s = 2Sl$; ——x—— $L_s = 3Sl$

Figure 4.15: Velocity profile near the wall of the tube with radius 0.15 cm under different slip parameter values

It has been shown that the slip parameter not only causes a pulsatile pattern to the velocity at the artery wall but also increases the velocity magnitude near the artery wall, especially when it comes to the peak time of systole and diastole. The larger the slip parameter is, the larger the velocity magnitude is. Figure 4.16 demonstrates the pressure profile near the artery wall along the artery length with a constant radius, $r = 0.15$ cm, under four different slip parameter values at two different instants of times (a) $t = 2.58$ s, and (b) $t = 3.02$ s. We observe that the pressure increases linearly along the length of the artery wall for every slip parameter value. Moreover, in Figure 4.16(a), when the slip parameter increases for $t = 2.58$ s , not only the pressure value near the wall increases but also the steepness of the pressure slop increases. The difference in pressure for different slip parameter values at the inlet is dramatically less than the difference in pressure for different slip parameter values on the outlet. Nevertheless, in Figure 4.16(b), when the slip parameter increases for $t = 3.02$ s, even though the pressure value at the inlet increases, the steepness of pressure slop does not increase, i.e. the pressure slops for $L_s = 0$ and $L_s = 2Sl$ are steeper than the pressure slops for $L_s = Sl$ and $L_s = 3Sl$,respectively. It yields that the outlet pressure values for $L_s = Sl$ and $L_s = 3Sl$ are greater than the outlet pressure values for $L_s = 0$ and

$L_s = 2Sl$,respectively.

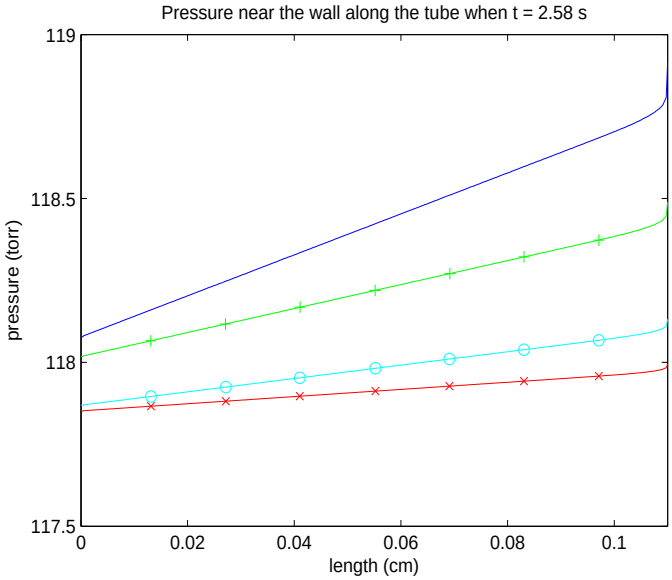

(a)

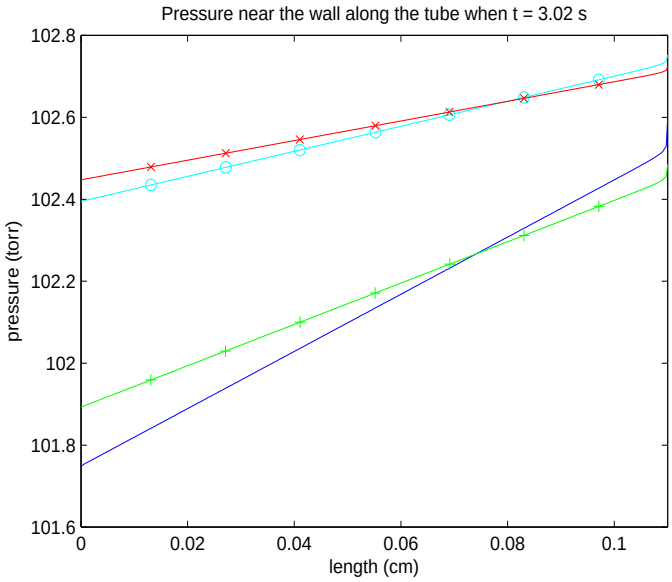

(b)

——— $L_s = 0$; ——+—— $L_s = Sl$;
——o—— $L_s = 2Sl$; ——x—— $L_s = 3Sl$

Figure 4.16: Pressure profile near the tube wall along its length with the tube radius 0.15 cm under different slip parameter values at two different instants of time (a) $t = 2.58s$ and (b) $t = 3.02$ s.

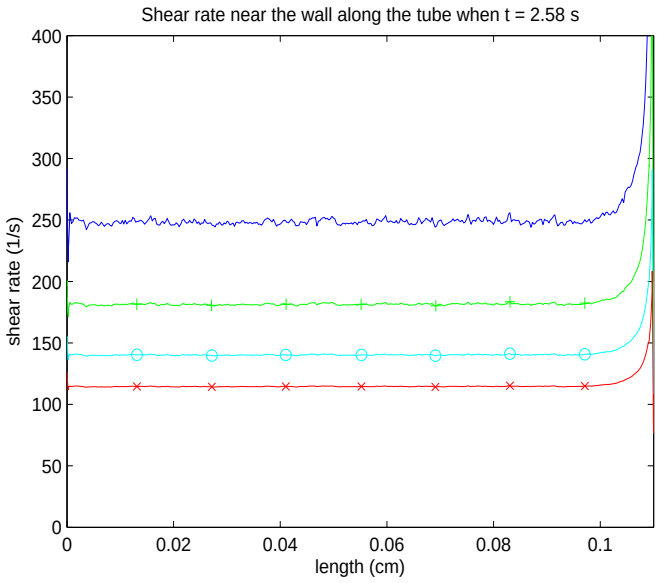

(a)

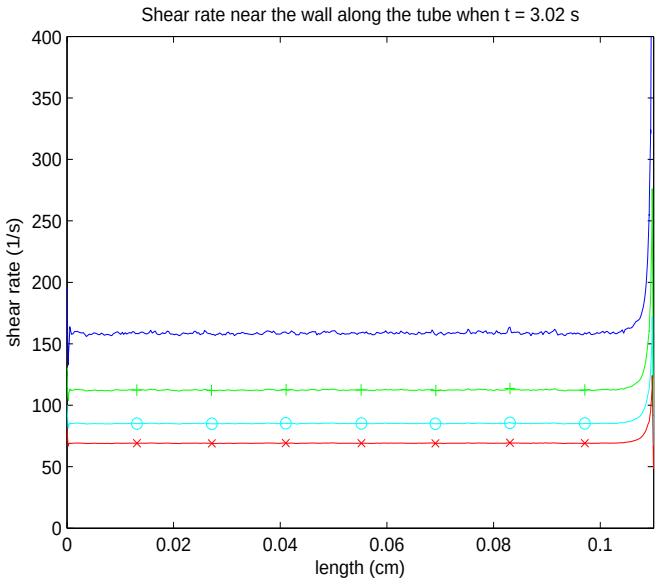

(b)

——— $L_s = 0$; ——+—— $L_s = Sl$;
——o—— $L_s = 2Sl$; ——x—— $L_s = 3Sl$

Figure 4.17: Shear rate profile near the tube wall along its length for the tube radius of 0.15 cm under different slip parameter values at two different instants of time (a) $t = 2.58s$ and (b) $t = 3.02$ s.

Figure 4.17 demonstrates the shear rate profile near the artery wall along

the artery length with a constant radius, $r = 0.15$ cm, under four different slip parameter values at $t = 2.58$ s, and $t = 3.02$ s. The results demonstrate that the shear rate values is influenced by the slip parameter values, i.e. when the slip parameter increases, the shear rate decreases. Noticeably, it is decreased by the number of multiple. Furthermore, the shear rate difference between the inlet and the outlet of the artery domain decreases as well. We also discover that the noise oscillation in the no-slip case is reduced.

4.7.2 The Effect of Variable Artery Radius

We now explore the blood flow behaviour in the variable radius artery domain taking into account the influence of boundary slip. Figure 4.18 demonstrates the three-dimensional surface of the variation of velocity as a function of time and space at the inlet of the variable radius artery domain under slip parameter values $L_s = 0$ (no-slip), and $L_s = 3Sl$ (boundary slip), Figure 4.19 demonstrates the two-dimensional velocity profile at the inlet of the variable radius artery domain under four different slip parameter values, $L_s = 0, Sl, 2Sl, 3Sl$, at $t = 2.58$ s, and $t = 3.02$ s. These numerical results have been evaluated via the cross-section diameter cut-line located near the inlet of the artery domain as presented in Figure 4.6(a). As a result of the cut-line located nearby the inlet where the normal inflow velocity condition is applied, the velocity profile curves are almost identically horizontal line at the same value. The velocity near the arterial wall is influenced by the boundary slip. We observe that when the boundary slip is applied, $L_s > 0$, the velocity near the arterial wall increases to the maximum magnitude of velocity as expressed in the velocity profile.

Figure 4.20 demonstrates the three-dimensional surface of the variation of velocity as a function of time and space at the middle of the variable radius artery domain with radius 0.1125 cm. under slip parameter values $L_s = 0$ (no-slip), and $L_s = 3Sl$ (boundary slip) whereas Figure 4.21 demonstrates the two-dimensional velocity profile at the middle of the variable radius artery domain under four different slip parameter values, i.e. $L_s = 0, Sl, 2Sl, 3Sl$, at $t = 2.58$ s, and $t = 3.02$ s. These numerical results have been detected by the cross-section diameter cut-line located at the middle of the artery domain as presented in Figure 4.6(b). From the graphs, we see that the boundary slip has significant effect on the velocity profile and its pattern. That is, when the slip parameter is applied, the velocity near the arterial wall at the middle of the domain increases gradually with respect to the slip parameter value. Contrarily, the maximum magnitude of the velocity located at the center of the cut-line (the center of

diameter) decreases when the slip parameter values increases. Consequently, the pattern of the velocity profile becomes flatter when the slip parameter value increases. Moreover, since the cross-section area at the middle is less than the cross-section area at the inlet, we have seen that the magnitude of velocity profile at the middle of the artery domain is greater than the magnitude of the velocity profile at the inlet.

Figure 4.22 demonstrates the three-dimensional surface of the variation of velocity as a function of time and space at the outlet of the radius variation artery domain with radius 0.075 cm under slip parameter values $L_s = 0$ (no-slip), and $L_s = 3Sl$ (boundary slip), Figure 4.23 demonstrates the two-dimensional velocity profile at the outlet of the radius variation artery domain under four different slip parameter values, i.e. $L_s = 0, Sl, 2Sl, 3Sl$, at $t = 2.58$ s, and $t = 3.02$ s. These numerical results have been evaluated via the cross-section diameter cut-line located near the outlet of the artery domain as presented in Figure 4.6(c). Similarly, the graphs show that the slip parameter influences the velocity profile and its pattern. When the slip parameter value increases, the near-wall velocity increases while the maximum magnitude of velocity decreases as the result of the flatter pattern. Since the outlet cross-section area is less than the cross-section area at the middle of the domain, the velocity magnitude is affected significantly by the boundary slip condition. Therefore, the larger the slip parameter value is and the less the area is, the larger the velocity magnitude near the arterial wall is and the flatter pattern of the velocity profile is.

Figure 4.24 shows the velocity magnitude near the arterial wall in the variable radius artery domain at two different locations, located near the inlet of the artery domain, at the middle of artery domain, near the outlet of the artery domain under four different slip parameter values, $L_s = 0, Sl, 2Sl, 3Sl$. We notice that the boundary slip influences the velocity profile, particularly, at peak of systole and diastole in each cardiac cycle. For the no-slip case, $L_s = 0$, the pulsatile flow nature gradually disappear toward the arterial wall; while with boundary slip, the flow near the arterial wall also displays a pulsatile nature. We then consider the pressure behaviour in the variable radius artery domain. Figure 4.25 demonstrates the pressure profile near the artery wall along the length of the variable radius artery domain under four different slip parameter values, $L_s = 0, Sl, 2Sl, 3Sl$, at $t = 2.58$ s, and $t = 3.02$ s. The graphs show that the pressure is a non-linear decreasing function along the domain length. It decreases significantly when the slip parameter increases. Since the pressure function is imposed on the outlet boundary, the pressure difference between the inlet and

the outlet of the artery domain is reduced when the boundary slip is considered. Hence, the pressure profile becomes flatter when the boundary slip is applied.

Ultimately, we investigate the shear rate behaviour. Figure 4.26 demonstrates the shear rate profile near the arterial wall along the length of the variable radius artery domain under four different slip parameter values, $L_s = 0, Sl, 2Sl, 3Sl$, at $t = 2.58$ s, and $t = 3.02$ s. Similarly, the graphs show that the shear rate is a nonlinear increasing function along the length and the shear rate near the outlet decreases dramatically when the slip parameter is applied.

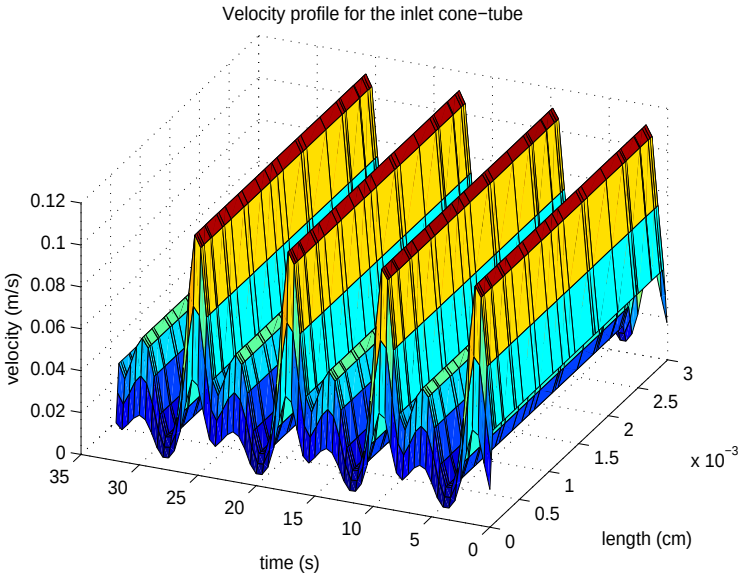

(a)

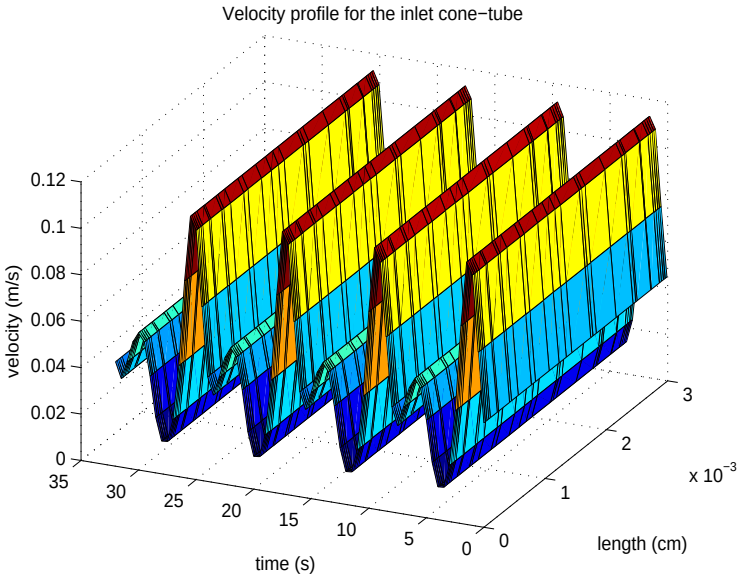

(b)

Figure 4.18: 3D graphs of the variation of velocity as a function of time and space in the cone-tube with inlet radius of 0.15 cm under slip parameter values (a) $L_s = 0$, (b) $L_s = 3Sl$.

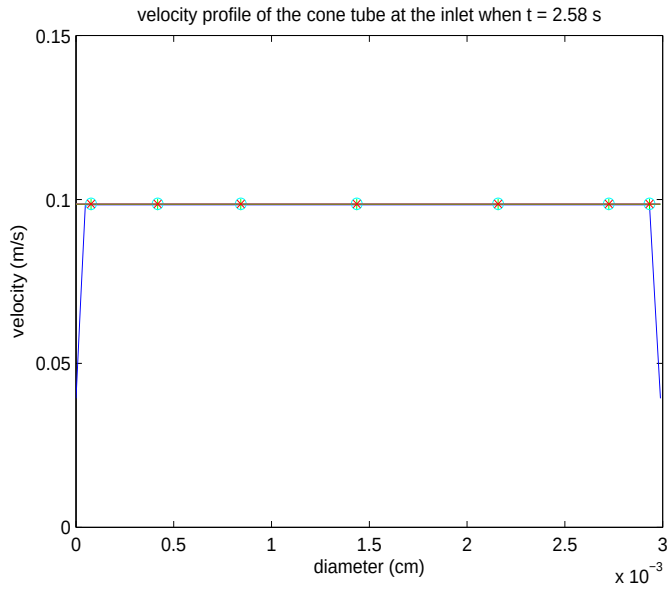

(a)

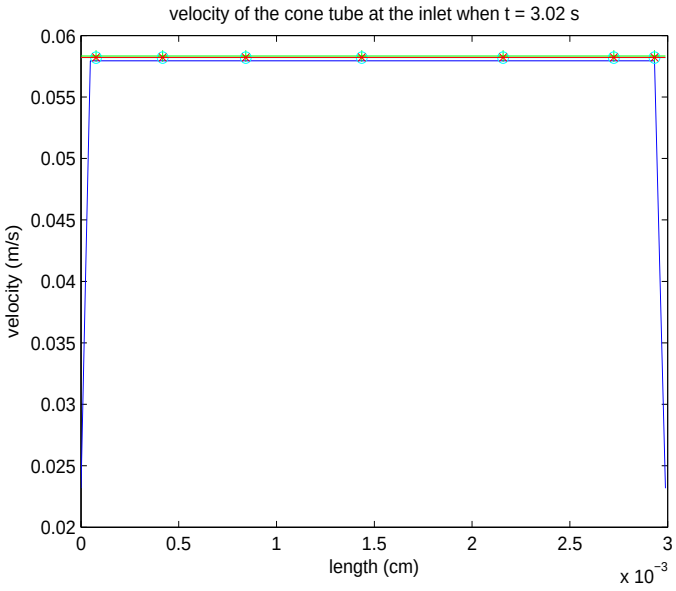

(b)

——— $L_s = 0$; ——+—— $L_s = Sl$;
——o—— $L_s = 2Sl$; ——x—— $L_s = 3Sl$

Figure 4.19: Velocity profile at the inlet of the cone-tube with radius 0.15 cm under different slip parameter values at two different times: (a) $t = 2.58$ s and (b) $t = 3.02$ s.

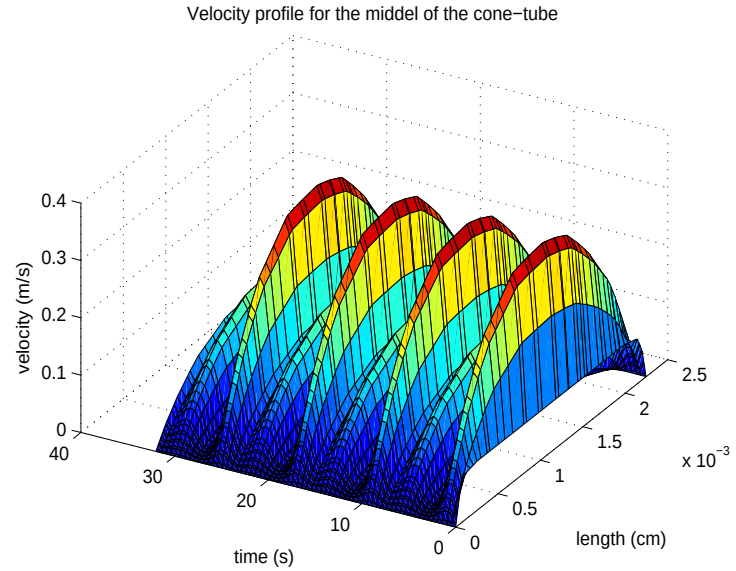

(a)

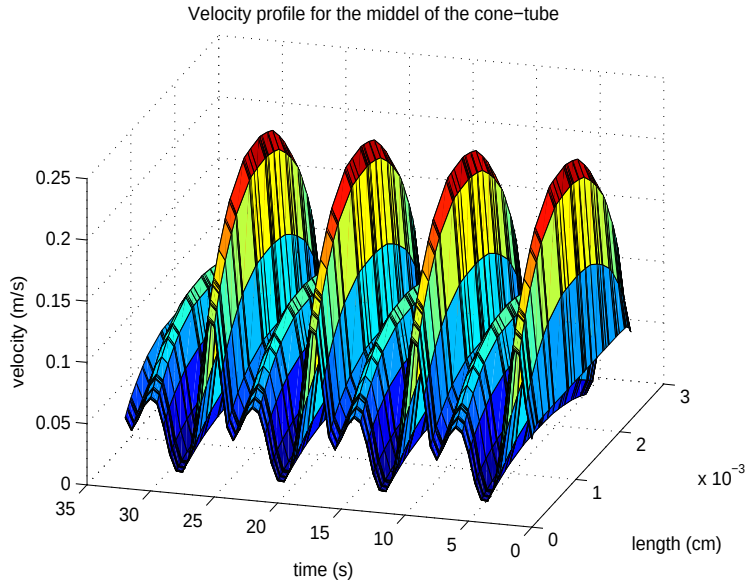

(b)

Figure 4.20: 3D graphs of the variation of velocity as a function of time and space in the cone-tube with middle radius 0.1125 cm under slip parameter values (a) $L_s = 0$, (b) $L_s = 3Sl$.

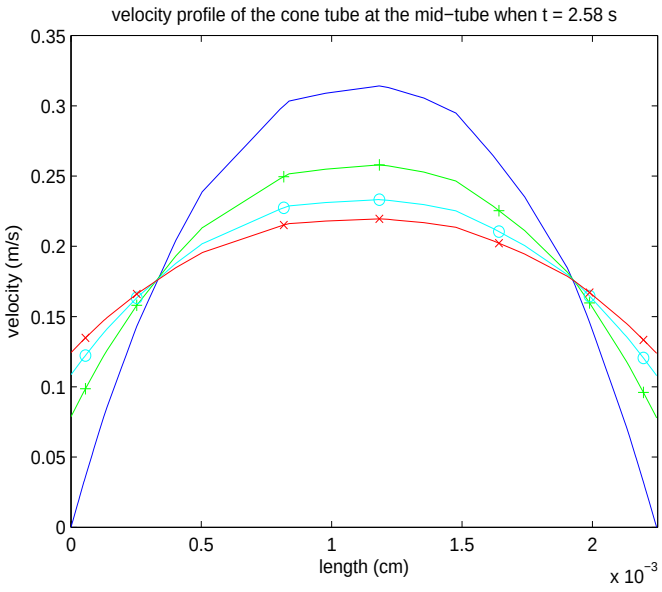

(a)

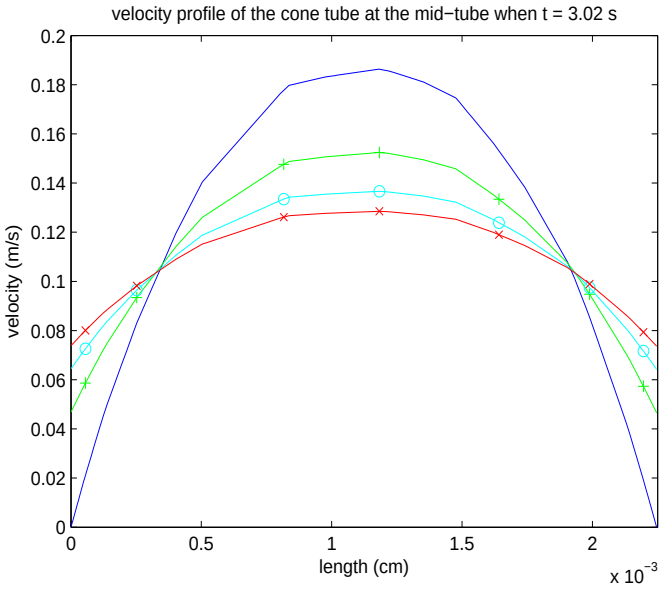

(b)

—— $L_s = 0$; —+— $L_s = Sl$;
—o— $L_s = 2Sl$; —x— $L_s = 3Sl$

Figure 4.21: Velocity profile at the middle of the cone-tube with radius 0.1125 cm under different slip parameter values at two different times: (a) $t = 2.58$ s and (b) $t = 3.02$ s.

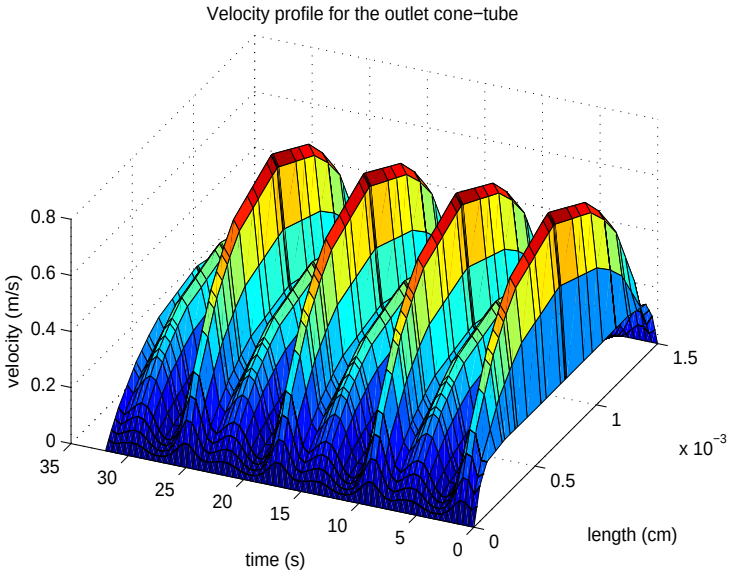

(a)

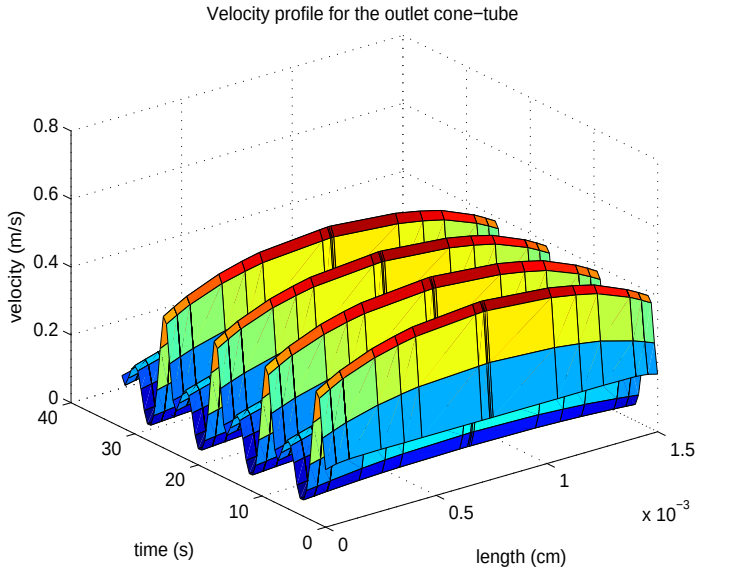

(b)

Figure 4.22: 3D graphs of the variation of velocity as a function of time and space in the cone-tube with middle radius 0.075 cm under slip parameter values (a) $L_s = 0$, (b) $L_s = 3Sl$.

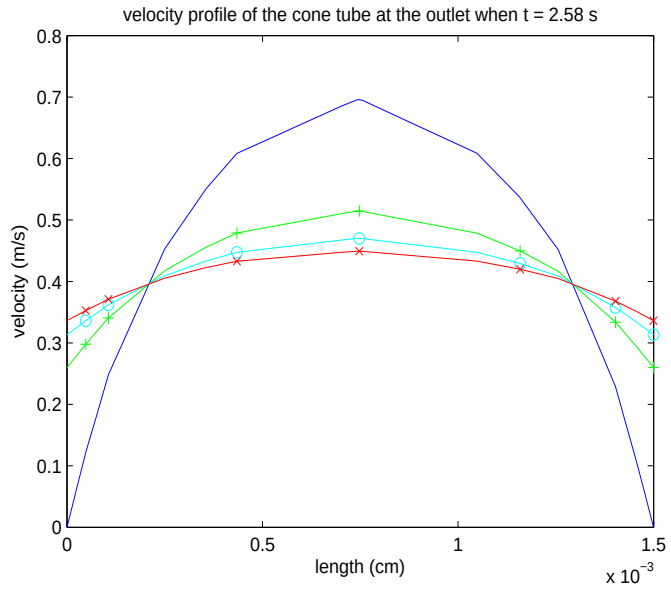

(a)

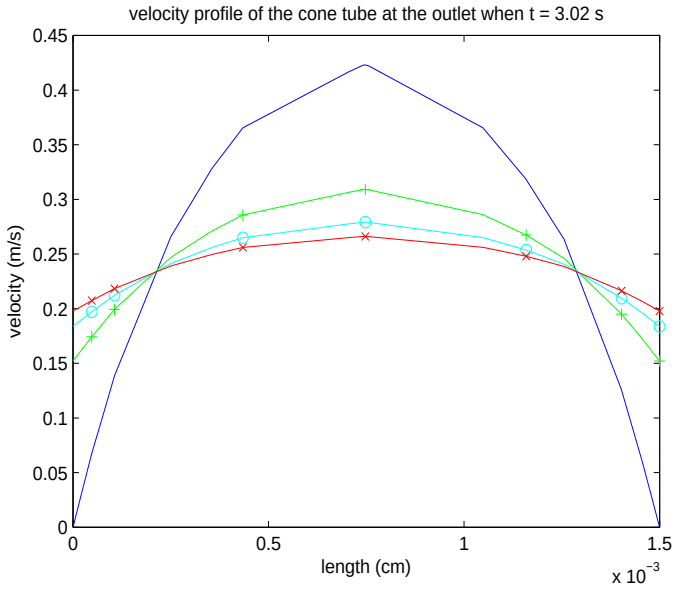

(b)

——— $L_s = 0$; ——+—— $L_s = Sl$;
——o—— $L_s = 2Sl$; ——x—— $L_s = 3Sl$

Figure 4.23: Velocity profile at the outlet of the cone-tube with radius of 0.075 cm under different slip parameter values at two different times: (a) $t = 2.58$ s and (b) $t = 3.02$ s.

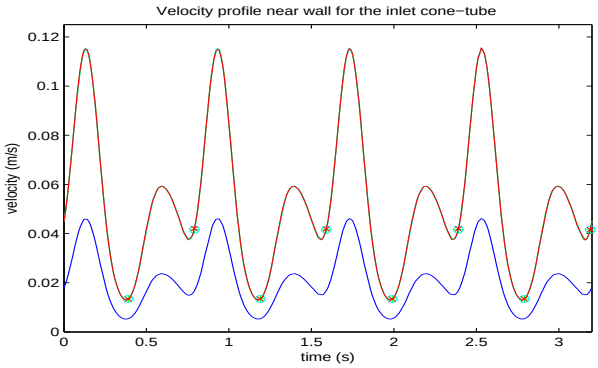

(a)

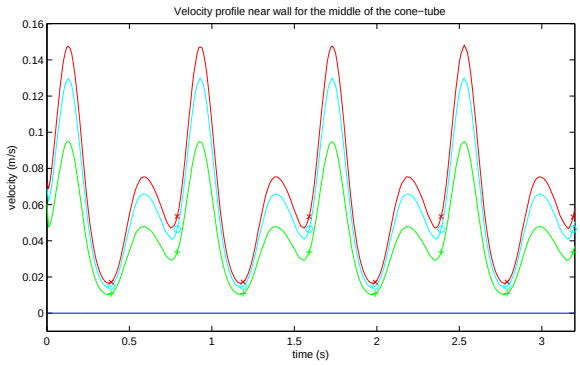

(b)

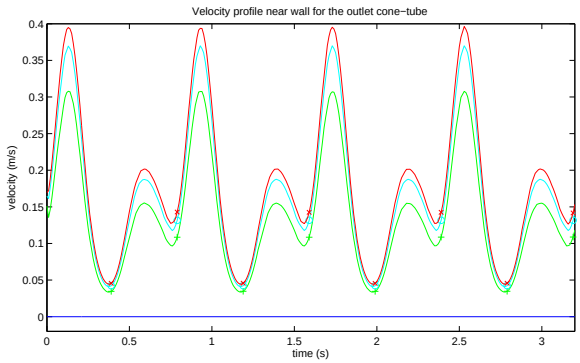

(c)

——— $L_s = 0$; ——+—— $L_s = Sl$;
——o—— $L_s = 2Sl$; ——x—— $L_s = 3Sl$

Figure 4.24: Velocity profile near the wall under different slip parameter values at three locations: (a) the inlet of the cone-tube with radius 0.15 cm. ; (b) the middle of the cone-tube with radius 0.1125 cm. ; (c) the outlet of the cone-tube with radius 0.075 cm.

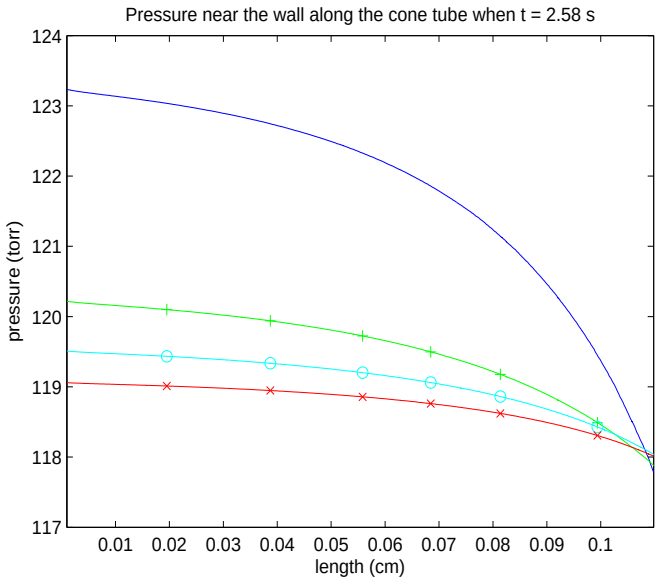

(a)

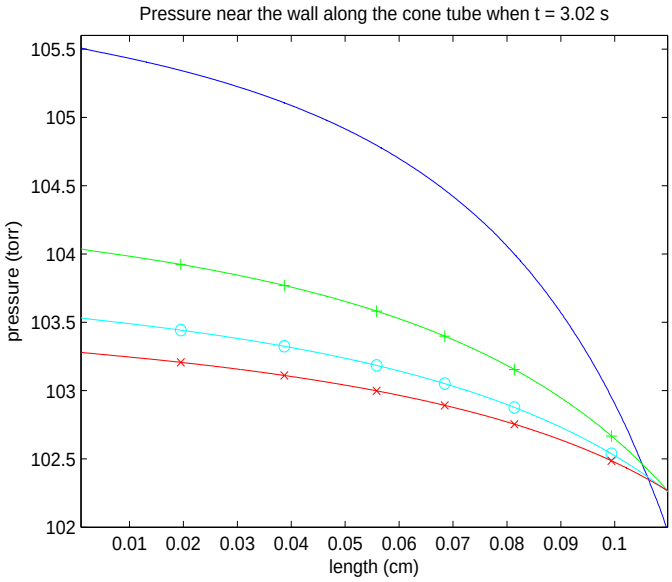

(b)

——— $L_s = 0$; ——+—— $L_s = Sl$;
——o—— $L_s = 2Sl$; ——x—— $L_s = 3Sl$

Figure 4.25: In the figure, the graphs show the pressure profile near the wall of the cone-tube along its length for the tube radius 0.15 cm under different slip parameter values at two different times: (a) $t = 2.58s$ and (b) $t = 3.02s$.

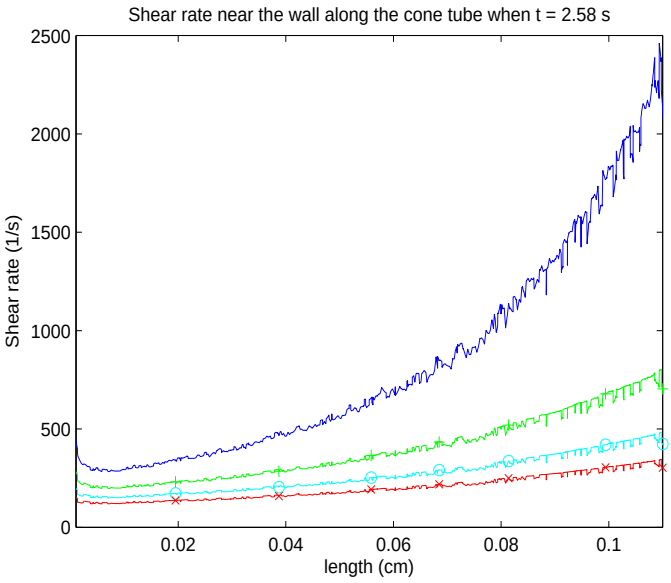

(a)

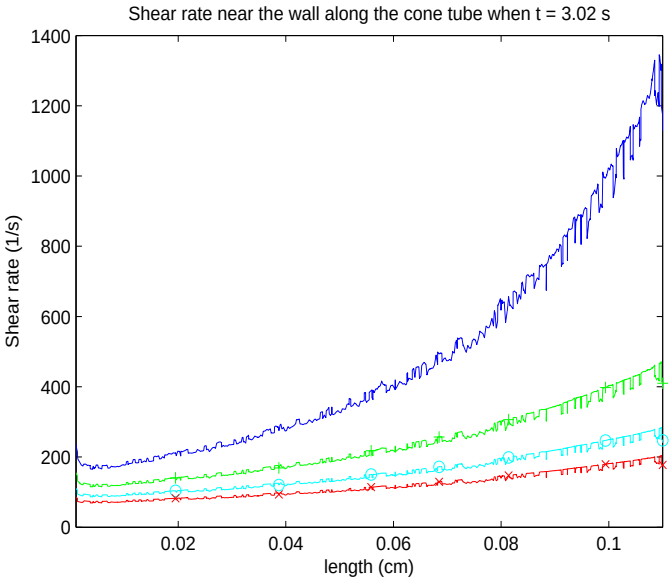

(b)

——— $L_s = 0$; ——+—— $L_s = Sl$;
——o—— $L_s = 2Sl$; ——x—— $L_s = 3Sl$

Figure 4.26: Shear rate profile near the wall of the cone-tube along its length with the tube radius 0.15 cm under different slip parameter values at two different times: (a) $t = 2.58s$ and (b) $t = 3.02s$.

4.8 Concluding Remarks

In this chapter, the numerical solution for the three-dimensional transient pulsatile blood flow model of an incompressible non-Newtonian fluid in artery is studied taking into account the boundary slip in two types of artery domains, i.e. the artery domain with a constant radius and the artery domain with a variable radius along the length. A numerical scheme based on the finite element method utilizing the Comsol Multiphysics packages is used for computation. It is found that the boundary slip has significant effect on the flow behaviour. The conclusion of the results are as follows:

(i) The slip parameter value influences the velocity profile significantly, and it is possible to create an optimal control problem to obtain the desired velocity profile based on the need of the application.

(ii) For the case of a constant radius artery, the boundary slip has dramatically affected the fluid flow in the artery. It affects not only the magnitude of the flow velocity significantly, but it also affects the pattern of velocity profile. That is, the larger the slip parameter value is, the larger the velocity magnitude near the arterial wall is and the flatter the velocity profile pattern is. Besides, the pressure which is a linear function along the domain length is influenced by the boundary slip as well. We found that the larger the slip parameter value is, the less the pressure and the steepness are. Lastly, the shear rate near the arterial wall along the length has been observed and it is found that the shear rate near the arterial wall in the constant radius artery domain is also affected by the boundary slip. That is, for the no-slip boundary, the shear rate is almost constant; while the boundary slip is applied, the shear rate decreases as the noise oscillation reduces. The larger the slip parameter is, the less shear rate and the noise oscillation are.

(iii) For the case of variable radius artery, the boundary slip has very significant influence on the blood flow in the domain. Firstly, we found that the velocity magnitude near the wall increases greatly while the maximum velocity at the center of the diameter cut-line decreases considerably when the slip parameter increases. Consequently, the velocity pattern becomes flatter. Additionally, as the slip parameter increases, the pressure along the length of the domain decreases nonlinearly. Since the inlet pressure is reduced while the outlet pressure is the set boundary condition, the pressure pattern becomes flatter, almost linear. Finally, the shear rate near the arterial wall in the variable radius artery domain is considered. The results show that the boundary slip also affect the shear rate and its pattern which is a non-linear increasing function. That is, for the no-

slip boundary, the shear rate difference between the inlet and the outlet is very large; while if the boundary slip is applied, the shear rate difference decreases. The larger the slip parameter is, the less the shear rate and the less the noise oscillation are.

CHAPTER 5

Summary and Future Research Directions

5.1 Summary

In this thesis, we study two kinds of micro-flows taking into account of micro-slip on the boundary, including the transient pulsatile flow of a modified second-grade fluid in the artery with boundary slip and the flow of a non-Newtonian fluid in a micro-tube with the transient pulsatile effect. Based on the previous work in the field, we have derived some analytical and numerical results. The main results are summarized as follows:

(1) Results for the effect of boundary slip on the transient pulsatile flow of a modified second-grade fluid

(i) The equations governing the transient pulsatile flow of a modified second-grade fluid have been formulated and established based on the Navier-Stokes equations and the continuity equation in the cylindrical polar coordinates. With the assumption of fully developed one-dimensional flow in the blood vessel, the field equations for the velocity field reduce to a second order partial differential equation with a pulsatile pressure force. The boundary conditions based on the Navier slip model has also been established.

(ii) The governing partial differential equations subject to the slip boundary condition have been solved to yield the exact solutions for the velocity field in the artery when $m = 0$. The basic method is to express the pressure gradient by the Fourier series and obtain the solution by using the superposition principle, that is, if u_n is the solution for $\frac{\partial p}{\partial z} = c_n \exp(in\omega t)$, then the complete solution for $\frac{\partial p}{\partial z} = \mathrm{Re}\left\{\sum_{n=0}^{\infty} c_n \exp(in\omega t)\right\}$ is $u = \sum_{n=0}^{\infty} \{\mathrm{Re}(u_n)\}$. Then the solution is found by the separation of variables.

(iii) The governing partial differential equations subject to the slip boundary condition have been solved to yield the numerical solutions for the velocity field in the artery when $m \neq 0$. The numerical approach for the problem is based on the finite different method.

(iv) Based on the mathematical model constructed and the solutions obtained for $m = 0$ and $m \neq 0$ with two radius sizes of the arteries, a number of investigations have been carried out to study the dynamic flow phenomena and the influence of the slip parameter on the flow behaviour. Form the investigatations, it can be concluded that

(a) The slip length has significant influence on the magnitude of the mean flow velocity of the blood in the artery and on the flow pattern and velocity profile on the cross-section. As l increases, the mean velocity of the blood flow in the artery increases especially in the artery with a small radius.

(b) When the slip boundary is applied, the pulsatile flow nature occurs significantly near the boundary wall.

(c) When the numerical technique is applied for $m \neq 0$, the slip length affects the convergence rate of the numerical solution to the exact solution and the convergence time, that is, the larger the slip length is, the slower the convergence rate of numerical results to the exact solutions is, and more time is needed to reach the steady state pulsatile flow.

(2) Results for the effect of boundary slip on the transient pulsatile flow of non-Newtonian blood flow

(i) The equations governing the problem, including the Navier-Stokes equations and the continuity equation, have been formulated in rectangular coordinate. The complete set of boundary conditions based on the Navier-Slip model in rectangular coordinate has also been developed.

(ii) The governing partial different equations subject to the boundary slip has been numerically calculated to yield the numerical solutions for the velocity field in the artery. The numerical approach for the problem is based on the finite element method.

(iii) Based on the mathematical model constructed and the numerical method established, a number of investigations have been carried out to study the dynamic flow phenomena and the influence of the slip parameters on the flow behaviour, and the following conclusions have been obtained.

(a) For the artery with a constant radius, when the slip length increases, the magnitude of the blood velocity near the wall increases more significantly than

at the centre of the artery. Therefore, the larger the slip length is, the flatter the flow pattern is. Moreover, the boundary slip also induces the pulsatile flow nature near the wall.

(b) The pressure near the arterial wall along the length is linear along the arterial length for the case of constant cross-section. Furthermore, its magnitude is also affected by the slip length. The larger the slip parameter value is, the less the pressure and steepness are.

(c) For the constant radius artery, the shear rate near the arterial wall along the arterial length is almost constant with a noise oscillation. When the slip length increases, the shear rate becomes smoother and its value is reduced.

(d) For an artery with variable radius along the arterial length, as the slip parameter increases, the magnitude of the blood velocity near the wall increases greatly and the flow pattern becomes flatter.

(e) For the artery with variable radius, the pressure near the arterial wall is a non-linear decreasing function along the arterial length. Moreover, when the slip parameter increases, the inlet pressure decreases and hence the pressure pattern becomes flatter.

(f) For the artery with variable radius, the shear rate near the arterial wall is a non-linear increasing function with oscillation noise along the arterial length. When the slip parameter increases, the shear rate along the arterial length decreases especially at the outlet of the artery with less oscillation noise and hence the shear rate pattern becomes flatter and smoother.

5.2 Future Research Directions

In this project, we use Fourier series expansion in time and Bessel function in space to develop and investigate analytical solutions, and establish numerical techniques to investigate the behaviour of unsteady slip flow in cylindrical coordinate and rectangular coordinate, respectively. Although some important results have been obtained, there are still problems for further research. One possible extension is to consider different types of boundary slip models including nonlinear models. Another further work is to study unsteady slip flows in more complex computation domains such as the arteries with branches and the real geometric artery domain.

APPENDIX A

Standard Finite Elements and Isoparametric Mapping

A.1 One-Dimensional Linear Bar Elements

For any line segment ($P_1(x_1, y_1, z_1)$,$P_2(x_2, y_2, z_2)$) in three-dimensional space, there is a invertible linear coordinate transformation T_l that maps from an arbitrary segment Ω_e in system of the (x, y, z) into a standard line segment ($Q_1(-1, 0, 0)$, $Q_2(1, 0, 0)$) of $\bar{\Omega}_e$ in system of the (ξ, ζ, η) as shown in figure A.1.
Firstly, we define a mapping of line segment in the standard segment as

$$Q = N_1(Q)Q_1 + N_2(Q)Q_2, \tag{A.1}$$

where $N_1(Q)+N_2(Q) = 1$ and $Q = [\xi, 0, 0]^T$ is any point on the standard segment. Furthermore, we can write

$$N_i(Q) = \begin{cases} 1, & \text{at node } i, \\ 0, & \text{otherwise.} \end{cases} \tag{A.2}$$

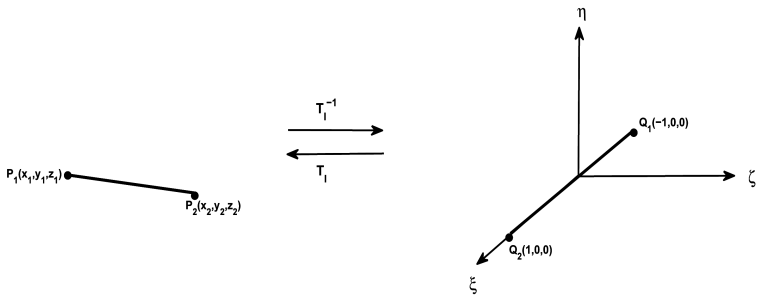

Figure A.1: Mapping between an arbitrary line segment $\Omega_e$in the system of (x, y, z) and the standard line segment in the system $\bar{\Omega}_e$ of (ξ, ζ, η).

Since $Q_1 = (-1, 0, 0)$ and $Q_2 = (1, 0, 0)$, we obtain

$$Q = N_1(Q) \begin{bmatrix} -1 \\ 0 \\ 0 \end{bmatrix} + N_2(Q) \begin{bmatrix} 1 \\ 0 \\ 0 \end{bmatrix}. \tag{A.3}$$

Hence, we have

$$\begin{bmatrix} \xi \\ 1 \end{bmatrix} = \begin{bmatrix} -1 & 1 \\ 1 & 1 \end{bmatrix} \begin{bmatrix} N_1(Q) \\ N_2(Q) \end{bmatrix}. \tag{A.4}$$

Solving this system of equations yields

$$N_1(Q) = \frac{1-\xi}{2}, \tag{A.5}$$

$$N_2(Q) = \frac{1+\xi}{2}. \tag{A.6}$$

We then apply $N_1(Q)$ and $N_2(Q)$ to a line segment mapping in an arbitrary three-dimensional segment, and then we get

$$P = N_1(Q)P_1 + N_2(Q)P_2, \tag{A.7}$$

where $P = (x, y, z), P_1 = (x_1, y_1, z_1),$ and $P_2 = (x_2, y_2, z_2)$ are coordinates in an arbitrary segment. Thus,

$$\begin{bmatrix} x \\ y \\ z \end{bmatrix} = \frac{1-\xi}{2} \begin{bmatrix} x_1 \\ y_1 \\ z_1 \end{bmatrix} + \frac{1+\xi}{2} \begin{bmatrix} x_2 \\ y_2 \\ z_2 \end{bmatrix}. \tag{A.8}$$

Rearranging (A.8) as a function of $Q = (\xi, 0, 0)$, we obtain the coordinate mapping $T_l(Q)$ as

$$\begin{aligned} \begin{bmatrix} x \\ y \\ z \end{bmatrix} &= \begin{bmatrix} \frac{x_2-x_1}{2} \\ \frac{y_2-y_1}{2} \\ \frac{z_2-z_1}{2} \end{bmatrix} \xi + \begin{bmatrix} \frac{x_2+x_1}{2} \\ \frac{y_2+y_1}{2} \\ \frac{z_2+z_1}{2} \end{bmatrix}, \\ &= \begin{bmatrix} T_{l,1}(\xi) \\ T_{l,2}(\xi) \\ T_{l,3}(\xi) \end{bmatrix}. \end{aligned} \tag{A.9}$$

We obtain that T_l is an invertible linear coordinate transformation from the standard segment to any arbitrary segment and its inverse is a linear transformation

from any arbitrary segment to the standard segment.
Moreover, we observe that
1) When $Q = (-1, 0, 0)$ is applied to the coordinate transformation T_l, we have $T_l(-1, 0, 0) = (x_1, y_1, z_1)$.
2) When $Q = (1, 0, 0)$ is applied to the coordinate transformation T_l, we have $T_l(1, 0, 0) = (x_2, y_2, z_2)$.

A.2 Two-Dimensional Triangular Elements

For any arbitrary triangular elements Ω_e formed by $\{ P_1(x_1, y_1, z_1),\ P_2(\, x_2, y_2, z_2\,),\ P_3(x_3, y_3, z_3)\,\}$, there is an invertible linear transformation T_{tri} that maps from the standard uniform triangular elements $\bar{\Omega}_e$ in system of the (ξ, ζ, η) formed by $\{\, Q_1(0, 0, 0),\, Q_2(1, 0, 0),\, Q_3(0, 1, 0)\,\}$ to an arbitrary triangular elements Ω_e in system of the (x, y, z).

We begin with the definition of the standard uniform triangular mapping as follows:

$$Q = N_1(Q)Q_1 + N_2(Q)Q_2 + N_3(Q)Q_3, \tag{A.10}$$

where $N_1(Q) + N_2(Q) + N_3(Q) = 1$ as in equation(A.2), and $Q = [\xi, \zeta, 0]^T$ is a point on the standard uniform triangular element.
Substituting Q_1, Q_2, Q_3, yields

$$\begin{bmatrix} \xi \\ \zeta \\ 0 \end{bmatrix} = N_1(Q) \begin{bmatrix} 0 \\ 0 \\ 0 \end{bmatrix} + N_2(Q) \begin{bmatrix} 1 \\ 0 \\ 0 \end{bmatrix} + N_3(Q) \begin{bmatrix} 0 \\ 1 \\ 0 \end{bmatrix}. \tag{A.11}$$

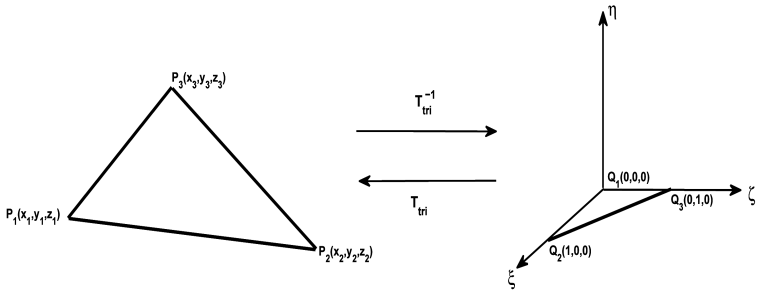

Figure A.2: Diagram showing the mapping between an arbitrary triangular element Ω_e in the system of (x, y, z) and the standard triangular element $\bar{\Omega}_e$ in the system of (ξ, ζ, η).

With the N_i function property, we obtain the following linear system of equations:

$$\begin{bmatrix} \xi \\ \zeta \\ 1 \end{bmatrix} = \begin{bmatrix} 0 & 1 & 0 \\ 0 & 0 & 1 \\ 1 & 1 & 1 \end{bmatrix} \begin{bmatrix} N_1(Q) \\ N_2(Q) \\ N_3(Q) \end{bmatrix}. \tag{A.12}$$

Solving the above system of equations, we obtain

$$\begin{aligned} N_1(Q) &= 1 - \xi - \zeta, \\ N_2(Q) &= \xi, \\ N_3(Q) &= \zeta. \end{aligned} \tag{A.13}$$

To obtain an invertible linear coordinate mapping T_{tri}, we then apply the $N_i(Q)$ functions to an arbitrary triangular mapping to yield

$$P = N_1(Q)P_1 + N_2(Q)P_2 + N_3(Q)P_3, \tag{A.14}$$

where $P = (x, y, z), P_1 = (x_1, y_1, z_1), P_2 = (x_2, y_2, z_2),$ and $P_3 = (x_3, y_3, z_3)$ are coordinate in an arbitrary triangular element.
That is,

$$\begin{bmatrix} x \\ y \\ z \end{bmatrix} = (1 - \xi - \zeta) \begin{bmatrix} x_1 \\ y_1 \\ z_1 \end{bmatrix} + \xi \begin{bmatrix} x_2 \\ y_2 \\ z_2 \end{bmatrix} + \zeta \begin{bmatrix} x_3 \\ y_3 \\ z_3 \end{bmatrix}. \tag{A.15}$$

Rearranging (A.15) being a function of $Q = (\xi, \zeta, 0)$, gives us a definition of coordinate mapping T_{tri} ,

$$\begin{aligned} \begin{bmatrix} x \\ y \\ z \end{bmatrix} &= \begin{bmatrix} x_2 - x_1 \\ y2 - y_1 \\ z_2 - z_1 \end{bmatrix} \xi + \begin{bmatrix} x_3 - x_1 \\ y_3 - y_1 \\ z_3 - z_1 \end{bmatrix} \zeta + \begin{bmatrix} x_1 \\ y_1 \\ z_1 \end{bmatrix}, \\ &= \begin{bmatrix} T_{tri,1}(\xi, \zeta, 0) \\ T_{tri,2}(\xi, \zeta, 0) \\ T_{tri,3}(\xi, \zeta, 0) \end{bmatrix}, \\ &= \begin{bmatrix} x(\xi, \zeta, 0) \\ y(\xi, \zeta, 0) \\ z(\xi, \zeta, 0) \end{bmatrix}. \end{aligned} \tag{A.16}$$

Hence, T_{tri} is an invertible linear coordinate transformation from the standard triangular element $\bar{\Omega}_e$ to any arbitrary triangular element Ω_e and its inverse is a

linear transformation from any arbitrary triangular element Ω_e to the standard uniform triangular element $\bar{\Omega}_e$.

Moreover, we observe that

1) When $Q = (0, 0, 0)$ is applied to the coordinate transformation T_{tri}, we have $T_{tri}(0, 0, 0) = (x_1, y_1, z_1)$.

2) When $Q = (1, 0, 0)$ is applied to the coordinate transformation T_{tri}, we have $T_{tri}(1, 0, 0) = (x_2, y_2, z_2)$.

3) When $Q = (0, 1, 0)$ is applied to the coordinate transformation T_{tri}, we have $T_{tri}(0, 1, 0) = (x_3, y_3, z_3)$.

Thus, the jacobian matrix under the coordinate transformation T_{tri} is given by

$$\begin{aligned} J_{tri} &= \frac{\partial(x, y, z)}{\partial(\xi, \zeta)}, \\ &= \begin{bmatrix} \frac{\partial x(\xi,\zeta,0)}{\partial \xi} & \frac{\partial x(\xi,\zeta,0)}{\partial \zeta} \\ \frac{\partial y(\xi,\zeta,0)}{\partial \xi} & \frac{\partial y(\xi,\zeta,0)}{\partial \zeta} \\ \frac{\partial z(\xi,\zeta),0}{\partial \xi} & \frac{\partial z(\xi,\zeta,0)}{\partial \zeta} \end{bmatrix}, \end{aligned} \tag{A.17}$$

where

$$\frac{\partial x(\xi, \zeta, 0)}{\partial \xi} = x_2 - x_1, \tag{A.18}$$

$$\frac{\partial x(\xi, \zeta, 0)}{\partial \zeta} = x_3 - x_1, \tag{A.19}$$

$$\frac{\partial y(\xi, \zeta, 0)}{\partial \xi} = y_2 - y_1, \tag{A.20}$$

$$\frac{\partial y(\xi, \zeta, 0)}{\partial \zeta} = y_3 - y_1, \tag{A.21}$$

$$\frac{\partial z(\xi, \zeta), 0}{\partial \xi} = z_2 - z_1, \tag{A.22}$$

$$\frac{\partial z(\xi, \zeta, 0)}{\partial \zeta} = z_3 - z_1. \tag{A.23}$$

Since T_{tri} is an invertible mapping, there exists a mapping $T_{tri}^{-1}(x, y, z) = \begin{bmatrix} \xi(x, y, z) \\ \zeta(x, y, z) \\ 0 \end{bmatrix}$ from the coordinate system (x, y, z) to the coordinate system (ξ, ζ, η).

We then define the shape function at node i in an arbitrary triangular element, Φ_i^e, as

$$\Phi_i^e(x, y, z) = N_i(\xi(x, y, z), \zeta(x, y, z)) \qquad \text{for } i = 1, 2, 3. \tag{A.24}$$

Vice versa, we have

$$N_i(\xi,\zeta) = \Phi_i^e(x(\xi,\zeta,0), y(\xi,\zeta,0), z(\xi,\zeta,0)) \qquad \text{for } i = 1,2,3. \tag{A.25}$$

To approximate the unknown variables in this element type, we choose three nodes of an arbitrary triangular element Ω_e for interpolation. We suppose that $\{f_1, f_2, f_3\}$ be a set of three values of the unknown function f at node $1, 2$ and 3 of this element, respectively. Hence, the function f in Ω_e can be interpolated by

$$\begin{aligned} f^e(x,y,z) &= \Phi_1^e(x,y,z)f_1 + \Phi_2^e(x,y,z)f_2 + \Phi_3^e(x,y,z)f_3, \\ &= \sum_{i=1}^{3} \Phi_i^e(x,y,z)f_i. \end{aligned} \tag{A.26}$$

By using the coordinate transformation, equation (A.26) becomes

$$\begin{aligned} f^e(x,y,z) &= \sum_{i=1}^{3} \Phi_i^e(x,y,z)f_i, \\ &= \sum_{i=1}^{3} \Phi_i^e(x(\xi,\zeta,0), y(\xi,\zeta,0), z(\xi,\zeta,0))f_i, \\ &= \sum_{i=1}^{3} N_i(\xi,\zeta,0)f_i, \\ &= g^e(\xi,\zeta,0), \end{aligned} \tag{A.27}$$

where $g^e(\xi,\zeta,0)$ is a coordinate transformed function of the function f.

Using the property of transformation of multiple integral from rectangular to curvilinear coordinate, the integration of the unknown function f can be calculated as

$$\begin{aligned} \iint_{\Gamma} f(x,y,z)d\Gamma &= \iint_{\bar{\Omega}_e} g(\xi,\zeta,0)det(J_{tri})d\xi d\zeta, \\ &= \int_0^1 \int_0^{1-\zeta} g(\xi,\zeta,0)det(J_{tri})d\xi d\zeta, \end{aligned} \tag{A.28}$$

where

$$det(J_{tri}) = \left\| \left| \frac{\partial T_{tri}^{-1}(\xi,\zeta,0)}{\partial \xi} \times \frac{\partial T_{tri}^{-1}(\xi,\zeta,0)}{\partial \zeta} \right| \right\|,$$
$$= \left\| det \left(\begin{bmatrix} i & j & k \\ \frac{x(\xi,\zeta,0)}{\partial \xi} & \frac{y(\xi,\zeta,0)}{\partial \xi} & \frac{z(\xi,\zeta,0)}{\partial \xi} \\ \frac{x(\xi,\zeta,0)}{\partial \zeta} & \frac{y(\xi,\zeta,0)}{\partial \zeta} & \frac{z(\xi,\zeta,0)}{\partial \zeta} \end{bmatrix} \right) \right\|.$$

A.3 Two-Dimensional Quadrilateral Elements

Let $\{P_1(x_1,y_1,z_1), P_2(x_2,y_2,z_2), P_3(x_3,y_3,z_3), P_4(x_4,y_4,z_4)\}$ form an arbitrary quadrilateral element Ω_e in system of (x,y,z) coordinate and $\{\ Q_1(1,1,0), Q_2(-1,1,0), Q_3(-1,-1,0), Q_4(1,-1,0)\ \}$ form the standard quadrilateral element $\bar{\Omega}_e$ in system of (ξ,ζ,η). To derive an coordinate transformation T_{sq}, we then apply a superposition of shape functions for line segment in ξ-direction and ζ-direction to $N_i(Q)$, i.e.

$$N_1(Q) = \tfrac{1}{2}(1+\xi)\cdot\tfrac{1}{2}(1+\zeta) = \frac{1}{4}(1+\xi)(1+\zeta), \tag{A.29}$$
$$N_2(Q) = \tfrac{1}{2}(1-\xi)\cdot\tfrac{1}{2}(1+\zeta) = \frac{1}{4}(1-\xi)(1+\zeta), \tag{A.30}$$
$$N_3(Q) = \tfrac{1}{2}(1-\xi)\cdot\tfrac{1}{2}(1-\zeta) = \frac{1}{4}(1-\xi)(1-\zeta), \tag{A.31}$$
$$N_4(Q) = \tfrac{1}{2}(1+\xi)\cdot\tfrac{1}{2}(1-\zeta) = \frac{1}{4}(1+\xi)(1-\zeta). \tag{A.32}$$

Note that $N_i(Q)$ preserves the property of equation (A.2). Therefore, a coordinate transformation from the standard quadrilateral element to an arbitrary

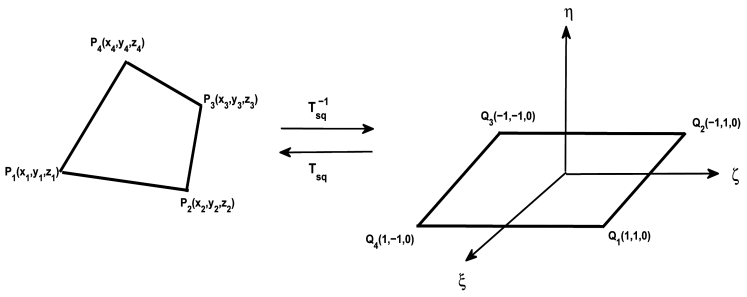

Figure A.3: An arbitrary quadrilateral element Ω_e in the system of (x,y,z) and the standard quadrilateral element $\bar{\Omega}_e$ in the system of (ξ,ζ,η).

quadrilateral element is defined by

$$P = N_1(Q)P_1 + N_2(Q)P_2 + N_3(Q)P_3 + N_4(Q)P_4, \tag{A.33}$$

where $P = (x, y, z), P_1 = (x_1, y_1, z_1), P_2 = (x_2, y_2, z_2), P_3 = (x_3, y_3, z_3)$ and $P_4 = (x_4, y_4, z_4)$ are coordinates in an arbitrary quadrilateral element with the shape function $N_i(Q)$ defined by the equations (A.29)- (A.32). We then express equation (A.33) in term of the system of equations,

$$\begin{aligned}
\begin{bmatrix} x \\ y \\ z \end{bmatrix} &= \frac{1}{4}(1+\xi)(1+\zeta)\begin{bmatrix} x_1 \\ y_1 \\ z_1 \end{bmatrix} + \frac{1}{4}(1-\xi)(1+\zeta)\begin{bmatrix} x_2 \\ y_2 \\ z_2 \end{bmatrix} + \frac{1}{4}(1-\xi)(1-\zeta)\begin{bmatrix} x_3 \\ y_3 \\ z_3 \end{bmatrix} \\
&\quad + \frac{1}{4}(1+\xi)(1-\zeta)\begin{bmatrix} x_4 \\ y_4 \\ z_4 \end{bmatrix}, \\
&= \begin{bmatrix} T_{sq,1}(\xi,\zeta,0) \\ T_{sq,2}(\xi,\zeta,0) \\ T_{sq,2}(\xi,\zeta,0) \end{bmatrix} \\
&= \begin{bmatrix} x(\xi,\zeta,0) \\ y(\xi,\zeta,0) \\ z(\xi,\zeta,0) \end{bmatrix}.
\end{aligned} \tag{A.34}$$

Obviously, T_{sq} is a coordinate mapping from $(\xi, \zeta, 0)$ in $\bar{\Omega}_e$ to (x, y, z) in Ω_e i.e. it is a coordinate transformation from the standard quadrilateral element to any arbitrary quadrilateral element and its inverse is a coordinate transformation from any arbitrary quadrilateral element to the standard quadrilateral element.
Moreover, we observe that
1) When $Q = (1, 1, 0)$ is applied to the coordinate transformation T_{sq}, we have $T_{sq}(1, 1, 0) = (x_1, y_1, z_1)$.
2) When $Q = (-1, 1, 0)$ is applied to the coordinate transformation T_{sq}, we have $T_{sq}(-1, 1, 0) = (x_2, y_2, z_2)$.
3) When $Q = (-1, -1, 0)$ is applied to the coordinate transformation T_{sq}, we have $T_{sq}(-1, -1, 0) = (x_3, y_3, z_3)$.
4) When $Q = (1, -1, 0)$ is applied to the coordinate transformation T_{sq}, we have $T_{sq}(1, -1, 0) = (x_4, y_4, z_4)$.

Similarly to the triangular element, the Jacobian matrix under the coordinate

transformation T_{sq} is calculated by

$$J_{sq} = \frac{\partial(x,y,z)}{\partial(\xi,\zeta)}, \\ = \begin{bmatrix} \frac{x(\xi,\zeta,0)}{\partial\xi} & \frac{x(\xi,\zeta,0)}{\partial\zeta} \\ \frac{y(\xi,\zeta,0)}{\partial\xi} & \frac{y(\xi,\zeta,0)}{\partial\zeta} \\ \frac{z(\xi,\zeta,0)}{\partial\xi} & \frac{z(\xi,\zeta,0)}{\partial\zeta} \end{bmatrix}. \tag{A.35}$$

where

$$\frac{\partial x(\xi,\zeta,0)}{\partial\xi} = \frac{1}{4}\left[(1+\zeta)(x_1-x_2)+(1-\zeta)(x_4-x_3)\right], \tag{A.36}$$

$$\frac{\partial x(\xi,\zeta,0)}{\partial\zeta} = \frac{1}{4}\left[(1+\xi)(x_1-x_4)+(1-\xi)(x_2-x_4)\right], \tag{A.37}$$

$$\frac{\partial y(\xi,\zeta,0)}{\partial\xi} = \frac{1}{4}\left[(1+\zeta)(y_1-y_2)+(1-\zeta)(y_4-y_3)\right], \tag{A.38}$$

$$\frac{\partial y(\xi,\zeta,0)}{\partial\zeta} = \frac{1}{4}\left[(1+\xi)(y_1-y_4)+(1-\xi)(y_2-y_3)\right], \tag{A.39}$$

$$\frac{\partial z(\xi,\zeta),0}{\partial\xi} = \frac{1}{4}\left[(1+\zeta)(z_1-z_2)+(1-\zeta)(z_4-z_3)\right], \tag{A.40}$$

$$\frac{\partial z(\xi,\zeta,0)}{\partial\zeta} = \frac{1}{4}\left[(1+\xi)(z_1-z_4)+(1-\xi)(z_2-z_3)\right]. \tag{A.41}$$

According to the invertible mapping T_{sq}, there exists a mapping $T_{sq}^{-1}(x,y,z) = \begin{bmatrix} \xi(x,y,z) \\ \zeta(x,y,z) \\ 0 \end{bmatrix}$ from the coordinate system (x,y,z) to the coordinate system (ξ,ζ,η). We then define the shape function at node i in an arbitrary quadrilateral element, ϕ_i^e, as

$$\Phi_i^e(x,y,z) = N_i(\xi(x,y,z),\zeta(x,y,z)) \qquad \text{for } i=1,2,3,4. \tag{A.42}$$

In the other way, we have

$$N_i(\xi,\zeta) = \Phi_i^e(x(\xi,\zeta,0),y(\xi,\zeta,0),z(\xi,\zeta,0)) \qquad \text{for } i=1,2,3,4. \tag{A.43}$$

To approximate the unknown variables in this element type, we choose three nodes of an arbitrary triangular element Ω_e for interpolation. By letting $\{f_1,f_2,f_3,f_4\}$ be a set of four values of the unknown function f at node $1,2,3$ and 4 of this

element, respectively. Hence, the function f in Ω_e can be interpolated by

$$\begin{aligned} f^e(x,y,z) &= \Phi_1^e(x,y,z)f_1 + \Phi_2^e(x,y,z)f_2 + \Phi_3^e(x,y,z)f_3 + \Phi_4^e(x,y,z)f_4, \\ &= \sum_{i=1}^{4} \Phi_i^e(x,y,z)f_i. \end{aligned} \tag{A.44}$$

By using the coordinate transformation, equation (A.44) becomes

$$\begin{aligned} f^e(x,y,z) &= \sum_{i=1}^{4} \Phi_i^e(x,y,z)f_i, \\ &= \sum_{i=1}^{4} \Phi_i^e(x(\xi,\zeta,0), y(\xi,\zeta,0), z(\xi,\zeta,0))f_i, \\ &= \sum_{i=1}^{4} N_i(\xi,\zeta,0)f_i, \\ &= g^e(\xi,\zeta,0), \end{aligned} \tag{A.45}$$

where $g^e(\xi,\zeta,0)$ is a coordinate transformed function of the function f.

Using the property of transformation of multiple integral from rectangular to curvilinear coordinate, the integration of the unknown function f can be calculated as

$$\begin{aligned} \iint_{\Gamma} f(x,y,z)d\Gamma &= \iint_{\bar{\Omega}_e} g(\xi,\zeta,0)det(J_{sq})d\xi d\zeta, \\ &= \int_{-1}^{1}\int_{-1}^{1} g(\xi,\zeta,0)det(J_{sq})d\xi d\zeta, \end{aligned} \tag{A.46}$$

where

$$\begin{aligned} det(J_{sq}) &= \left\| \frac{\partial T_{sq}^{-1}(\xi,\zeta,0)}{\partial \xi} \times \frac{\partial T_{sq}^{-1}(\xi,\zeta,0)}{\partial \zeta} \right\|, \\ &= \left\| det \begin{bmatrix} i & j & k \\ \frac{x(\xi,\zeta,0)}{\partial \xi} & \frac{y(\xi,\zeta,0)}{\partial \xi} & \frac{z(\xi,\zeta,0)}{\partial \xi} \\ \frac{x(\xi,\zeta,0)}{\partial \zeta} & \frac{y(\xi,\zeta,0)}{\partial \zeta} & \frac{z(\xi,\zeta,0)}{\partial \zeta} \end{bmatrix} \right\|. \end{aligned}$$

A.4 Three-Dimensional Tetrahedral Elements

Now we consider the coordinate transformation T_{te} between an arbitrary tetrahedral element Ω formed by $\{ P_1(x_1, y_1, z_1), P_2(x_2, y_2, z_2), P_3(x_3, y_3, z_3), P_4(x_4, y_4, z_4) \}$ and the standard tetrahedral element $\bar{\Omega}_e$ formed by $\{ Q_1(0,0,0), Q_2(1,0,0), Q_3(0,1,0), Q_4(0,0,1) \}$. we define the standard tetrahedral element mapping formed by $\{Q_1, Q_2, Q_3, Q_4\}$ as

$$Q = N_1(Q)Q_1 + N_2(Q)Q_2 + N_3(Q)Q_3 + N_4(Q)Q_4, \tag{A.47}$$

where $N_1(Q) + N_2(Q) + N_3(Q) + N_4(Q) = 1$ similarly to equation (A.2), $Q = [\xi, \zeta, \eta]^T$ is a point on the standard tetrahedral element.

Substituting Q_1, Q_2, Q_3, Q_4, yields

$$\begin{bmatrix} \xi \\ \zeta \\ \eta \end{bmatrix} = N_1(Q) \begin{bmatrix} 0 \\ 0 \\ 0 \end{bmatrix} + N_2(Q) \begin{bmatrix} 1 \\ 0 \\ 0 \end{bmatrix} + N_3(Q) \begin{bmatrix} 0 \\ 1 \\ 0 \end{bmatrix} + N_4(Q) \begin{bmatrix} 0 \\ 0 \\ 1 \end{bmatrix}. \tag{A.48}$$

With the N_i function property, we obtain the following linear system equation:

$$\begin{bmatrix} \xi \\ \zeta \\ \eta \\ 1 \end{bmatrix} = \begin{bmatrix} 0 & 1 & 0 & 0 \\ 0 & 0 & 1 & 0 \\ 0 & 0 & 0 & 1 \\ 1 & 1 & 1 & 1 \end{bmatrix} \begin{bmatrix} N_1(Q) \\ N_2(Q) \\ N_3(Q) \\ N_4(Q) \end{bmatrix}. \tag{A.49}$$

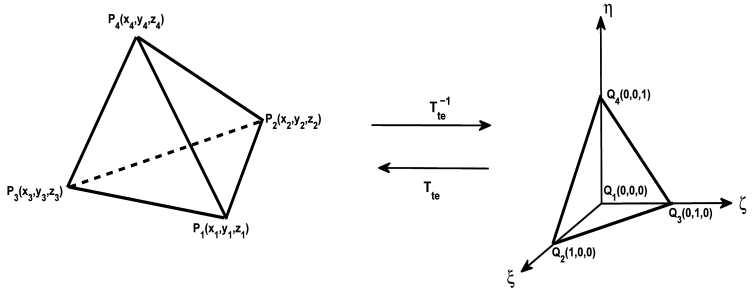

Figure A.4: Mapping between an arbitrary tetrahedral element Ω_e in the system of (x, y, z) and the standard tetrahedral element $\bar{\Omega}_e$ in the system of (ξ, ζ, η).

By solving the equations system, we obtain

$$N_1(Q) = 1 - \xi - \zeta - \eta, \tag{A.50}$$
$$N_2(Q) = \xi, \tag{A.51}$$
$$N_3(Q) = \zeta, \tag{A.52}$$
$$N_4(Q) = \eta. \tag{A.53}$$

To obtain an invertible linear coordinate mapping T_{tetra}, we then apply the $N_i(Q)$ functions to an arbitrary triangular mapping. This yields

$$P = N_1(Q)P_1 + N_2(Q)P_2 + N_3(Q)P_3 + N_4(Q)P_4, \tag{A.54}$$

where $P = (x, y, z), P_1 = (x_1, y_1, z_1), P_2 = (x_2, y_2, z_2), P_3 = (x_3, y_3, z_3),$ and $P_4 = (x_4, y_4, z_4)$ are coordinate in an arbitrary triangular element.
That is,

$$\begin{bmatrix} x \\ y \\ z \end{bmatrix} = (1 - \xi - \zeta) \begin{bmatrix} x_1 \\ y_1 \\ z_1 \end{bmatrix} + \xi \begin{bmatrix} x_2 \\ y_2 \\ z_2 \end{bmatrix} + \zeta \begin{bmatrix} x_3 \\ y_3 \\ z_3 \end{bmatrix} + \eta \begin{bmatrix} x_4 \\ y_4 \\ z_4 \end{bmatrix}. \tag{A.55}$$

Rearranging (A.55) being a function of $Q = (\xi, \zeta, \eta)$ gives us a linear coordinate mapping T_{tetra} ,

$$\begin{aligned} \begin{bmatrix} x \\ y \\ z \end{bmatrix} &= \begin{bmatrix} x_2 - x_1 \\ y2 - y_1 \\ z_2 - z_1 \end{bmatrix} \xi + \begin{bmatrix} x_3 - x_1 \\ y_3 - y_1 \\ z_3 - z_1 \end{bmatrix} \zeta + \begin{bmatrix} x_4 - x_1 \\ y_4 - y_1 \\ z_4 - z_1 \end{bmatrix} \eta + \begin{bmatrix} x_1 \\ y_1 \\ z_1 \end{bmatrix}, \\ &= \begin{bmatrix} T_{te,1}(\xi, \zeta, \eta) \\ T_{te,2}(\xi, \zeta, \eta) \\ T_{te,3}(\xi, \zeta, \eta) \end{bmatrix} \\ &= \begin{bmatrix} x(\xi, \zeta, \eta) \\ y(\xi, \zeta, \eta) \\ z(\xi, \zeta, \eta) \end{bmatrix}. \end{aligned} \tag{A.56}$$

Obviously, T_{te} is an invertible linear coordinate transformation from the standard tetrahedral element $\bar{\Omega}_e$ to any arbitrary tetrahedral element Ω_e and its inverse is a linear transformation from any arbitrary tetrahedral element Ω_e to the standard tetrahedral element $\bar{\Omega}_e$.
Moreover, we observe that
1) When $Q = (0, 0, 0)$ is applied to the coordinate transformation T_{te}, we have

$T_{te}(0,0,0) = (x_1, y_1, z_1)$,
2) When $Q = (1,0,0)$ is applied to the coordinate transformation T_{te}, we have $T_{te}(1,0,0) = (x_2, y_2, z_2)$,
3) When $Q = (0,1,0)$ is applied to the coordinate transformation T_{te}, we have $T_{te}(0,1,0) = (x_3, y_3, z_3)$,
4) When $Q = (0,0,1)$ is applied to the coordinate transformation T_{te}, we have $T_{te}(0,0,1) = (x_4, y_4, z_4)$.

Analogously, the Jacobian matrix under the coordinate transformation T_{te} is written by

$$J_{te} = \frac{\partial(x,y,z)}{\partial(\xi,\zeta,\eta)}, = \begin{bmatrix} \frac{x(\xi,\zeta,\eta)}{\partial\xi} & \frac{x(\xi,\zeta,\eta)}{\partial\zeta} & \frac{x(\xi,\zeta,\eta)}{\partial\eta} \\ \frac{y(\xi,\zeta,\eta)}{\partial\xi} & \frac{y(\xi,\zeta,\eta)}{\partial\zeta} & \frac{y(\xi,\zeta,\eta)}{\partial\eta} \\ \frac{z(\xi,\zeta,\eta)}{\partial\xi} & \frac{z(\xi,\zeta,\eta)}{\partial\zeta} & \frac{z(\xi,\zeta,\eta)}{\partial\eta} \end{bmatrix}. \tag{A.57}$$

where

$$\frac{\partial x(\xi,\zeta,\eta)}{\partial\xi} = x_2 - x_1, \tag{A.58}$$
$$\frac{\partial x(\xi,\zeta,\eta)}{\partial\zeta} = x_3 - x_1, \tag{A.59}$$
$$\frac{\partial x(\xi,\zeta,\eta)}{\partial\eta} = x_4 - x_1, \tag{A.60}$$
$$\frac{\partial y(\xi,\zeta,\eta)}{\partial\xi} = y_2 - y_1, \tag{A.61}$$
$$\frac{\partial y(\xi,\zeta,\eta)}{\partial\zeta} = y_3 - y_1, \tag{A.62}$$
$$\frac{\partial y(\xi,\zeta,\eta)}{\partial\eta} = y_4 - y_1, \tag{A.63}$$
$$\frac{\partial z(\xi,\zeta),\eta}{\partial\xi} = z_2 - z_1, \tag{A.64}$$
$$\frac{\partial z(\xi,\zeta,\eta)}{\partial\zeta} = z_3 - z_1, \tag{A.65}$$
$$\frac{\partial z(\xi,\zeta,\eta)}{\partial\eta} = z_4 - z_1. \tag{A.66}$$

According to the invertible mapping T_{sq}, there exists a mapping $T_{sq}^{-1}(x,y,z) = \begin{bmatrix} \xi(x,y,z) \\ \zeta(x,y,z) \\ \eta(x,y,z) \end{bmatrix}$ from the coordinate system (x,y,z) to the coordinate system (ξ,ζ,η).

We then define the shape function at node i in an arbitrary quadrilateral element, ϕ_i^e, as

$$\phi_i^e(x,y,z) = N_i(\xi(x,y,z),\zeta(x,y,z),\eta(x,y,z)) \qquad \text{for } i = 1,2,3,4. \tag{A.67}$$

In the other way, we have

$$N_i(\xi,\zeta\eta) = \phi_i^e(x(\xi,\zeta,\eta),y(\xi,\zeta,\eta),z(\xi,\zeta,\eta)) \qquad \text{for } i = 1,2,3,4. \tag{A.68}$$

To approximate the unknown variables in this element type, we choose three nodes of an arbitrary triangular element Ω_e for interpolation. Namely, let $\{f_1, f_2, f_3, f_4\}$ be the value of the unknown function f at node $1, 2, 3$ and 4 of this element, respectively. Hence, the function f in Ω_e can be interpolated by

$$\begin{aligned} f^e(x,y,z) &= \phi_1^e(x,y,z)f_1 + \phi_2^e(x,y,z)f_2 + \phi_3^e(x,y,z)f_3 + \phi_4^e(x,y,z)f_4, \\ &= \sum_{i=1}^{4} \phi_i^e(x,y,z)f_i. \end{aligned} \tag{A.69}$$

By using the coordinate transformation, equation (A.44) becomes

$$\begin{aligned} f^e(x,y,z) &= \sum_{i=1}^{4} \phi_i^e(x,y,z)f_i, \\ &= \sum_{i=1}^{4} \phi_i^e(x(\xi,\zeta,\eta),y(\xi,\zeta,\eta),z(\xi,\zeta,\eta))f_i, \\ &= \sum_{i=1}^{4} N_i(\xi,\zeta,\eta)f_i, \\ &= g^e(\xi,\zeta,\eta). \end{aligned} \tag{A.70}$$

where $g^e(\xi,\zeta,\eta)$ is a coordinate transformed function of the function f.

Using the property of transformation of multiple integral from rectangular to curvilinear coordinate, the integration of the unknown function f can be calculated as

$$\begin{aligned} \iiint_{\Omega} f(x,y,z)d\Omega &= \iiint_{\bar{\Omega}_e} g(\xi,\zeta,\eta)det(J_{te})d\eta d\zeta d\xi, \\ &= \int_0^1 \int_0^{1-\xi} \int_0^{1-\xi-\zeta} g(\xi,\zeta\eta)det(J_{te})d\eta d\zeta d\xi, \end{aligned} \tag{A.71}$$

where

$$det(J_{te}) = det\left(\begin{bmatrix} \frac{x(\xi,\zeta,\eta)}{\partial\xi} & \frac{y(\xi,\zeta,\eta)}{\partial\xi} & \frac{z(\xi,\zeta,\eta)}{\partial\xi} \\ \frac{x(\xi,\zeta,\eta)}{\partial\zeta} & \frac{y(\xi,\zeta,\eta)}{\partial\zeta} & \frac{z(\xi,\zeta,\eta)}{\partial\zeta} \\ \frac{x(\xi,\zeta,\eta)}{\partial\eta} & \frac{y(\xi,\zeta,\eta)}{\partial\eta} & \frac{z(\xi,\zeta,\eta)}{\partial\eta} \end{bmatrix}\right). \tag{A.72}$$

A.5 Three-Dimensional Triangular Prismatic Elements

Let $\{ P_1(x_1, y_1, z_1), P_2(x_2, y_2, z_2), P_3(x_3, y_3, z_3), P_4(x_4, y_4, z_4), P_5(x_5, y_5, z_5), P_6(x_6, y_6, z_6) \}$ form any arbitrary triangular prismatic element Ω_e in system of (x, y, z) coordinate and $\{ Q_1(0, 0, -1), Q_2(1, 0, -1), Q_3(0, 1, -1), Q_4(0, 0, 1), Q_5(1, 0, 1), Q_6(0, 1, 1) \}$ form the standard triangular prismatic element $\bar{\Omega}_e$ in system of (ξ, ζ, η). Since this element is composed of triangles and quadrilaterals, to derive an coordinate transformation T_{pr}, we then apply a superposition of shape functions for triangles and line elements to achieve $N_i(Q)$.
Form the shape functions of triangle element equation (A.13), we have

$$N_1^\star(Q) = 1 - \xi - \zeta, \tag{A.73}$$

$$N_2^\star(Q) = \xi, \tag{A.74}$$

$$N_3^\star(Q) = \zeta, \tag{A.75}$$

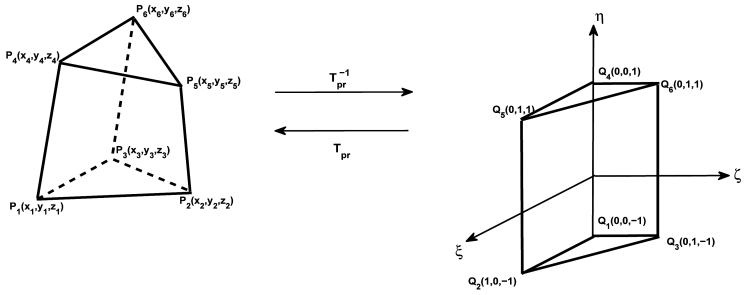

Figure A.5: Mapping between an arbitrary triangular prismatic element Ω_e in the system of (x, y, z) and the standard triangular prismatic $\bar{\Omega}_e$ in the system of (ξ, ζ, η).

Then combine these shape function to the shape function of line segment, yields

$$N_1(Q) = N_1^\star(Q) \cdot \tfrac{1}{2}(1-\eta) = \frac{1}{2}(1-\xi-\zeta)(1-\eta), \tag{A.76}$$

$$N_2(Q) = N_2^\star(Q) \cdot \tfrac{1}{2}(1-\eta) = \frac{1}{2}\xi(1-\eta), \tag{A.77}$$

$$N_3(Q) = N_3^\star(Q) \cdot \tfrac{1}{2}(1-\eta) = \frac{1}{2}\zeta(1-\eta), \tag{A.78}$$

$$N_4(Q) = N_1^\star(Q) \cdot \tfrac{1}{2}(1+\eta) = \frac{1}{2}(1-\xi-\zeta)(1+\eta), \tag{A.79}$$

$$N_5(Q) = N_2^\star(Q) \cdot \tfrac{1}{2}(1+\eta) = \frac{1}{2}\xi(1+\eta), \tag{A.80}$$

$$N_6(Q) = N_3^\star(Q) \cdot \tfrac{1}{2}(1+\eta) = \frac{1}{2}\zeta(1+\eta). \tag{A.81}$$

Note that $N_i(Q)$ preserves the property of equation (A.2).
Thus, the coordinate transformation is defined as

$$P = N_1(Q)P_1 + N_2(Q)P_2 + N_3(Q)P_3 + N_4(Q)P_4 + N_5(Q)P_5 + N_6(Q)P_6, \tag{A.82}$$

where $P = (x, y, z), P_1 = (x_1, y_1, z_1), P_2 = (x_2, y_2, z_2), P_3 = (x_3, y_3, z_3), P_4 = (x_4, y_4, z_4), P_5 = (x_5, y_5, z_5)$ and $P_6 = (x_6, y_6, z_6)$ are coordinate in an arbitrary quadrilateral element with $N_i(Q)$ defined as (A.76) - (A.81).
Expressing equation (A.82) in term of the system of equations, gives

$$\begin{aligned}
\begin{bmatrix} x \\ y \\ z \end{bmatrix} &= \frac{1}{2}(1-\xi-\zeta)(1-\eta)\begin{bmatrix} x_1 \\ y_1 \\ z_1 \end{bmatrix} + \frac{1}{2}\xi(1-\eta)\begin{bmatrix} x_2 \\ y_2 \\ z_2 \end{bmatrix} + \frac{1}{2}\zeta(1-\eta)\begin{bmatrix} x_3 \\ y_3 \\ z_3 \end{bmatrix} \\
&\quad + \frac{1}{2}(1-\xi-\zeta)(1+\eta)\begin{bmatrix} x_4 \\ y_4 \\ z_4 \end{bmatrix} + \frac{1}{2}\xi(1+\eta)\begin{bmatrix} x_5 \\ y_5 \\ z_5 \end{bmatrix} + \frac{1}{2}\zeta(1+\eta)\begin{bmatrix} x_6 \\ y_6 \\ z_6 \end{bmatrix}, \\
&= \begin{bmatrix} T_{pr,1}(\xi,\zeta,\eta) \\ T_{pr,2}(\xi,\zeta,\eta) \\ T_{pr,3}(\xi,\zeta,\eta) \end{bmatrix}.
\end{aligned} \tag{A.83}$$

Obviously, T_{pr} is a coordinate mapping from (ξ, ζ, η) in $\bar{\Omega}_e$ to (x, y, z) in Ω_e i.e. it is a coordinate transformation from the standard quadrilateral element to any arbitrary quadrilateral element and its inverse is a coordinate transformation from any arbitrary quadrilateral element to the standard quadrilateral element.
Moreover, we observe that
1) When $Q = (0, 0, -1)$ is applied to the coordinate transformation T_{pr}, we have

$T_{pr}(0,0,-1) = (x_1, y_1, z_1)$.
2) When $Q = (1,0,-1)$ is applied to the coordinate transformation T_{pr}, we have $T_{pr}(1,0,-1) = (x_2, y_2, z_2)$.
3) When $Q = (0,1,-1)$ is applied to the coordinate transformation T_{pr}, we have $T_{pr}(0,1,-1) = (x_3, y_3, z_3)$.
4) When $Q = (0,0,1)$ is applied to the coordinate transformation T_{pr}, we have $T_{pr}(0,0,1) = (x_4, y_4, z_4)$.
5) When $Q = (1,0,1)$ is applied to the coordinate transformation T_{pr}, we have $T_{pr}(1,0,1) = (x_5, y_5, z_5)$.
6) When $Q = (0,1,1)$ is applied to the coordinate transformation T_{pr}, we have $T_{pr}(0,1,1) = (x_6, y_6, z_6)$.

Again, the jacobian matrix under the coordinate transformation T_{pr} is represented by

$$J_{pr} = \frac{\partial(x,y,z)}{\partial(\xi,\zeta,\eta)}, \\ = \begin{bmatrix} \frac{x(\xi,\zeta,\eta)}{\partial\xi} & \frac{x(\xi,\zeta,\eta)}{\partial\zeta} & \frac{x(\xi,\zeta,\eta)}{\partial\eta} \\ \frac{y(\xi,\zeta,\eta)}{\partial\xi} & \frac{y(\xi,\zeta,\eta)}{\partial\zeta} & \frac{y(\xi,\zeta,\eta)}{\partial\eta} \\ \frac{z(\xi,\zeta,\eta)}{\partial\xi} & \frac{z(\xi,\zeta,\eta)}{\partial\zeta} & \frac{z(\xi,\zeta,\eta)}{\partial\eta} \end{bmatrix}. \tag{A.84}$$

where

$$\frac{\partial x(\xi,\zeta,\eta)}{\partial\xi} = \frac{1}{2}\left[(1-\eta)(x_2-x_1) + (1+\eta)(x_5-x_4)\right], \tag{A.85}$$

$$\frac{\partial x(\xi,\zeta,\eta)}{\partial\zeta} = \frac{1}{2}\left[(1-\eta)(x_3-x_1) + (1+\eta)(x_6-x_4)\right], \tag{A.86}$$

$$\frac{\partial x(\xi,\zeta,\eta)}{\partial\eta} = \frac{1}{2}\left[(1-\xi-\zeta)(x_4-x_1) + \xi(x_5-x_2) + \zeta(x_6-x_3)\right], \tag{A.87}$$

$$\frac{\partial y(\xi,\zeta,\eta)}{\partial\xi} = \frac{1}{2}\left[(1-\eta)(y_2-y_1) + (1+\eta)(y_5-y_4)\right], \tag{A.88}$$

$$\frac{\partial y(\xi,\zeta,\eta)}{\partial\zeta} = \frac{1}{2}\left[(1-\eta)(y_3-y_1) + (1+\eta)(y_6-y_4)\right], \tag{A.89}$$

$$\frac{\partial y(\xi,\zeta,\eta)}{\partial\eta} = \frac{1}{2}\left[(1-\xi-\zeta)(y_4-y_1) + \xi(y_5-y_2) + \zeta(y_6-y_3)\right], \tag{A.90}$$

$$\frac{\partial z(\xi,\zeta),\eta}{\partial\xi} = \frac{1}{2}\left[(1-\eta)(z_2-z_1) + (1+\eta)(z_5-z_4)\right], \tag{A.91}$$

$$\frac{\partial z(\xi,\zeta,\eta)}{\partial\zeta} = \frac{1}{2}\left[(1-\eta)(z_3-z_1) + (1+\eta)(z_6-z_4)\right], \tag{A.92}$$

$$\frac{\partial z(\xi,\zeta,\eta)}{\partial\eta} = \frac{1}{2}\left[(1-\xi-\zeta)(z_4-z_1) + \xi(z_5-z_2) + \zeta(z_6-z_3)\right]. \tag{A.93}$$

Because of the invertible mapping T_{pr}, there exists a mapping $T_{pr}^{-1}(x,y,z) = \begin{bmatrix}\xi(x,y,z)\\ \zeta(x,y,z)\\ \eta(x,y,z)\end{bmatrix}$ from the coordinate system (x,y,z) to the coordinate system (ξ,ζ,η). We then define the shape function at node i in an arbitrary quadrilateral element, ϕ_i^e, as

$$\phi_i^e(x,y,z) = N_i(\xi(x,y,z),\zeta(x,y,z),\eta(x,y,z)) \qquad \text{for } i = 1,2,3,4,5,6. \quad \text{(A.94)}$$

In the other way, we have

$$N_i(\xi,\zeta\eta) = \phi_i^e(x(\xi,\zeta,\eta),y(\xi,\zeta,\eta),z(\xi,\zeta,\eta)) \qquad \text{for } i = 1,2,3,4,5,6. \quad \text{(A.95)}$$

To approximate the unknown variables in this element type, we choose three nodes of an arbitrary triangular element Ω_e for interpolation. Let $\{f_1, f_2, f_3, f_4\}$ be the value of the unknown function f at node $1, 2, 3$ and 4 of this element, respectively. Hence, the function f in Ω_e can be interpolated by

$$\begin{aligned} f^e(x,y,z) &= \phi_1^e(x,y,z)f_1 + \phi_2^e(x,y,z)f_2 + \phi_3^e(x,y,z)f_3 + \phi_4^e(x,y,z)f_4 \\ &\quad + \phi_5^e(x,y,z)f_5 + \phi_6^e(x,y,z)f_6, \\ &= \sum_{i=1}^{6} \phi_i^e(x,y,z)f_i. \end{aligned} \quad \text{(A.96)}$$

By using the coordinate transformation, Equation (A.44) becomes

$$\begin{aligned} f^e(x,y,z) &= \sum_{i=1}^{6} \phi_i^e(x,y,z)f_i, \\ &= \sum_{i=1}^{6} \phi_i^e(x(\xi,\zeta,\eta),y(\xi,\zeta,\eta),z(\xi,\zeta,\eta))f_i, \\ &= \sum_{i=1}^{6} N_i(\xi,\zeta,\eta)f_i, \\ &= g^e(\xi,\zeta,\eta), \end{aligned} \quad \text{(A.97)}$$

where $g^e(\xi,\zeta,\eta)$ is a coordinate transformed function of the function f.

Using the property of transformation of multiple integral from rectangular to curvilinear coordinate, the integration of the unknown function f can be calcu-

lated as

$$\iiint_{\Omega} f(x,y,z)d\Omega = \iiint_{\bar{\Omega}_e} g(\xi,\zeta,\eta)det(J_{pr})d\eta d\zeta d\xi,$$
$$= \int_0^1 \int_0^{1-\xi} \int_0^{1-\xi-\zeta} g(\xi,\zeta,0)det(J_{pr})d\eta d\zeta d\xi. \quad \text{(A.98)}$$

where

$$det(J_{pr}) = det\left(\begin{bmatrix} \frac{x(\xi,\zeta,\eta)}{\partial\xi} & \frac{y(\xi,\zeta,\eta)}{\partial\xi} & \frac{z(\xi,\zeta,\eta)}{\partial\xi} \\ \frac{x(\xi,\zeta,\eta)}{\partial\zeta} & \frac{y(\xi,\zeta,\eta)}{\partial\zeta} & \frac{z(\xi,\zeta,\eta)}{\partial\zeta} \\ \frac{x(\xi,\zeta,\eta)}{\partial\eta} & \frac{y(\xi,\zeta,\eta)}{\partial\eta} & \frac{z(\xi,\zeta,\eta)}{\partial\eta} \end{bmatrix}\right). \quad \text{(A.99)}$$

Bibliography

[1] M.T.Draney C.A.Taylor. experimental and computational methods in cardiovascular fluid mechanics. *Annu.Rev.Fluid Mech.*, 36.

[2] J.E.Burgess R.S.Pergolizzi M.J.Sheridan C.M.Putman J.R.Cebral, M.A.Castro. Characterization of cerebral aneurysms for assessing risk of rupture by using patient-specific computational hemodynamics models. *AJNR Am.J.Neuroradiol*, 26:2550–2559, 2005.

[3] M.Resch K.Perktole, R.Peter. Pulsatile non-newtonian blood flow simulation through a bifurcation with an aneurysm. *Biorheology*, 26:1011–1030, 1989.

[4] M.T.Draney N.M.Wilson P.S.Tsao R.J.Herfkens C.A.Taylor B.T.Tang, C.P.Cheng. Abdominal aoric hemodynamics in young health adults at rest and during lower limb exercise: quantification using image-based computer modeling. *Am.J.Physiol.Heart Cir.Physiol.*, 291:H668–H676, 2006.

[5] D.A.Steinman G.R.Stuhne. Finite-element modeling of the hemodynamics of stented aneurysms. *J.Biomech.Eng*, 126:382–387, 2004.

[6] C.Kleinstreuer Z.Li. Blood flow and structure interactions in a stented abdominal aortic aneurysm model. *Med.Eng.Phys.*, 27:369–382, 2005.

[7] G.Pennati G.Dubini T.Y.Hsia M.R. de Leval E.L.Bove F.Migliavacca, R.Balossino. Multiscale modelling in biofluidynamics: application to reconstructive paediatric cardiac surgery. *J.Biomech*, 39:1010–1020, 2006.

[8] D. de Zelicourt S.Sharma K.Kanter M.Fogel A.P.Yoganathan D.D.Soerensen, K.Pekkan. Introduction of a new optimized total cavopulmonary connection. *Ann.Thorac.Surg.*, 83:2182–2190, 2007.

[9] J.P.Ku D.Parker B.N.Steele K.Wang C.K.Zarins C.A.Taylor, M.T.Draney. Predictive medicine:computational techniques in therapeutic decision-making. *Comput.Aided Surg*, 4:231–247, 1999.

[10] J.Dankelman J.A.E.Spaan P.Bruinsma, T.Arts. Model of the coronary circulation based on pressure dependence of coronary resistance and compliance. *Basic Res.Cardiol*, 83.

[11] J.D.Van Janssen R.S.Reneman A.Segal C.C.M.Rindt, A.A.Steenhoven. A numerical analysis of steady flow in a three-dimensional model of the carotid artery bifurcation. *J.Biomech*, 23.

[12] M.B.Scheidegger D.Liepsch K.Perktold P.Boesiger R.H.Botnar, G.Rappitsch. Hemodynamics in the carotid artery bifurcation: a comparison between numerical simulations and in vitro mri measurements. *J.Biomech*, 33.

[13] Fung YC. Biomechanics: Circulation. *Springer-Verlag New York Inc.*

[14] Sakamoto M Matsuzawa T Gao F, Guo Z. Fluid-structure interaction within a layered aortic arch model. *J.Biol Phys*, 32.

[15] C.Vergara F.Nobile. An effective fluid-structure interaction formulation for vascular dynamics by generalized robin conditions. *SIAM Journal on Scientific Computing*, 30(2):731–763, 2008.

[16] G.Guidoboni A.Mikelic C.Hartley D.Rosenstrauch S.Canic, J.Tambaca. Modeling viscoelastic behaviour of arterial walls and their interaction with pulsatile blood flow. *SIAM Journal on Applied Mathematics*, 67(01):164–194, 2006.

[17] N.Cavallini S.Canic G.Guidoboni, R.Glowinski. Stable loosely-coupled-type algorithm for fluid-structure interaction in blood flow. *Journal of Computational Physics*, 228(18):6916–6937, 2009.

[18] N.Cavallini S.Canic S.Lapin G.Guidoboni, R.Glowinski. A kinematically coupled time-splitting scheme for fluid-structure interaction in blood flow. *Journal of Computational Physics*, 22(5):684–688, 2009.

[19] R.Glowinski J.Tambaca A.Quaini M.Bukac, S.Canic. Fluid-structure interaction blood flow capturing non-zero longitudinal structure displacement. *Journal of Computational Physics*, 235.

[20] M.A.Fernandes. Incremental displacement-correction schemes for incompressible fluid-structure interaction. *Numerische Mathematik*.

[21] K.E.Jansen T.J.Hughes C.A.Taylor C.A.Figueroa, I.E.Vignon-Clementel. A coupled momentum method for modeling blood flow in three-dimensional deformable arteries. *Computer Methods in Applied Mechanics and Engineering*, 195(41-43):5685–5706, 2006.

[22] C.A.Taylor J.D.Humphrey C.A.Figueroa, S.Baek. A computational framework for fluid-solid-growth modeling in cardiovascular simulations. *Computer Methods in Applied Mechnics and Engineering*, 198(45-46):3583–3601, 2009.

[23] Buraskorn Nuntadilok. *Mathematical model and numerical technique of blood flow in the system of human coronary arteries with no graft and with a bypass graft.* Phd thesis, Mahidol University, 2012.

[24] B. Wiwatanapataphee Y.H. Wu. *Finite element method and applications.* Misterkopy publishing Company, September 2006.

[25] Wikibooks. Human physiology/the cardiovascular system. website. Accessed July 2014.

[26] LIFEBEAT: A patient education resource from Boston Scientific. How your heart works. website. Accessed July 2014.

[27] American Society of Hematology. For patients/blood basics. website. Accessed July 2014.

[28] Jr. J.D. Anderson. *Computational Fluid Dynamics : An Introduction.* Springer-Verlag Berlin Heidelberg, 3rd edition, 2009.

[29] Suharsono S. *Analytical Study of Fluid Flows with Slip Boundary.* Ph.d.thesis, Department of Mathematics and Statistics, Curtin University, May 2012.

[30] Qian Sun. *Mathematical Analysis of Microflows Under Electroosmotic Forces.* Ph.d.thesis, Department of Mathematics and Statistics, Curtin University, 2013.

[31] Patrick Penel Jiří Neustupa. The navier-stokes equation with slip boundary conditions. *RIMS Kôkyôroku*, (1536):46–57, 2007.

[32] C.L.M.H.Navier. Memoire sur les lois du mouvement des fluids. *Mem. Acad. Sci. Inst Fr 6*, (6):389–416, 1829.

[33] Christopher David Frederick Honig. *Validation of the No-Slip Boundary Condition at Solid-Liquid Interfaces*. Ph.d thesis, University of Melbourne, Octorber 2008.

[34] G. Chauveteau. Rodlike polymer solution flow through fine pores: influence of pore size on rheological behaviour. *Journal of Rhelogy*, page 2(26):111, 1982.

[35] H.hervet R.Pit and L.Leger. A sequential quadratic programming algorithm for nonconvex, nonsmooth constrained optimization. *Physics Review Letter*, page 2(85):980, 2000.

[36] Mauricio Giraldo Cesar Nieto, Henry Power. Boundary elements solution of stokes flow between curved surfaces with nonlinear slip boundary condition. *Wiley Online Library*, 2012.

[37] P.A.Thompson and S.M.Troian. A general boundary condition for liquid flow at solid surface. *Nature 389*, pages 360–362, 1997.

[38] Y.Zhu and S.Granick. Rate-dependent slip of newtonian liquid at smooth surfaces. *Phys Rev Lett 87*, (096105-1-096105-4), 2001.

[39] E.Lauga and H.A.Stone. Effective slip in pressure-driven stokes flow. *J Fluid Mech 489*, pages 55–77, 2003.

[40] Y.Liu and D.K. Tan. Steaming potenial and wall-slip effects on pressure-driven microchannel flow. *CIESC*, pages 64(5):1173–1179, 2013.

[41] C.C.Zuo P.Zhang and D.Y.Zhou. Study on characteriecs of liquid flow through a rectangular microchannel with electrokinetic effects. *Optics and Precision Engineer*, pages 15(4):523–529, 2007.

[42] F.C. Hoppensteadt and C.S. Peskin. Modeling and simulation in medicine and the life sciences. *New York: Springer Verlag*, page 376 pp, 2001.

[43] A. Quarteroni and L. Formaggia. Mathematical medelling and numerical simulation of the cardiovascular system. in: N. ayache(ed.), modelling of living systems. *Elsevier (Amsterdam)*, 2003.

[44] T.J. Pedley. The fluid mechanics of large blood vessels. *Cambridge, G.B.: Cambridge University Press*, page 461 pp, 1980.

[45] A. Quarteroni L. Formaggia, F. Nobile and A. Veneziani. Multiscale modelling of the circulatory system: a preliminary analysis. *Comput. Visual. Sci.2*, pages 75–83, 1999.

[46] W.F. Keitzer V.L. Streeter and D.F. Bohr. Pulsatile pressure and flow through distensible vessels. *Circulation Res. 13*, pages 3–20, 1963.

[47] N. Stergiopulos F. Phythoud and J.-J. Meister. Forward and backward waves in the arterial system: nonlinear separation using riemann invariants. *Technol.Health Care 3*, pages 201 – 207, 1995.

[48] J.J.Wang. *Wave Propagation in a Model of the Human Arterial System.* Ph.d thesis, Imperial College, University of London, 1997.

[49] J.J.Wang and K.H.Parker. Wave propagation in a model of the arterial circulation. *journal of Biomechnics*, (37):457–470, 2004.

[50] N.Westerhof and A.Noordergraaf. Arterial viscoelasticity: a generalized model effect on input impedence and wave travel in the systemic tree. *J. Biomech*, (3):357–379, 1970.

[51] R.Skalak. *The synthesis of a complete circulation*, volume 2. London: Academic Press, 1972.

[52] P.Niederer J.C.Stettler and M.Anliker. Theoretical analysis of arterial hemodynamics including the influence of bifurcations, part i:mathematical model and predictionof normal pulse patter. *Ann. Biomed. Eng.*, (9):145–164, 1981.

[53] P.Niederer J.C.Stettler and M.Anliker. Theoretical analysis of arterial hemodynamics including the influence of bifurcations, part ii:critical evaluation of theoretical model and comparison with noninvasive measurements of flow patterns in normal and pathological cases. *Ann. Biomed. Eng.*, (9):165–175, 1981.

[54] D.F.Young N.Stergiopulos and T.R.Rogge. Computer simulation of arterial flow with applications to arterial and aortic stenoses. *J.Biomech*, (25):1477–1488, 1992.

[55] W.F.Keitzer V.L.Streeter and D.F.Bohr. Pulsatile pressure and flow through distensible vessels. *Circulation Res*, (13):3–20, 1963.

[56] N.Stergiopulos F.Phythoud and J.J.Meister. Forward and backward waves in the arterial system:nonlinear separation using riemann invariants. *Technol.Health Care*, (3):201–207, 1995.

[57] F.Nobile L.Formaggia and A.Quarteroni. *A one-dimensional model for blood flow: application to vascular prosthesis.* Mathematical Modeling and Numerical Simulation in Continuum Mechanics. Springer-Verlag Berlin Heidelberg, 2002. Volume 19 of Lecture Notes in Computational Science and Engineering.

[58] S.Čanič. Blood flow through compliant vessels after endovascular repair:wall deformations induced by the discontinuous wall properties. *Comput. Visual. Sci.*, (4):147–155, 2002.

[59] G.Pontrelli. A mathematical model of flow through a viscoelastic tube. *Med. Biol. Eng. Comput.*, (40):550–556, 2002.

[60] G.Pontreli. *Nonlinear pulse propagation in blood flow problems.* Pregress in Industrial Mathematics at ECMI2000. Springer-Verlag Berlin Heidelberg, 2002. pp.201-207.

[61] M.Olufsen. *Modeling the Arterial System with Reference to an Anestesia Simulatior.* PhD thesis, Roskilde University, 1998. Ph.D thesis, Tekst 345.

[62] D. Lamponi L.Formaggia and A. Quarteroni. One-dimensional models for blood flow in arteries. *Journal of Engineering Mathmatics*, 47:251–276, 2003.

[63] J.Peiró S.J.Sherwin, L.Formaggia and V.Franke. Computational modelling of 1d blood flow with variable mechanical properties and its application to the simulation of wave propagation in the human arterial system. *Int. J. Number. Meth. Fluids*, (43):673–700, 2003.

[64] W.Y.Kim E.M.Pedersen A.Nadim M.S.Olufsen, C.S.Peskin and J.Larsen. Numerical simulation and experimental validation of blood flow in arteries with structured-tree outflow conditions. *Annals Biomed. Engng.*, (28):1281–1299, 2000.

[65] J.Peiró S.J.Sherwin, V.Franke and K.Parker. One-dimensional modelling of a vascular network in space-time variables. *Journal of Engineering Mathematics*, (47(3-4)):217–250, 2003.

[66] B.Chahboune and J.M. Crolet. Numerical simulation of the blood-wall interaction in the human left ventricle. *The European Physical Journal Applied Physics*, 2(13):291–297, 1998.

[67] Josip Tambača Sunčica Čanić, Andro Mikelić. A two-dimensional effective model describing fluid-structure interaction in blood flow:analysis, simulation and experimental validation. *Comptes Rendus Mécanique*, 333:867–883, 2005.

[68] P.F. J-F Gerbeau, M.Vidrascu. Fluid-structure interaction in blood flow on geometries based on medical imaging. *Computers and structures*, (83), 2005.

[69] Kenneth E.Jansen Thomas J.R.Hughes Charles A. Taylor C.Alberto Figueroa, Irene E.Vignon-Clementel. A coupled momentum method for modeling blood flow in three-dimensional deformable arteries. *Comput.Methods Appl. Mech. Engrg.*, (195):5685–5706, 2006.

[70] C.H.G.A. van Oijen D.Bessems T.W.M. Gunther A.Segal B.J.B.M.Wolters J.M.A.Stijnen f.P.T.Baaijens F.N. van de Vosse, J. de Hart. Finite-element-based computational methods for cardiovascular fluid structure interaction. *J. Engrg. Math.*, (47):335–368, 2003.

[71] G.Rappitsch K.Perktole. Computer simulation of local blood flow and vessel mechanics in a compliant carotid artery bifurcation model. *J.Biomech*, (28):845–856, 1995.

[72] J.F.Gerbeau S.Salmon, M.Thiriet. Medical image-based computational model of pulsatile flow in saccular aneurisms. *Math.Modell.Numer.Anal.*, (37):663 – 679, 2003.

[73] K.Takagi R.Torii M.Hayakawa K.Katada A.Morita T.Kirino M.Shojima, M.Oshima. Magnitude and role of wall shear stress on cerebral aneurysm. *computational fluid dynamic study of 20 middle cerebral artery aneurysms*, 35:2500–2505, 2004.

[74] O.Soto R.Lohner N.Alperin J.R.Cebral, M.A.Castro. Blood-flow models of the circle of willis from magnetic resonance data. *J. Engrg. Math.*

[75] T.Kobayashi K.Takagi M.Oshima, R.Torii. Finite element simulation of blood flow in the cerebral artery.

[76] C.K.Zarins C.A.Taylor, T.J.R.Hughes. Finite element modeling of blood flow in arteries. *Comput. Methods Appl. Mech. Engrg*, (158):155–196, 1998.

[77] T.K. Zimmermann T.J.R.Hughes, W.K.Liu. Lagrangian eulerian finite element formulation for incompressible viscous flows. *Comput. Methods Appl. Mech. Engrg.*, (29):329–349, 1981.

[78] J.P.Halleux J.Donea, S.Giuliani. An arbitrary lagrangian eulerian finite element method for transient dynamic fluid structure interactions. *Comput. Methods Appl. Mech. Engrg.*, (33):689–723, 1982.

[79] J. mouro P.Le Tallec. Fluid structure interaction with large structural displacements. *Comput. Methods Appl. Mech. Engrg.*, (190):3039–3067, 2001.

[80] P.Boesiger K.Perktold A.Leuprecht, S.Kozerke. Blood flow in the human ascending aorta: a combined mri and cfd study. *J.Engrg.Math.*, (47):387–404, 2003.

[81] M.Heil. An efficient solver for the fully coupled solution of large-displacement fluid-structure interaction problem. *Comput.Methods Appl. Mech. Engrg.*, (193):1–23, 2004.

[82] G.W.M.Peters P.J.G.Schreurs J.De Hart, F.P.T. Baaijens. A computational fluid structure interaction analysis of a fiber-reinforced stentless aortic valve. *J.Biomech.*, (36):699–712, 2003.

[83] D.M.McQueen C.S.Peskin. A general method fore the computer simulation of biological systems interacting with fluids. *Symposia Soc. Exp. Biol.*, (49):265–267, 1995.

[84] P.Le Tallec M.A.Fernandez. Linear stability analysis in fluid structure interaction with transpiration. part ii:numerical analysis and applications. *Comput.Methods Appl.Mech.Engrg.*, (192):4837–4873, 2003.

[85] L.Formaggia S.Deparis, M.A.Fernandez. Acceleration of a fixed point algorithm for fluid structure interaction using transpiration conditions. *Math.Modell.Numer.Anal.*, (37):601–616, 2003.

[86] A.C. Eringen. Continuum theory of dense rigid suspension. *Rheol.Acta 30*, pages 23 – 32, 1991.

[87] A.C. Eringen. A continuum theory of dense ridid suspensions. *Z. Angew Math Phys. (ZAMP) 56*, pages 529–547, 2005.

[88] N.D Sylvester T. Ariman, M.A. Turk. Microcontinuum fluid mechanics - a review. *Int. J. Engng. Sci.11*, pages 905–930, 1973.

[89] T. Ariman M.A. Turk, N.D. Sylvester. On pulsatile blood flow. *Trans. Soc. Rheol.17*, pages 1–21, 1973.

[90] L. Debnath. On a microcontinuum model of pulsatile blood flow. *Acta Mech. 24*, pages 165–177, 1976.

[91] G. Ahmadi. A continuum theory of blood-flow. *Scientia Sinica 24*, pages 1465–1474, 1981.

[92] L. Usha S.N. Majhi. Modeling the fahraeus-lindqvist effect through fluids of differential type. *Int. J. Engng. Sci. 26*, pages 503–508, 1988.

[93] H.I. Andresson K. Haldar. Two-layered model of blood flow through stenosed arteries. *Act Mech. 117*, pages 221–228, 1996.

[94] Yazariah Yatim S. Sankar. Comparative analysis of mathematical models for blood flow in tapered constricted arteries. *Abstract and Applied Analysis, Article ID 235960*, 2012, 2012.

[95] V.R. Nair S.N. Majhi. Pulsatile flow of third grade fluids under body acceration - modeling blood flow. *Int. J. Engng. Sci. 32*, pages 839–846, 1994.

[96] T.X. Phuoc M. Massoudi. Pulsatile flow of blood using a modified second-grade fluid model. *Int. J. computers and mathematics with application 56*, pages 199–211, 2008.

[97] J.C. Slattery. Advance transport phenomena. *Cambridge University Press*, 1999.

[98] L. Leger R. Pit, H. Hervet. Direct experimental evidence of slip in hezadecane: Solid interfaces. *Physics Review Letters 85*, page 980, 2000.

[99] T. Taniguchi R. Tuinier. Polymer depletion-induced slip near an interface. *Journal of Physics Condensed Mstter 17*, page L9, 2005.

[100] Z.Y. Goo B.Y. Cao, M. Chen. Velocity slip of liquid flow in nanochannels. *Acta Physica Sinica 55(10)*, page 5305, 2006.

[101] L. Szalmas. Slip-flow boundary condition for straight walls in the lattice boltzmann model. *art.no. 066710, physical Review E 7306(6)*, page 6710, 2006.

[102] J.P. Pascal. Instability of power-law fluid flow down a porous incline. *Journal of Non-Newtonian Fluid Mechanics 133(2-3)*, page 109, 2006.

[103] P.D.M. Spelt O.K. Matar K.C. Sahu, P. Valluri. Linear instability of pressure-driven channel flow of a newtonian and a herschel-bulkley fluid. *Physics of Fluids 19*, page 122101, 2007.

[104] Y.X. Li J.L. Xu. Boundary conditions at the solid-liquid surface over the multiscale channel size from nanometer to micron. *International Journal of Heat and Mass Transfer 50(13-14)*, pages 2571–2581, 2007.

[105] S. Granick Y.X. Zhu. Rate-dependent slip of newtonian liquid at smooth surfaces. *art.no. 096105, Physical Review Letters 8709(9)*, page 6105, 2001.

[106] M. Hu Y.H. Wu, B. Wiwatanapataphee. Pressure-driven transient flows of newtonian fluids through microtubes with slip boundary. *Physica A - Statistical Mechanics and its applications*, 387:5979–5990, 2008.

[107] M. Hu et al Y.H. Wu, B. Wiwatanapataphee. A study of transient flows of newtonian fluids through micro-annuals with a slip boundary. *Journal of Physica A - Mathematical and Theoretical Journal*, 42, 2009.

[108] George Kaoullas Georgios C. Georgiou. Newtonian flow in a trianular duct with slip at the wall. *Mecanica*, 2013.

[109] Georgios C. Georgiou George Kaoullas George Kaoullas. Newtonian poiseuille flows with slip and non-zero slip yield stress. *Mecanica*, 2013.

[110] X. Yu Y.H. Wu, B. Wiwatanapataphee. An enthalpy control volume method for transient mass and heat transport with solidification. *International Journal of Computation Fluid Dynamics 18(7)*, pages 577–584, 2004.

[111] B. Wiwatanapataphee. Modelling of non-newtonian blood flow through stenosed coronary arteries. *Dynamics of Continuous, Discrete and Impulsive Systems Series B: Applications*, 2008.

[112] B. Wiwatanapataphee S. Amornsamankul, K. Kaorapapong. Three-dimensional simulation of femur bone and implant in femoral canal using

finite element method. *International Journal of Mathematics and Computers in Simulation 4(4)*, pages 171–178, 2010.

[113] B. Wiwatanapataphee Y.H. Wu. Modelling of turbulent flow and multiphase heat transfer under electromagnetic force. *Discrete and Continuous Dynamical Systems - Series B 8(3)*, pages 695–706, 2007.

[114] K.K. Lee H.B. Lee, I.W. Yeo. Water flow and slip on napl-wetted surfaces of a paralled-walled fracture. *Geophysical Research Letters 34(19)*, (19401), 2007.

[115] Y.H. Wu Y. Lenbury B. Wiwatanapataphee, D. Poltem. Simulation of pulsatile flow of blood in stenosed coronary artery bypass with graft. *Mathematical Biosciences and Engineering*, 3(2):695–706, 2006.

[116] C.S. Man and Q.K. Sun. On the significance of normal stress effects in the flow of glaciers. *J. Glaciology*, pages 268–273, 1987.

[117] C.S. Man. Nonsteady channel flow of ice as a modified second-order fluid with power-law viscosity. *Arch. Ration. Mech. Anal. 119*, pages 35–57, 1992.

[118] P.Chaturani and V.Palanisamy. Pulsatile flow of blood with periodic body acceleration. *International Journal of Engineering Science*, 29(1):113–121, 1991.

[119] S.F.Kaldas S.A.N.Elsoud and S.K.Mekheimer. Interaction of peristaltic flow with pulsatile couple stress fluid. *Journal of Biomathematics*, 13(4):417425, 1998.

[120] N.A.S.Afifi E.F.Elshehawey, E.M.E.Elbarbary and M.El-Shahed. Pulsatile flow of blood through aporous medium under periodic body acceleration. *International Journal of Theoretical Physics*, 39(1):183–188, 2000.

[121] K.Das and G.C.Saha. Arterial mhd pulsatile flow of blood under periodic body acceleration. *Bulletin of Society of Mathematicians. Banja Luka*, 16.

[122] C.Vasudev G.P.Rao, S.Ravikumar and R.S.Prasad. Unsteady two-phase viscous ideal fluid flow through a parallel plate channel under a pulsatile pressure gradient subjected to a body acceleration. *Journal of Engineering and Applied Sciences*, 6(1):1–7, 2011.

[123] Q.Hussain T.Hayat and N.Ali. Influence of partial slip on the peristaltic flow in a porous medium. *Physica A*, 387.

[124] N.T.El-Dabe E.F.El-Shehawy and I.M.El-Desoky. Slip effects on the peristaltic flow of a non-newtonian maxwellian fluid. *Acta Mechanica*, 186(1-4):141–159, 2006.

[125] I.M.Eldesoky. influence of slip condition on peristaltic transport of a compressible maxwell fluid through porous medium in a tube. *International Journal of Applied Mathematics and Mechanics*, 8(2):99–117, 2012.

[126] W.Kwang-Hua Chu and J.Fang. Peristaltic transport in a slip flow. *European Physical Journal B*, 16(3):543–547, 2000.

[127] T.Hayat N.Ali, Q.Hussain and S.Asghar. Slip effects on the peristaltic transport of mhd fluid with variable viscosity. *Physics Letters A*, 327(9):1477–1489, 2008.

[128] M.Umar T.Hayat and N.Ali. The influence of slip on the peristaltic motion of a third order fluid in an asymmetric channel. *Physics Letter A*, 372(15):2653–2664, 2008.

[129] A.M.Sobh. Interaction of couple stresses and slip flow on peristaltic transport in uniform and nonuniform channels. *Turkish Journal of Engineering and Environmental Science*, 32(2):117–123, 2008.

[130] A.M.Sobh. Slip flow in peristaltic transport of a carreau fluid in an asymetric channel. *Canadian Journal of Physics*, 87(8):957–965, 2009.

[131] S.Nadeem and S.Akram. Slip effects on the peristaltic flow of a jeffrey fluid in an asymmetric channel under the effect of induced magnetic field. *International Journal for Numerical Methods in Fluids*, 63(3):374–394, 2010.

[132] I.M.Eldesoky. Slip effects on the unsteady mhd pulsatile blood flow through porous medium in an artery under the effect of body acceleration. *Physics Letter A*, 2012.